Abdominal organ segmentation based on a statistical shape model

Atsushi Saito

Department of Electronic and Information Engineering,
the Graduate School of Engineering of
Tokyo University of Agriculture and Technology

This dissertation is submitted for the degree of
Doctor of Philosophy

Tokyo University of
Agriculture and Technology

March 2016

Acknowledgements

During my five years working in the Shimizu laboratory in Tokyo University of Agriculture and Technology, I was supported by many people. I would like to take this opportunity to express my gratitude to them.

First, I would like to express my most heartfelt thanks to my supervisor Prof. Akinobu Shimizu, who encouraged me to study for a Ph.D. I could not have completed this study without his help. I would also like to thank Dr. Elco Oost very much for helping me with the work on MICCAI 2013. In addition, the success of most of my research during my Ph.D. studies is due to the contribution of Dr. Hidefumi Watanabe, Mr. Keita Nakagomi, and Ms. Misaki Nakada.

I thank Dr. Seiji Yamamoto and all the staff at the Ai information center, Chiba University. The study related to postmortem liver SSM and segmentation in Chapters 2 and 3 was performed in collaboration with members of the Ai information center. I wish to acknowledge the assistance provided by Dr. Okada of the University of Tsukuba, and Prof. Sato of the Nara Institute of Science and Technology, for providing their segmentation algorithm with the training software and for helpful discussions in Chapter 4. Part of this research was conducted under a Grant-in-aid for scientific research from the Japanese Ministry of Education, Culture, Sports, Science, and Technology.

I would like to give many sincere thanks to my parents and grandparents. I am very grateful for your financial and moral support.

Finally, during my Ph.D. studies, I was glad to share a lot of time with my labmates Dr. Hanaoka, Mr. Umetsu, Mr. Inagaki, Mr. Oshima, Mr. Takata, Mr. Yamashita., Mr. Okata., Mr. Hagihara, Mr. Kishimoto, Mr. Sunada, Mr. Ito, and Ms. Tachibana. Thank you.

Abstract

This study focuses on abdominal organ segmentation using a statistical shape model (SSM). One of the main contributions of the study is that it introduces an algorithm for postmortem computed tomography (CT) volume segmentation, which is a first application of computer-aided diagnosis using autopsy imaging (Ai). The method is innovative not only in its application but also in the methodology for the statistical shape analysis of a limited number of label volumes with a large variation in shape. A second important contribution is that it provides a globally optimal solution for the objective functional of the segmentation, considering all possible shapes generated by the SSM. The thesis consists of five chapters. The first chapter provides the background of medical image segmentation and Ai, and the purpose of the study presented in thesis. In the second chapter, the development of an SSM of a liver for postmortem CT images is described. The performance of the SSM of a postmortem liver is found to be improved by using artificial shape labels synthesized from *in vivo* liver shape labels. In Chapter 3, the integration of these SSMs in the postmortem liver segmentation algorithm is explained. The conventional SSM-based liver segmentation algorithm is extended to postmortem CT volumes by using a dynamic probabilistic atlas. The best SSM described in Section 2 also show the highest performance in segmentation. Chapter 4 provides a solution to optimize the segmentation energy across all shapes in the SSM, as well as the segmentation labels in a graph cut segmentation. The solution is guaranteed to be globally optimal, as compared to that of the conventional algorithm used in existing methods that employs a branch-and-bound search over a search tree of predefined shapes. The proposed algorithm improves the segmentation accuracy as well as the computational efficacy. The performance is also comparable to that of the state-of-the-art segmentation algorithms. Finally, the summary and conclusions are presented in Chapter 5, and future works are discussed.

Table of contents

List of figures

List of tables

Nomenclature

Roman Symbols

$\mathbb{R}$	the set of all real numbers
$\mathbb{Z}$	the set of all integer numbers
d	number of dimensions of the eigenshape space
$\boldsymbol{I}$	a three-dimensional volume image
$\mathcal{L}$	a binary label set $(= \{0, 1\})$
$\mathcal{V}$	the set of voxels
$\mathcal{E}$	the set of neighboring voxel pairs

Greek Symbols

$\boldsymbol{\alpha}$	coefficient vector of eigenshape space
$\boldsymbol{\phi}$	a level set function
$\boldsymbol{\varphi}$	a weighted level set function

Other Symbols

$\|\cdot\|$	L2 norm of a vector
$\cdot^\top$	transpose of a matrix
$\cdot^+$	Moore–Penrose pseudoinverse
$\oint_\Gamma$	integration around a curve Γ

Chapter 1

Introduction

1.1 Background of statistical shape models for medical image segmentation

Since the 1970s, great advances have been made in imaging technology for 3-dimensional (3D) X-ray computed tomography (CT), which is now an indispensable tool for diagnosis in many clinical practices in Japan. In addition, computer aided diagnosis (CAD) has become an important research subject. Automated segmentation of an abdominal organ from a CT image is a crucial task in many CAD systems. However, the segmentation of an abdominal organ from a CT image has constituted a difficult problem because of the relatively low S/N ratio of the image, as well as the relatively high variation in the shape of an organ belonging to different patients, as shown in Fig. 1.1.

Over the last two decades, a number of image segmentation algorithms have been proposed. One of the early successful methods was based on active contour models, also referred to as *Snakes*, introduced in Kass et al. [2], where the evolution of the contour is constrained by two types of energy: external energy, which evaluates the fitness between the model and the image data, and internal energy, which assesses the smoothness of the contour. The original version of Snakes, which was designed for 2D images, was extended to 3D image segmentation [3]. However, since the smoothness constraint was based not on the statistical information but on a general spline function, the segmentation results may be inappropriate.

A segmentation algorithm based on a statistical shape model (SSM) is one of the most popular recent approaches for organ segmentation. This has an advantage over non-SSM-based approaches, such as Snakes, in that it can describe global shape

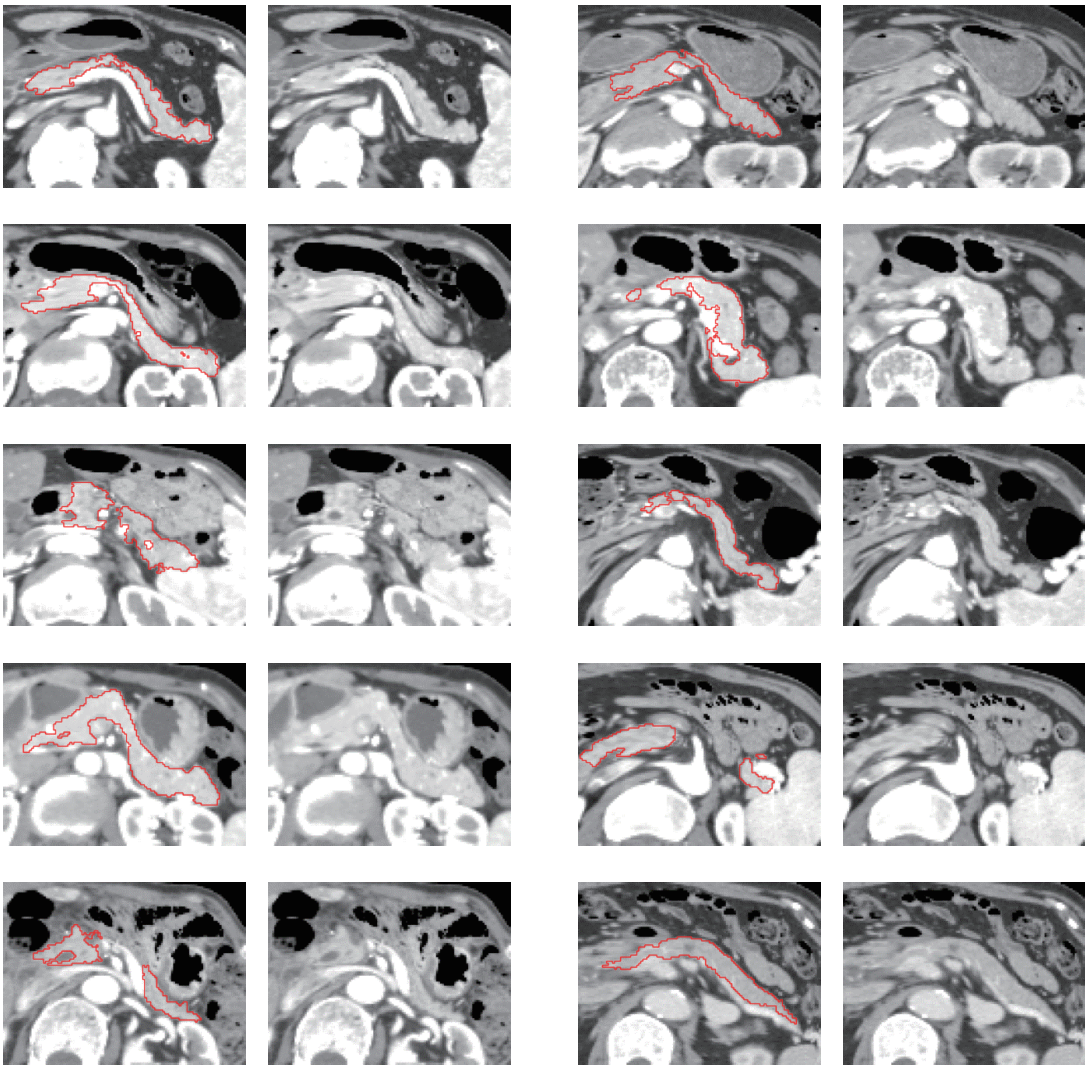

Fig. 1.1 Examples of ten abdominal CT images with and without contours of pancreas (*right two columns*) shown in red

constraints learned statistically from the training shapes. Thus far, a variety of SSM construction algorithms have been proposed, which are categorized into two groups by the shape representation methods: explicit and implicit.

The most widely used SSM that employs explicit shape representation is the point distribution model (PDM) [4]. In PDM, the distribution of the anatomical landmarks on training shapes is statistically analyzed by principal component analysis (PCA). Pizer et al. [5] proposed a shape representation called *m-rep*, in which shapes are represented by the medial points of the center line and the radii. The main drawback of this method is that it requires that point correspondences be established between different subjects among the training shapes. Styner et al. [6] proposed a method using spherical harmonics for shape representation called SPHARM-PDM, which represents the shape on a frequency domain. A possible limitation of SPHARMs is that the shapes are required to have a spherical topology. Moreover, it remains to be seen which is the best method for mapping the shape onto the frequency domain.

For implicit shape representations, the *statistical deformation model* was proposed, which statistically models the deformation of the mean shape, i.e., the template. Rueckert et al. [7] introduced a statistical model for the deformation field described as a free form deformation (FFD) model that deforms an object by manipulating an underlying mesh of control points. Durrleman [8] proposed employing the LDDMM (Large Deformation Diffeomorphic Metric Mapping) for the statistical deformation model. LDDMM guarantees that the mapping of the deformation will be diffeomorphic (i.e., continuous and one-to-one), which is a desired property for describing the variation in anatomical structures in many cases. However, this method requires some parameters for the deformation model, as well as huge computational resources for calculating the deformation. The level set distribution model (LSDM) [9] is another widely used implicit shape representation. LSDM describes the contour of a shape as a level set function defined by a discrete signed distance function in a high-dimensional space. The set of shapes represented as level set functions are known not to form a linear space, which may lead to an invalid shape when it is constructed by PCA. Nevertheless, this method requires neither the establishment of the point correspondences between different training subjects nor any parameters for the shape representation, which could be a great advantage over all the SSM construction methods described above.

In other important studies related to SSMs, their extension to multiple organs was investigated. Tsai et al. [10] and Yang et al. [11] developed multi-shape SSM based on multiple level set representations. In more recent studies, logarithms of

odds (LogOdds) based shape representations [12] and label spaces [13] were proposed, and their modification, called isometric log-ratio mapping, was proposed by Changizi and Hamarneh [14]. However none of these methods was designed for abdominal organs. Okada et al. [15] developed multi-shape SSM for seven abdominal organs, where the hierarchy and interrelations among organs were explicitly incorporated, which was successfully applied to multi-organ segmentation. Recently, a hierarchical SSM for fourteen abdominal organs was developed [16], where the synthesized labels were used to overcome the lack of a training dataset; however, its application to multi-organ segmentation remains as future work.

In a number of studies in the literature, these SSMs are integrated in the segmentation process in various manners. Cootes et al. [4] extended their PDM with a model fitting algorithm, which is generally referred to as an active shape model (ASM). ASM is an extension of Snakes that can impose the PDM-based energy on the contour evolution. In [17], some methods are introduced to integrate an SSM in a segmentation algorithm based on the front propagation of the level set, called the level set method. However, the success of this method strongly relies on the initialization of the segmentation. Thus, poor initialization may result in a local optimum, i.e., an undesired segmentation result.

The recent noteworthy progress in segmentation is due to the use of discrete optimization techniques. [18] proposed a graph-based segmentation method, called graph cuts, which was successfully applied to a variety of image segmentations, including segmentation of 3D medical images. The biggest advantage of graph cuts is that the globally optimal solution for the binary segmentation problem can be efficiently computed. Recently, a number of authors integrated SSMs in the graph cut segmentation framework for various applications, *e.g.* , Grosgeorge et al. [19], Malcolm et al. [20], and Nakagomi et al. [21], in which SSM is used to provide prior knowledge of the shape, called a shape prior. However, the segmentation accuracy of these methods still depends on the performance of the shape prior selection method.

Some authors proposed an optimization method not only for segmentation labeling but also for the shape prior. Besbes et al. [22], Chen et al. [23], Xiang et al. [24] presented a joint optimization method of the segmentation and the shape prior from the PDM based on a discrete optimization framework in different manners. However, the global optimality of the solution is not guaranteed in all these methods. Lempitsky et al. [25] proposed a novel framework for jointly computing the optimal graph cut segmentation and the shape prior from a number of shape templates.

Nevertheless, in this method, all the templates should be defined in advance, and the algorithm can consider only a small subset of the shapes generated by the SSM. To the best of my knowledge, a globally and jointly optimal solution for the segmentation labeling and the shape prior remains an unresolved problem.

1.2 Autopsy imaging

1.2.1 Background of autopsy imaging

Autopsy has played an important role in the advances in many fields of medicine *e.g.* , autopsy, pathology, and epidemiology. However, the autopsy rate in Japan is extremely low. As a result, deaths from blunt trauma without surface injuries may be overlooked, and the cause of death may be misinterpreted.

Meanwhile, with the advancement of imaging technology, imaging of cadavers, i.e., postmortem imaging (PMI), is becoming popular as a new approach to corpse analysis. PMI has been conducted under the name of *virtopsy* in Switzerland [26], *virtual autopsy* in France [27] and *Radio-autopsy* in Germany [28], the concepts of which are similar each other. In Japan, a new concept called autopsy imaging (Ai) was proposed by Ezawa et al. [29], M.D. of the National Institute of Radiological Sciences. In this study, I denote PMI by Ai.

Ai has a complementary relationship with conventional autopsy and provides information that supplements that gained from the autopsy [29], resulting in higher diagnostic accuracy. However, a state-of-the-art CT scanner outputs several hundred or several thousand slice images per cadaver, which places a heavy burden on the doctor. Moreover, the specific appearance of targets in Ai, *e.g.* , postmortem changes as well as the pathology or injury that caused death, makes diagnosis difficult even for a trained radiologist. Therefore, a computer-aided diagnosis (CAD) system is required to assist the doctor.

1.2.2 Difficulties in PMCT image segmentation

Difficulties in the segmentation of organs from PMCT images arise because they are very different from *in vivo* CT images. The three most dominant challenges in liver segmentation in Ai are summarized as follows.

Severe organ deformation

Figure 1.2 shows an example of typical changes in the shape of a liver after

death. The right lobe of the liver is elevated because of respiratory arrest, while the left lobe descends because of the dilation of the heart. Moreover, the microbism of organs causes an accumulation of gas in the abdomen, pushing the entire liver upward. These postmortem changes make the variation in the postmortem liver shape much wider than the variation in the *in vivo* liver shape. Consequently, as compared to an *in vivo* liver model, a statistical shape model of the postmortem liver requires a substantial amount of training data.

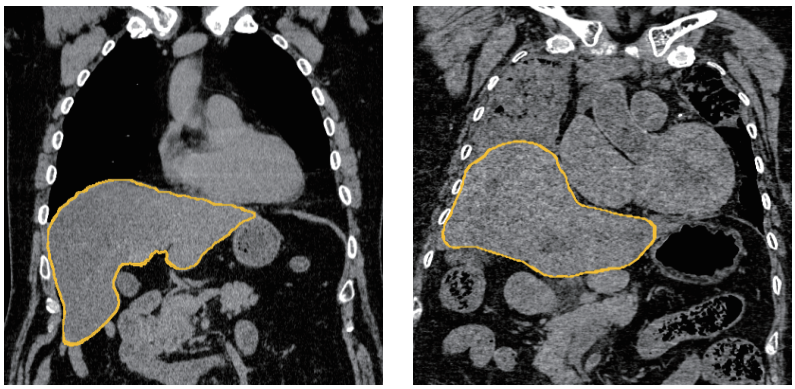

Fig. 1.2 Typical examples from an *in vivo* liver (*left*) and a postmortem liver (*right*). The *yellow lines* indicate the true contours of the livers. In the postmortem liver, the right lobe was elevated owing to respiratory arrest, and cardiac arrest caused enlargement of the right ventricle, resulting in a downward deformation of left lobe

Severe pathology

Postmortem changes in CT values make the liver segmentation from PMCT images much more difficult than do those in *in vivo* CT volumes. For example, Fig. 1.3 shows a severe metastases in the lung, which is one of the specific appearances in PMCT images. Lung disease such as this causes a lower contrast between the lung and the liver, when a contrast agent is used.

Intensity changes and artifacts

Postmortem changes also appear in the CT value, *e.g.* , fluid accumulation in the lungs and postmortem hypostasis. In addition, because of the postmortem rigidity, the doctors are forced to scan corpses with their arms at their side, which may cause strong artifacts in the PMCT volumes. As shown in Fig. 1.4, intensity changes and artifacts lead to a lower S/N ratio between the liver and lung. It should also be noted that PMCT is commonly acquired without using

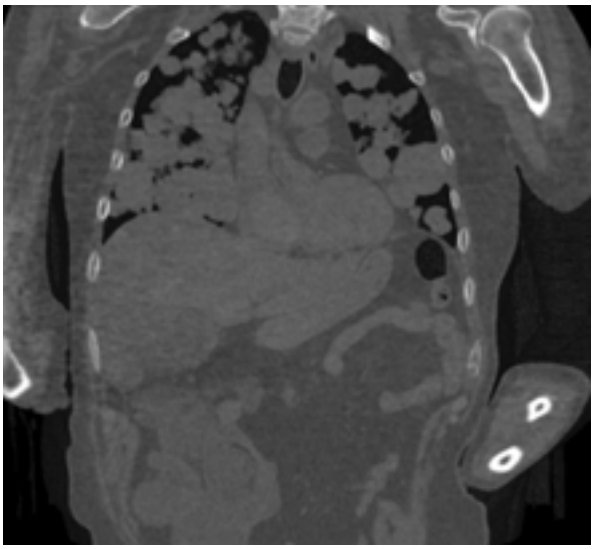

Fig. 1.3 A PMCT case with severe pathology

a contrast agent, which makes it difficult to apply many existing segmentation algorithms designed for multi-phase *in vivo* CT volumes to a single-phase PMCT volume.

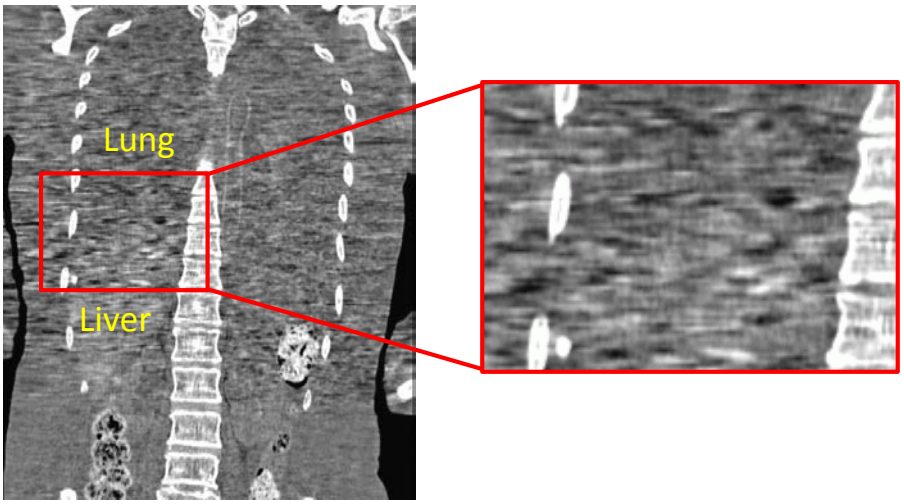

Fig. 1.4 A PMCT case with intensity changes in CT value as well as strong artifacts

For the above reasons, conventional SSM designed for *in vivo* CT images may not applicable to PMCT images. However, no studies have been conducted on a segmentation algorithm for PMCT and the relationship between SSMs in *in vivo* and postmortem organs has not been investigated.

1.3 Purpose

The purpose of this study is to achieve breakthroughs on the issue relate to the SSM-based abdominal organ segmentation on a CT volume, which are summerized as follows:

Developement of an SSM and SSM-based postmortem liver segmentation

Due to the large differences in shape as well as in appearance between *in vivo* and postmortem CT images, segmentation algorithms designed for *in vivo* livers may not applicable to the postmortem livers. Many state-of-the-art liver segmentation algorithms employ SSMs; however all of which are designed for *in vivo* livers.

Integration of an SSM with graph cuts for abdominal organ segmentation

Some conventional studies [22–24] proposed simultaneous optimization of the segmentation and the shape generated from SSM. All of these methods, however, are not guaranteed to achieve globally optimal solution.

1.4 Outline

The rest of this thesis is organized as follows.

In Chapter 2, the SSM construction method for a postmortem liver is introduced. First, the relationship between SSMs obtained from *in vivo* liver CT scans and those from postmortem cases is investigated. Then, a sophisticated SSM construction method for postmortem livers using synthesized-based learning is proposed. The performance of the different SSMs is compared in terms of the performance indices, i.e., *generalization* and *specificity*.

In Chapter 3, the integration of the SSMs mentioned in the previous section into the proposed postmortem liver segmentation algorithm is explained. The performance of the SSMs are compared in terms of segmentation accuracy.

In Chapter 4, pancreas segmentation from *in vivo* CT images is described, where the joint optimization method is employed to obtain an optimal segmentation la-

beling, as well as an optimal shape prior, from all the possible shapes from the SSM.

Chapter 5 summarizes this study. Then, the conclusion and future work are presented.

Chapter 2

Statistical shape model of the postmortem liver

2.1 Introduction

The autopsy rate in Japan is extremely low. As a result, deaths from blunt trauma without surface injuries may be overlooked, and the cause of death may be misinterpreted. A new concept called autopsy imaging (Ai) was proposed by Dr. Ezawa, M.D. of the National Institute of Radiological Sciences in Japan [29]. Ai has a complementary relationship with conventional autopsy and provides supplemental information to the autopsy [30], resulting in higher diagnostic accuracy. A cadaver is scanned using an imaging modality, such as CT, US, or MR. The images are analyzed by a medical doctor and used in the subsequent surgical dissection. However, a state-of-the-art CT scanner outputs several hundred or sev-eral thousand slice images per cadaver, which places a heavy burden on the doctor. Therefore, a computer-aided diagnosis (CAD) system is required to assist the doctor.

In many CAD systems, a statistical shape model (SSM) [31] of an organ plays a key role as a shape prior that achieves high performance during the segmentation of an organ, such as the liver [32, 33] or lung [21]. Recent notable studies include conditional SSMs as described in [34]. Related studies [35, 36] incorporate the uncertainties of the conditions within the conditional SSMs, such as the liver segmentation algorithm with a relaxed conditional SSM developed by Tomoshige et al. [37]. Other important studies relate to SSMs for multiple shapes enable the segmentation process to impose neighbor constraints. Tsai et al. [10] and Yang et al. [11] developed neighbor-constrained segmentation using a multi-shape SSM based

on representations of multiple level sets. Recent studies have proposed different approaches for representing multiple shapes, as well as logarithms of odds-based (LogOdds) shape representations [38] and label spaces [13]. Changizi and Hamarneh [14] introduced isometric log-ratio mapping to overcome several drawbacks of the previous method [13]. More recent studies [15, 39] include applications of multi-shape SSMs to multiple organ segmentation based on abdominal CT volumes. All of these SSMs were originally designed for organs in *in vivo* bodies, but they might also have potential applications in Ai.

However, different types of deformation in a cadaver might not be accounted for by an SSM trained from *in vivo* livers. As shown in Fig. 1.2 of Section 1.2.2, respiratory arrest causes diaphragmatic elevation, and circulatory arrest causes enlargement of the right ventricle, resulting in the right lobe going up and the left lobe going down. This suggests that a conventional SSM constructed from *in vivo* livers [21, 32, 33] might lack the ability to describe postmortem livers. One possible solution to the problem is to use postmortem livers to build an SSM. Because of the shortage of postmortem liver CT data and shape label volumes manually drawn by experts, an SSM trained only from a small number of postmortem livers might not be able to describe the various shapes of postmortem livers.

A machine learning-based methodology has been developed in order to improve accuracy when only a small amount of training data are available, which is called synthesized-based learning [40]. Synthesized-based learning has been successfully applied to many pattern recognition applications such as human shape matching [41] and traffic sign symbol recognition [42]. One of the purpose of this study is to synthesize postmortem liver labels by transforming *in vivo* liver labels and to train an SSM for a postmortem liver using synthesized postmortem liver labels.

To the best of my knowledge, this is the first report that explores an SSM as well as the SSM-based segmentation algorithm for a postmortem liver. The main contributions of this paper are summerized as follows:

(i) Investigation of the relationship between SSMs constructed from *in vivo* livers and those from postmortem livers

(ii) Proposal of algorithms to transform *in vivo* liver labels such that they resemble postmortem liver labels

(iii) Comparison of SSMs constructed using synthesized postmortem liver labels from the viewpoint of describing postmortem liver shapes

The remainder of this chapter is organized as follows. In section 2.2, I discuss the relationship between SSMs built from *in vivo* livers and postmortem livers. Section 2.3 proposes algorithms for the transformation from *in vivo* livers to postmortem livers, and compares SSMs trained using different sets of synthesized postmortem liver labels, followed by conclusions for this chapter in Section 2.4.

2.2 Relationship between SSMs of an *in vivo* liver and a postmortem liver

2.2.1 Level set distribution model

I investigated the relationship between SSMs trained using *in vivo* liver data and postmortem liver data in terms of performance in describing postmortem livers. This study focuses on a level set distribution model (LSDM) [9] that does not require correspondence between boundaries of shape labels. Here, a shape label was manually drawn by experts, where each voxel value is one inside a liver and zero outside. It is simply called a label in the remainder of this paper.

Given a set of N binary labels I_i ($i = 1, \ldots, N$), each shape I_i is embedded in the zero level set of the signed distance function of I_i. Let $\boldsymbol{\phi}_i$ be a $d \times 1$ feature vector constructed from the signed distance function of I_i , where d is the number of voxels. I call this feature space a level set space. I employed a weighted distance function defined by $\boldsymbol{\varphi}_i = W\boldsymbol{\phi}_i$ that was reported to be superior to the conventional distance function [43]. $W = diag\,(w_1, \ldots, w_d)$ is a weight matrix, where w_k is computed by

$$w_k = \frac{1}{N}\sum_{i=1}^{N}\frac{1}{1+\exp\left(\gamma\left|\phi_k^i\right|\right)} \tag{2.1}$$

with γ determined empirically.

Principal component analysis (PCA) is applied to the set of weighted distance vectors $\boldsymbol{\varphi}_i$ to construct an eigenshape space or an SSM. The principal components and scores can be used to reconstruct a weighted distance vector of a shape as

$$\boldsymbol{\varphi}_i \approx \boldsymbol{\mu} + U\boldsymbol{\alpha} \tag{2.2}$$

where $\boldsymbol{\mu} = \frac{1}{N}\sum_{i=1}^{N}\boldsymbol{\varphi}_i$ is an average vector. $U = [\boldsymbol{u}_1, \ldots, \boldsymbol{u}_t]$ is a matrix whose j-th column is the j-th principal component vector and $\boldsymbol{\alpha} = [\alpha_1, \ldots, \alpha_t]^\top$ is a coefficient

vector, where t is the number of principal components. A shape can be reconstructed by binarizing the weighted distance function with a zero threshold value.

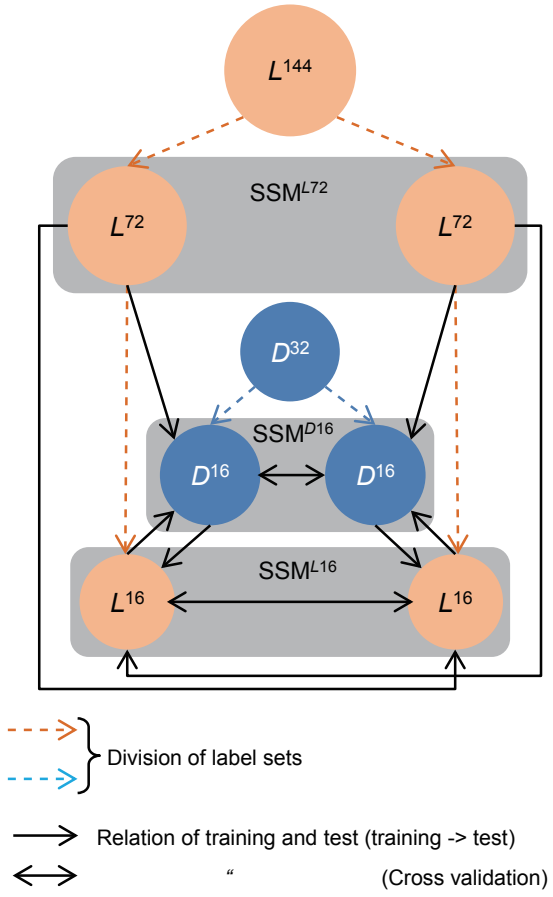

Fig. 2.1 Illustration for label set divisions (*dashed lines*) and the relationship between training and test data (*solid lines*) for performance evaluations of the three SSMs

2.2.2 Materials, performance indices, and SSMs to be compared

I used datasets of 144 *in vivo* (living) liver labels, L^{144} and 32 postmortem (dead) liver labels, D^{32}. The labels were manually delineated on non-contrast CT volumes of size 512×512×191–3201 voxels and were reduced to 170×170×170 voxels for the sake of computational efficacy (voxel size: 2.0-mm isotropic). The study was approved by the ethics committee of Chiba University. A spatial standardization was carried out so that the gravity points of the labels were identical among the training datasets.

Training and testing datasets were required to evaluate the generalization and specificity of the SSMs, which will be explained in detail in "Evaluation of SSMs" section. The L^{144} and D^{32} sets were randomly divided into two equally sized subsets, named L^{72} and D^{16}. In addition, two L^{16} subsets were randomly extracted from the two L^{72} subsets, as shown by the dashed lines in Fig. 2.1. This study constructed three SSMs, namely SSM^{L72}, SSM^{L16}, and SSM^{D16}, which were built from subsets L^{72}, L^{16}, and D^{16}, respectively. The constructed SSMs were evaluated using the L^{16} and D^{16} subsets that were not used for training. The relationship between the training and test data is represented by the solid lines in this figure. For the sake of consistency, the size of the test labels used to evaluate the SSMs was fixed at 16 throughout the study.

The main objective of SSM is to provide a probability distribution for the shape that an object can assume. Therefore, as mentioned in [44] and [45], the following properties are desired for SSMs.

- *Generalization* : The ability to describe instances outside the training set.
- *Specificity* : The ability to represent only valid instances of the object.

Based on [44], I define the generalization and the specificity indices used to evaluate the performance of my SSMs. Furthermore, I define the sum of the two indices of each SSM as the overall performance index of the SSM. Further details on the computation of the generalization and specificity are shown in Fig. 2.3 and are described in the following subsections.

Generalization

Generalization is a measure of the ability to describe unknown shapes. This is a fundamental property because it allows a SSM to learn the characteristics of an object class from a limited training set. If the SSM is overfitted to the training set, it will be unable to generalize to unknown examples. Generalization is defined as an average of Jaccard indices (JIs), each of which is calculated between an unknown shape S_n ($n = 1, \ldots, N$) in a test dataset and its reconstructed shape $\hat{S}_n$ by projection of the shape into the eigenshape space and back projection from the eigenshape space constructed using the training shapes:

$$(\textit{Generalization}) = \frac{1}{N} \sum_{n=1}^{N} JI(S_n, \hat{S}_n) \tag{2.3}$$

where N is the number of test shapes and $JI(S_n, \hat{S}_n)$ is a Jaccard index between S_n and $\hat{S}_n$. The JI between two regions A and B was computed by

$$JI(A, B) = \frac{|A \cap B|}{|A \cup B|} \tag{2.4}$$

where the size $|\cdot|$ means the volume of a region.

Specificity

Another important measure is specificity. A specific SSM should only generate instances of the object class that are similar to those in the test shapes. It is useful to assess this quantitatively by generating instances using the SSM and comparing them with the test shapes. To compute specificity, a large number of arbitrary shapes $\{R_1, \ldots, R_M\}$ were generated from the eigenshape space, using normal random numbers for the coefficient vectors of Eq. (2.2). Typically, the number of arbitrary shapes M was set as 5,000 in this study. The maximum value of the JI between the generated shape and the test shapes was computed and averaged over the generated shapes.

$$(Specificity) = \frac{1}{M} \sum_{m=1}^{M} \max_{n \in \{1,\ldots,N\}} JI(S_n, R_m) \tag{2.5}$$

The number of principal components t of each SSM was chosen such that the cumulative contribution ratio was equal to 0.95 and was determined empirically. The weighting parameter γ for the level set was set to 0.25, at which value the SSM^{D16} showed the highest performance in generalization, and was fixed throughout the experiment.

2.2.3 Results and discussion

Figure 2.2 shows box plots of JIs computed for the generalization and specificity of SSM^{L72}, SSM^{L16}, and SSM^{D16}, and the sums of both indices. Note that both indices of all models were computed individually using L^{16} and D^{16} subsets not used for training. For example, two D^{16} subsets were used to evaluate SSM^{D16} in a cross-validated manner. Subsequently, they were employed again to validate SSM^{L16} as well as SSM^{L72}, as indicated by the solid arrows whose arrowheads point to D^{16} in Fig. 2.1. The results of the latter experiment indicated a difference in performance when applying an SSM to data with different types of deformation, as shown in Fig. 1.2. Statistical tests were carried out between two SSMs under the null hypothesis

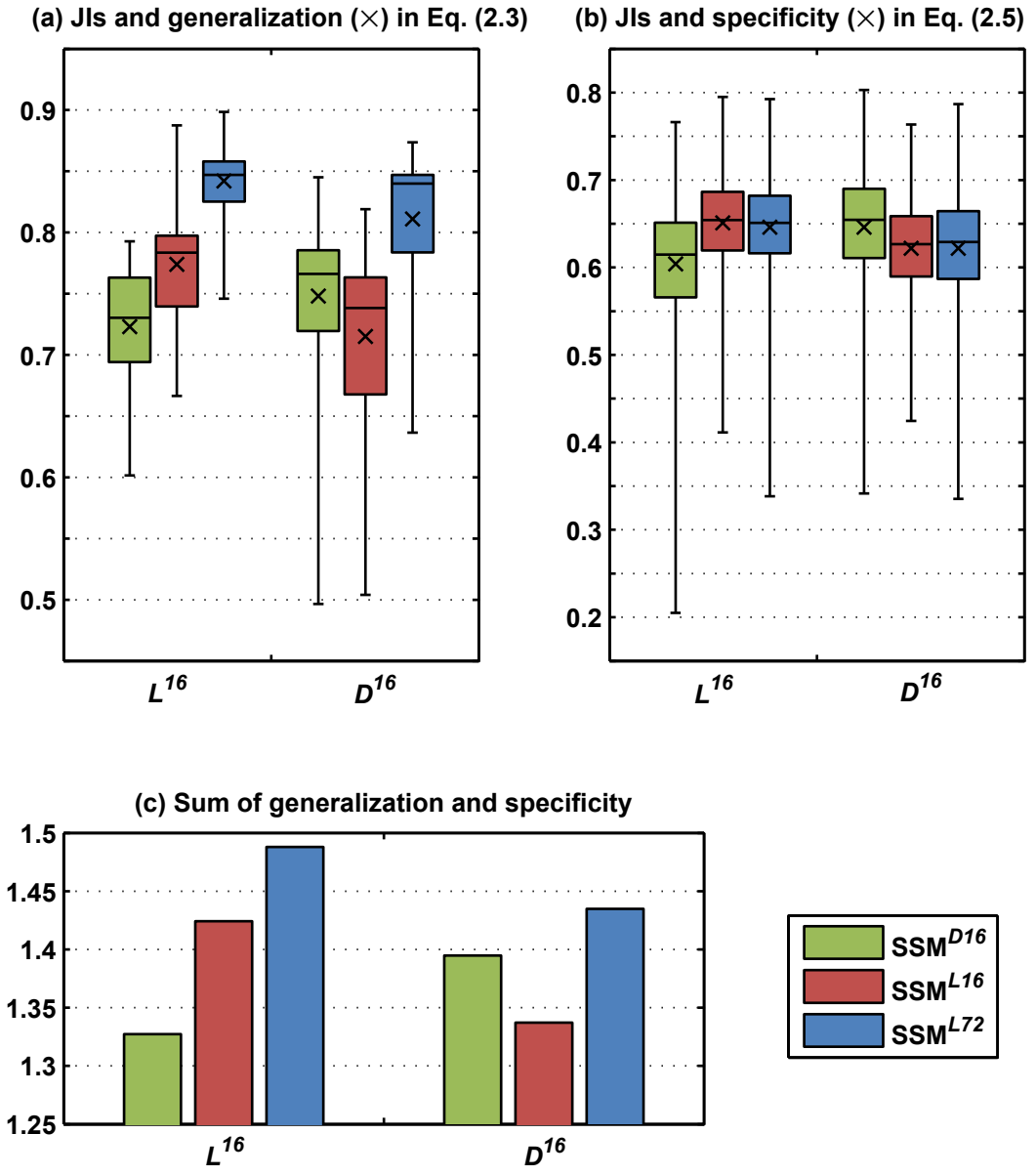

Fig. 2.2 Generalization, specificity, and the sum of both indices of the SSMs. Each model was evaluated individually using D^{16} and D^{16}. The *box plots* in (a) and (b) show the distributions of JIs in Eqs. (2.3) and (2.5), respectively, where the whiskers denote the range from the minimum to the maximum and the crosses indicate generalization and specificity, respectively. (a) JIs and generalization (*multiplication sign*) in Eq. (2.3). (b) JIs and specificity (*multiplication sign*) in Eq. (2.5). (c) Sum of generalization and specificity

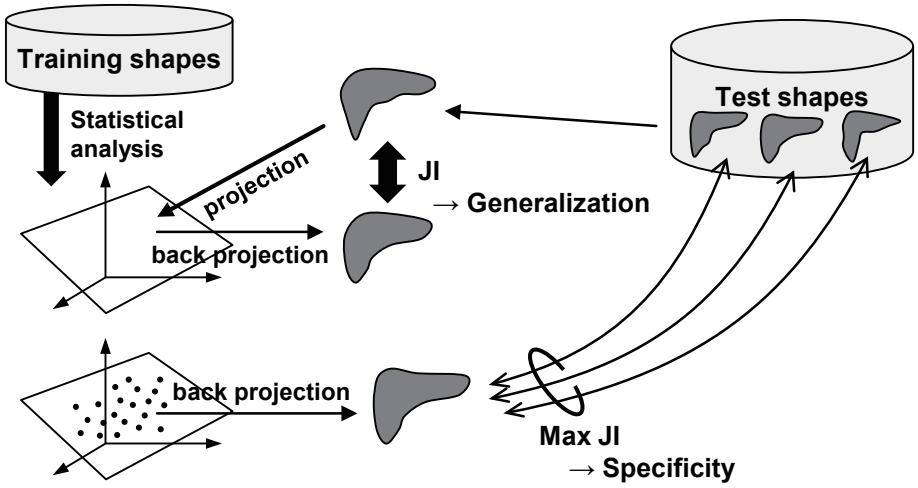

Fig. 2.3 Illustration of the performance indices of the SSMs. Generalization is the average of Jaccard indices (JIs) between test shapes and the back-projected shapes from an eigenshape space. Specificity is the average of maximum JIs between artificial shapes, based on random numbers and the test shapes

H0: *two JI distributions of the SSMs are statistically identical*. The significance level was fixed at 0.05 throughout this study. I individually performed a Wilcoxon matched-pairs test for generalization and a Mann–Whitney U test for specificity. Note that no statistical test can be defined on the sum of both indices, because it is a scalar value.

From the experimental results, the following were observed:

1. The performance when applying an SSM to data with the same types of deformation was always superior to those applying an SSM to data with different types of deformation. For example, generalization of SSM^{D16} evaluated by D^{16} was higher than that of SSM^{L16} evaluated by D^{16}, with a statistically significant difference. A similar relationship was observed not only in generalization, but also in specificity. Consequently, the sum of both indices presents an analogous relationship in the magnitude of the sum.

2. When increasing the number of training labels from 16 to 72, the generalization of SSM^{L72} was greatly improved compared to SSM L16. Consequently, even when evaluating with D^{16}, the generalization of SSM^{L72} was much higher than that of SSM^{D16}, with a statistically significant difference. In contrast, there was no clear evidence that the specificity of an SSM for a postmortem liver could be increased by increasing the number of training labels.

3. The sum of both indices of SSM^{L72} was improved by increasing the number of training labels due to an improvement in generalization.

The first observation suggests that the performance of an SSM constructed using *in vivo* liver labels suffers when describing postmortem liver shapes. The second and third observations indicate that a larger number of training labels are required to improve the performance of the SSM, particularly from the viewpoint of generalization. *In vivo* liver labels might be helpful in training an SSM for a postmortem liver to an extent, but the performance of an SSM constructed using *in vivo* livers would suffer when describing the specific shape of a postmortem liver (see Sections 2.3.4 and 2.3.5 for more details). In addition, because of the shortage of postmortem liver CT and label volumes, it is impossible to increase the number of postmortem liver labels for training.

2.3 SSM for a postmortem liver based on synthesized-based learning

2.3.1 Synthesis of postmortem liver labels from *in vivo* liver labels

In this section, I present three transformation methods to simulate the changes in shape from *in vivo* livers to postmortem livers, which are categorized into a geometrical transformation F_A and two statistical transformations, F_T and F_{TR}. I define the respective transformations as follows:

- $F_A : L \rightarrow \tilde{D}_A$ (geometrical)
- $F_T : L \rightarrow \tilde{D}_A$ (statistical)
- F_{TR}: $L \rightarrow \tilde{D}_A$ (statistical)

where L is a set of *in vivo* (living) liver labels.

Geometrical transformation

I define a geometrical transformation F_A as an affine transformation of *in vivo* liver shapes in real 3D space. I formulate an affine transformation $T_M : \Omega \rightarrow \Omega$ over the

domain of the images, $\Omega \subset \mathbb{R}^3$, as

$$T_M(x) = M(x - g) + g \tag{2.6}$$

where M is a 3×3 affine transformation matrix, and the symbol g denotes the gravity point of the liver labels. It is ensured that the gravity point of the label is constant before and after the transformation. Let *in vivo* liver label $I_L \in L$ be the function $I_L \to \{0, 1\}$. I define a synthesized postmortem liver $\tilde{I}_A \in \tilde{D}_A$ as

$$I_A = I_L \circ T_{M^*} \tag{2.7}$$

The optimal affine matrix M^* is obtained by minimizing the surface distance between the mean shape of *in vivo* livers $\overline{I_L}$ and that of postmortem livers $\overline{I_D}$, which can be formulated as

$$M^* = \arg\min_M d_{surf}(\overline{I_D}, \overline{I_L} \circ T_M) \tag{2.8}$$

where $d_{surf}(\cdot, \cdot)$ is the surface distance between two mean shapes that were constructed from *in vivo* liver label set L^{72} and postmortem liver label set D^{16}, respectively. The matrix M is initially set to the unit matrix and optimized using the Nelder-Mead method [46]. Finally, the obtained optimal affine transformation matrix M^* is applied to all *in vivo* liver labels in the L^{72} set so as to synthesize postmortem liver labels $\tilde{D}_A$.

Statistical transformation

I introduce two types of statistical transformation methods that apply linear transformations to the distribution of *in vivo* liver shapes in a level set space. The first transformation $F_T : L \to \tilde{D}_T$ is defined as a translation such that the mean of *in vivo* liver labels $\boldsymbol{\mu}_L$ is equal to that of postmortem liver labels $\boldsymbol{\mu}_D$ in a level set space, as shown in Fig. 2.4:

$$\boldsymbol{\phi}_T = \boldsymbol{\phi}_L + (\boldsymbol{\mu}_D - \boldsymbol{\mu}_L). \tag{2.9}$$

where $\boldsymbol{\phi}_L$ is a feature vector constructed from a signed distance function of a liver label, as explained in section 2.2.1.

The second method $F_{TR} : L \to \tilde{D}_{TR}$ performs a translation followed by a rotation such that the axes of the eigenshape space $U_L\,[l_1, \ldots, l_t]$ of *in vivo* livers coincide

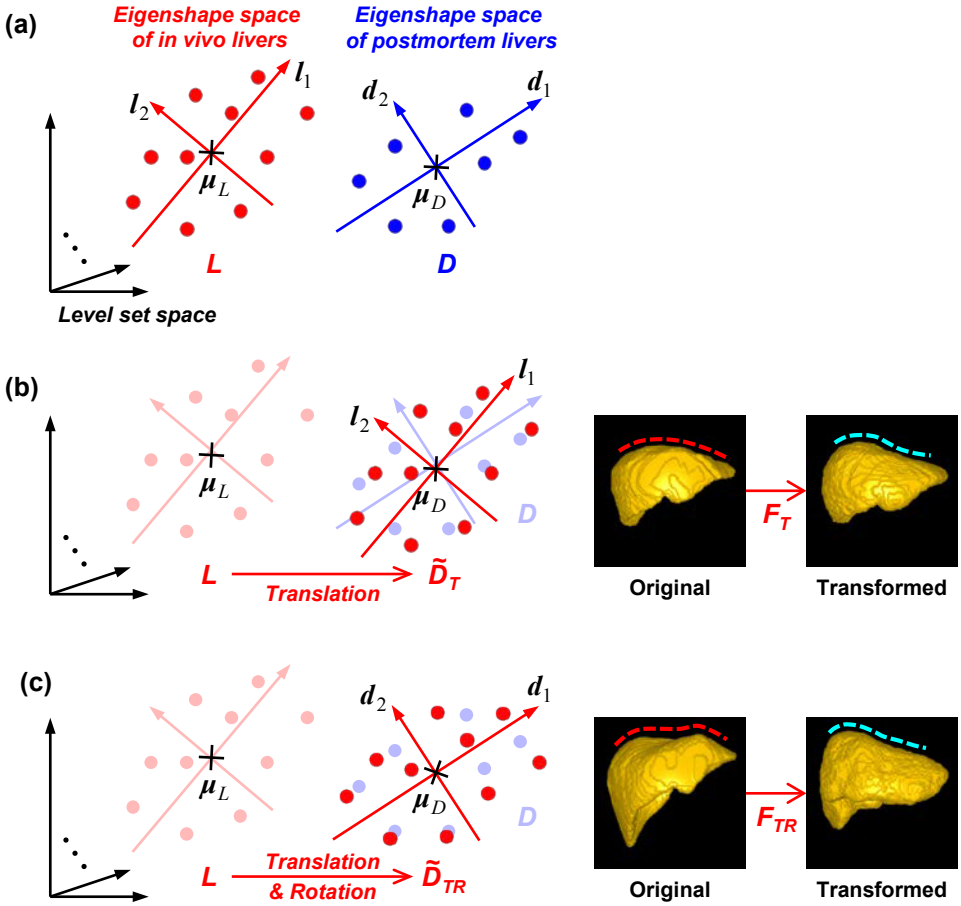

Fig. 2.4 Statistical transformations from *in vivo* livers to postmortem livers in a level set space. **(a)** The original relationship between the eigenshape spaces of *in vivo* livers and postmortem livers. **(b)** Transformation by translation of the postmortem liver label distribution. **(c)** Transformation by translation followed by rotation so that the coordinates of the eigenshape space of postmortem livers are identical to those of *in vivo* livers

with those of postmortem livers $U_D = [d_1, ..., d_t]$:

$$\boldsymbol{\phi}_{TR} = U_D U_L^{+}(\boldsymbol{\phi}_L - \boldsymbol{\mu}_L) + \boldsymbol{\mu}_D \tag{2.10}$$

where U_L^{+} is a Moore-Penrose pseudo-inverse of U_L.

2.3.2 SSMs to be compared

Figure 2.5 presents a workflow for constructing an SSM for a postmortem liver. Given *in vivo* (living) liver labels L and postmortem (dead) liver labels D, artificial postmortem liver labels $\tilde{D}$ are synthesized by transforming *in vivo* liver labels L to resemble postmortem liver labels. Then, $\tilde{D}$ is combined with D, and the "$D + \tilde{D}$" set is used to build an SSM for a postmortem liver.

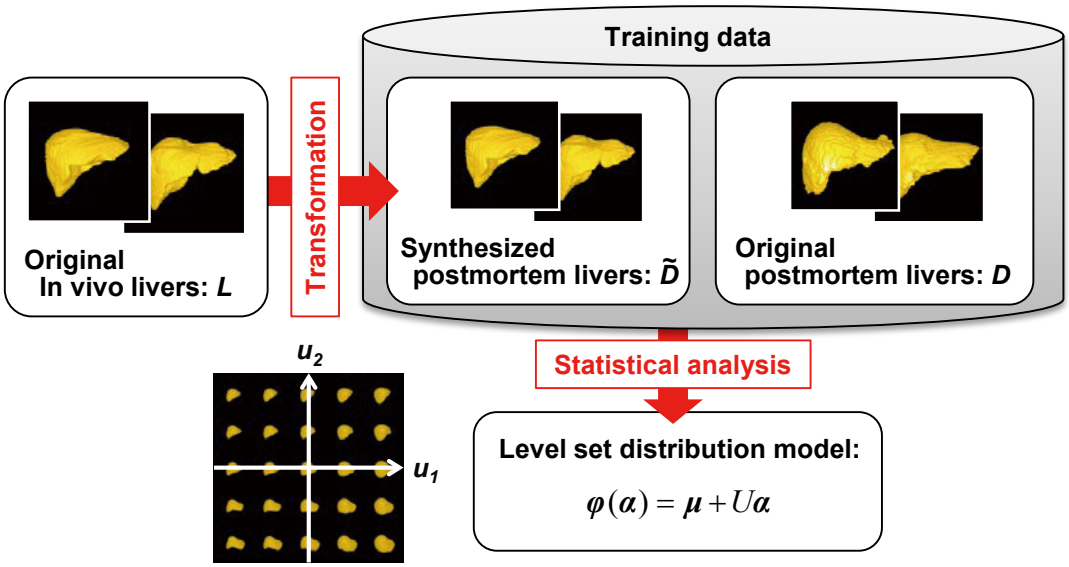

Fig. 2.5 Illustration of workflow of the proposed SSM construction

In this study, five SSMs were built. Three SSMs were constructed using the three label sets $\tilde{D}_T$, $\tilde{D}_{TR}$, and $\tilde{D}_A$. The remaining two SSMs were built using synthesized labels $\tilde{D}_{AT}$ and $\tilde{D}_{ATR}$, which were synthesized by applying transformations F_T and F_{TR} to $\tilde{D}_A$, respectively. Note that an eigenshape space was recomputed from $\tilde{D}_A$, and transformations F_T and F_{TR} were defined for the new eigenshape space. The relationships between the five SSMs and the five synthesized liver label sets for training are summarized as follows, where the training label sets are in parentheses.

- $D + T$ model (D and $\tilde{D}_T$)
- $D + TR$ model (D and $\tilde{D}_{TR}$)
- $D + A$ model (D and $\tilde{D}_A$)
- $D + AT$ model (D and $\tilde{D}_{AT}$)
- $D + ATR$ model (D and $\tilde{D}_{ATR}$)

2.3.3 Materials, performance indices, and parameters

To compare the SSMs, the sets of 144 *in vivo* liver labels L and 32 postmortem liver labels D were employed again and randomly divided into training labels and testing labels. These labels are the same as those mentioned in Section 2.2.2. All SSMs compared in this section were assessed in terms of generalization and specificity using two D^{16} subsets, where a test label set was separated from a training label set as explained in Section 2.2.2. I set the weighting parameter γ for the level set and the number of the generated shapes for specificity to be the same as the values in Section 2.2.2. The number of principal components t for each SSM was also decided in the same manner described in that section.

2.3.4 Results

Figure 2.6 summarizes the performance of the three conventional and five proposed SSMs in terms of generalization, specificity, and the sum of both indices. It was found that the $D + A$ model was best in terms of generalization, while the $D + T$ model was best in terms of specificity. I compared the performances of the eight SSMs and performed a statistical analysis of the results. Table 2.1 shows the results of the statistical tests of all possible pairs among the eight SSMs; the significance level and statistical tests used in this section are the same as those used in Section 2.2.3.

2.3.5 Discussion

From Table 2.1, it was found that the $D + L$, $D + T$, and $D + AT$ models were statistically identical to the best $D + A$ model in terms of generalization, and the $D + AT$ model was statistically the same as the best $D + T$ model in terms of specificity. Thus, the $D + T$ and $D + AT$ models that were the logical products of

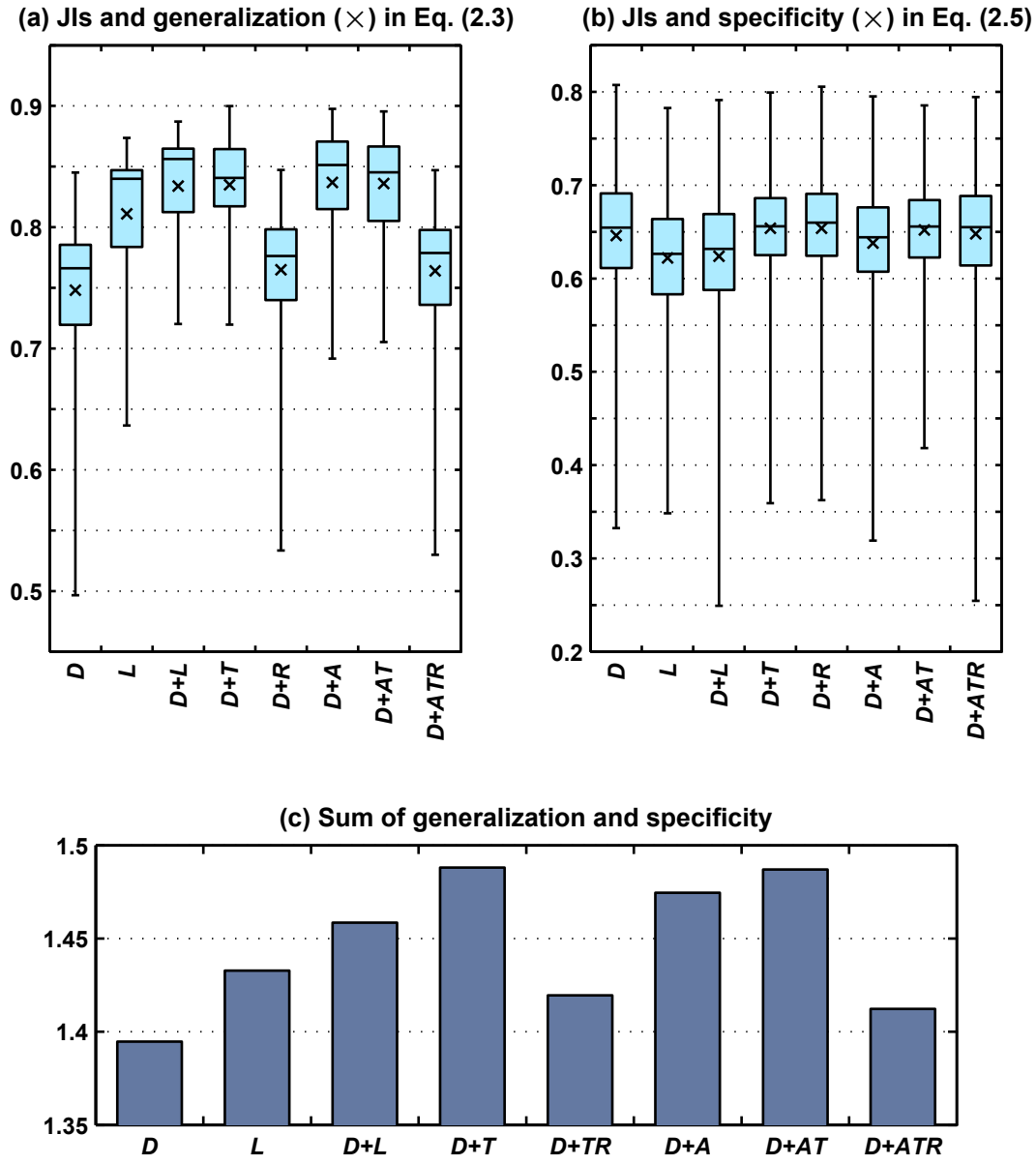

Fig. 2.6 Generalization, specificity, and the sum of both indices of the three conventional SSMs and five proposed SSMs. Each model was evaluated using two D^{16} subsets. (a) JIs and generalization (*multiplication sign*) in Eq. (2.3). (b) JIs and specificity (*multiplication sign*) in Eq. (2.5). (c) Sum of generalization and specificity

Table 2.1 Results of statistical significance tests for all pairs among the eight SSMs evaluated. † shows the statistical difference in generalization was observed at $p < 0.05$; ‡ indicates the statistical difference in specificity was observed at $p < 0.05$

	D	L	$D+L$	$D+T$	$D+TR$	$D+A$	$D+AT$
$D+ATR$	†, ‡	†, ‡	†, ‡	†, ‡	‡	†, ‡	†
$D+AT$	†	†, ‡	‡		†, ‡	‡	
$D+A$	†, ‡	†, ‡	‡	‡	†, ‡		
$D+TR$	†, ‡	†, ‡	†, ‡	†, ‡			
$D+T$	†, ‡	†, ‡	‡				
$D+L$	†, ‡	†, ‡					
L	†, ‡						

$\{D+L, D+T, D+A, D+AT\}$ and $\{D+T, D+AT\}$ were considered to be superior to other SSMs in terms of both performance indices. When the sum of both indices was computed, the $D+T$ model achieved the highest score. Therefore, I concluded that the $D+T$ model was the best model in this study. In the remainder of the discussion, I will explore the $D+T$ model further.

First, I compared the best model with the conventional SSMs, that is, the D, L, and $D+L$ models, based on Fig. 2.6 and Table 2.1. All experimental results showed that the conventional models were inferior to the proposed best $D+T$ model, except for the generalization of the $D+L$ model. It was found from Table 1 that the generalization of the $D+L$ model was statistically identical to that of the best model. However, the specificity of the $D+L$ model was significantly lower than that of the best model. The lower specificity of the $D+L$ model will be discussed further in the fourth paragraph of this section.

My second topic concerns the generalization of the SSMs. Figure 2.7 shows errors between the true shape and the reconstructed shapes from the eigenshape spaces of eight SSMs (see "Level set distribution model" section for the reconstruction). The colors represent the reconstruction error, and were mapped onto the true surface. The numerals are JIs, and a higher JI denotes greater generalization. In these figures, the $D+A$ model showed the highest JI, which was consistent with the results from Fig. 2.7 a. One of the reasons why the $D+A$ model achieved the highest performance in generalization is that reconstruction errors were suppressed, especially in the area of the left lobe and the top of the right lobe, as indicated by the arrows in 2.7.

My third topic relates to the specificity of SSMs. Specificity is the ability to exclude unnatural shapes from the eigenshape space of an SSM. Figure 2.8 shows shapes from eigenshape spaces, which were generated from a uniform sampling of

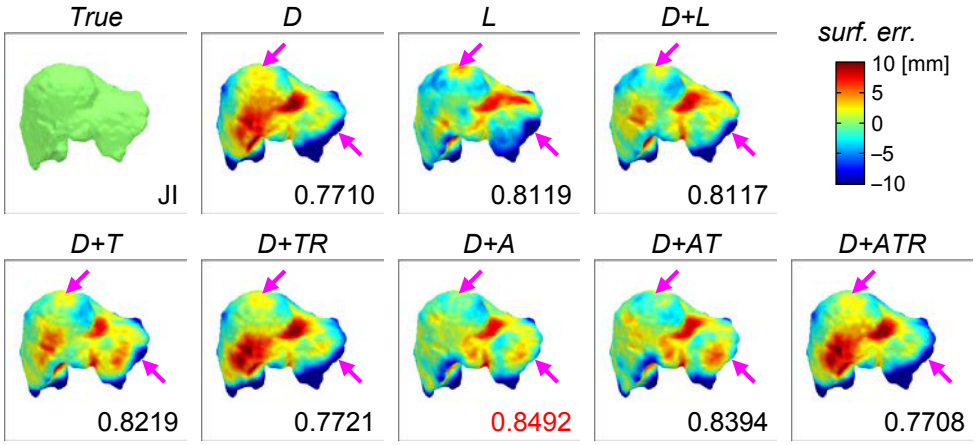

Fig. 2.7 A postmortem liver and its reconstructed shape from each SSM with a color display of surface error between the true shape and the reconstructed shape

the coefficients α_1 and α_2 in Eq. (2.2) from -2 sigma to $+2$ sigma, with an interval of one sigma. The red color indicates that the maximum JI between a shape and the test postmortem liver shapes was lower than 0.6, which means that the shapes were different from postmortem ones, or unnatural shapes. It was found from Fig. 2.2 that the $D + T$ and $D + AT$ models generated only two unnatural shapes, but conventional SSMs generated five to seven unnatural shapes. These observations support the above discussions about specificity: (i) the $D + T$ and $D + AT$ models were superior to other SSMs in terms of specificity, and (ii) the conventional $D + L$ model can be a good model in terms of generalization, as mentioned in the first paragraph. However, its low specificity is problematic, as shown in Fig. 2.8, resulting in it being inferior to the proposed models. Here, I discuss the reasons why the $D + T$ model achieved the highest performance in specificity. Generally speaking, using good shapes for training helps to achieve higher specificity, where a *good shape* is one that resembles the shape of a test label. Table 2.2 shows the similarity between the 144 artificial postmortem liver labels in $\tilde{D}_T$ used for training and the 32 actual postmortem liver labels used for testing. Similar to the computation of specificity, the maximum of JIs between an artificial label for training and actual labels for testing was computed for each artificial label and averaged over all the artificial labels. The higher the JIs, the more the artificial liver shapes resemble actual postmortem liver shapes. Table 2.2 shows that $\tilde{D}_T$ contained better shapes than other

synthesized label sets, and the results showed the $D + T$ model achieved the best performance in terms of specificity.

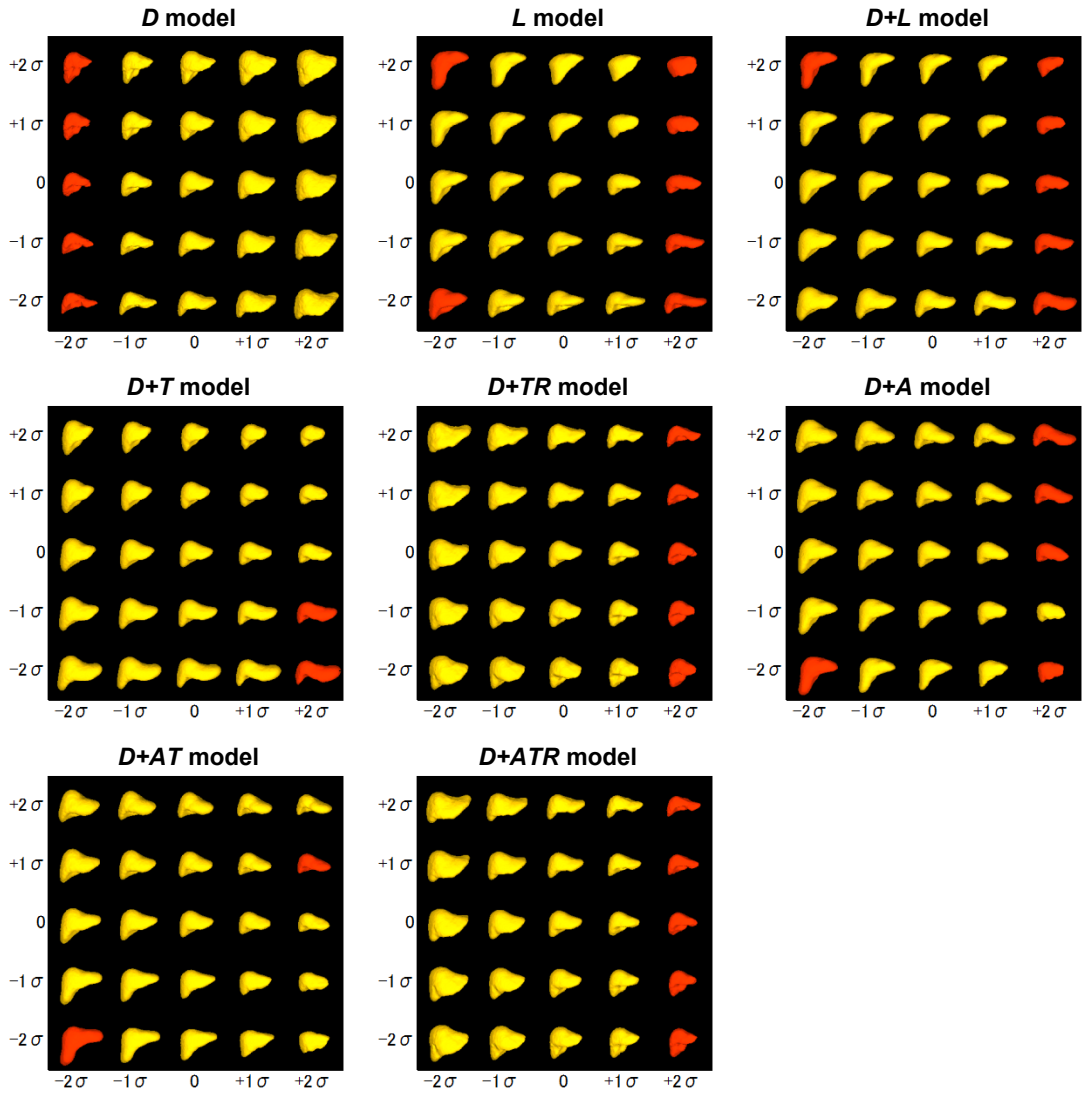

Fig. 2.8 Shapes from the eigenshape space of each SSM. Shapes were generated from a uniform sampling of coefficients α_1 and α_2 of the SSMs. The *red color* indicates that the maximum JI between a shape and the postmortem liver shapes was lower than 0.6, which means that the shapes did not resemble postmortem livers

My fourth topic is the effect of the number of principal components t and the weighting parameter γ on the performance indices of the SSM. Figure 2.9 shows changes in the performance indices (generalization and specificity) of the $D + T$ model as γ and t changed. Note that the actual values of t for the proposed $D + T$

Table 2.2 Similarity between the synthesized labels for training and actual labels for testing

$\tilde{D}_T$	$\tilde{D}_{TR}$	$\tilde{D}_A$	$\tilde{D}_{AT}$	$\tilde{D}_{ATR}$
0.6572	0.6486	0.6365	0.6554	0.6366

model were 26 and 28 in the crossvalidation test. The performance indices seemed to be sensitive to changes in the weighting parameter γ when $\gamma < 0.2$, and insensitive when $\gamma \geq 0.2$. On the other hand, while changing t affected the performance indices when t was small, the effects on the indices were limited when t was large. When considering the values employed in this study ($\gamma = 0.25$, $t = 26$, 28 for the $D + T$ model), I supposed that the perturbations around γ and t would have a marginal effect on the performance indices, and would result in similar conclusions.

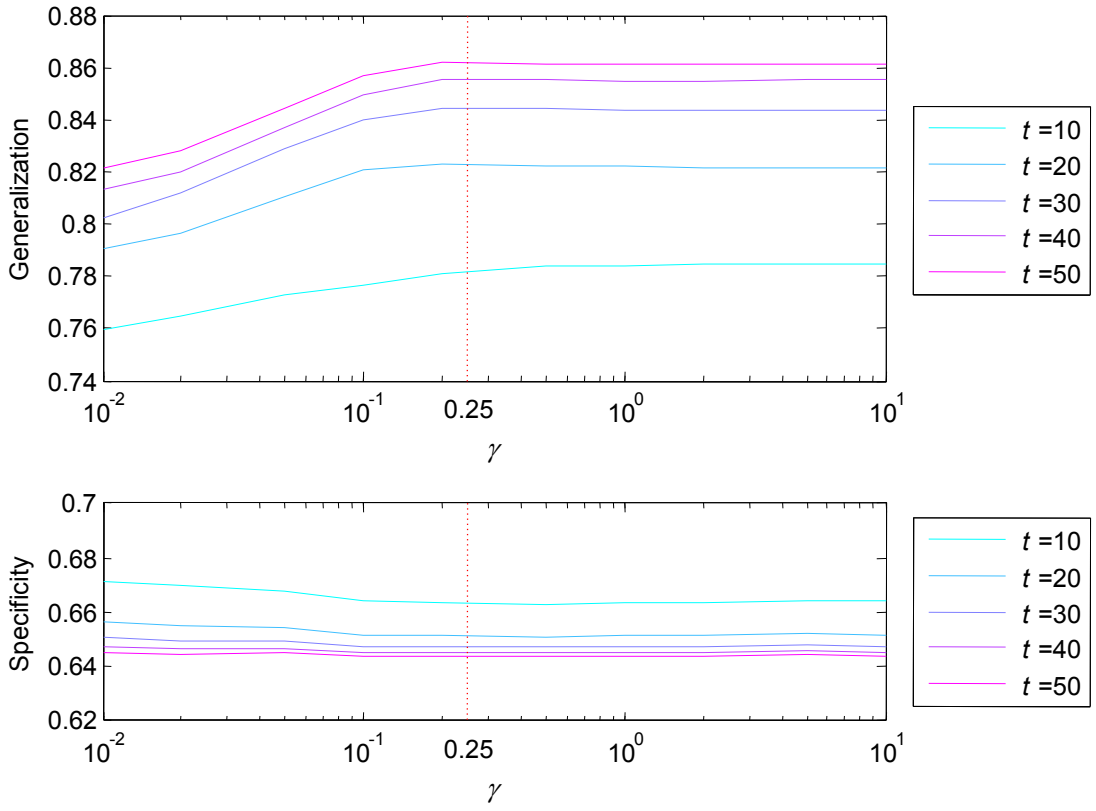

Fig. 2.9 Relations between parameters and performance indices. Top generalization, bottom specificity. The red dotted line indicates the value of γ I adopted

My final topic is the validation of the proposed transformation using actual pairs of *in vivo* and postmortem livers obtained from the same subjects. Figure 2.10 shows three pairs of images scanned from three subjects. If the proposed transformations are suitable to simulate the changes between an *in vivo* liver and a postmortem one, the JI between a true postmortem liver shape and a synthesized shape transformed from an *in vivo* liver should be higher than that of a shape without transformation. Figure 2.11 shows the results of applying the transformations to an *in vivo* liver label from case 1 to simulate the changes to a postmortem liver. The numerals show the JIs between synthesized postmortem liver shapes and the true postmortem liver shape from the same subject. It was found from the figures that the simulation composed of F_A (affine transformation in 3D space) followed by F_T (translation in level set space) achieved the best score, and the second and third best were simulations by F_A and F_T, respectively. All of these were concluded to be superior to other SSMs in terms of both indices or generalization. It is worth mentioning that the important characteristic of a postmortem liver was simulated well by these transformations (the right lobe tends to go up, and the left lobe tends to go down). Figure 2.12 shows the JIs of all transformations from the three cases; it was confirmed that the JIs of postmortem liver shapes transformed by F_T, F_A, and F_{AT} were higher than those of shapes without transformation.

2.4 Conclusions

This chapter reported a study on a SSM for a postmortem liver in autopsy imaging and its application to liver segmentation from PMCT volumes. First, the relationship between SSMs constructed from *in vivo* liver labels and those from postmortem ones was investigated. Second, I proposed several algorithms to transform *in vivo* liver labels to resemble postmortem liver labels. Third, I conducted a comparative study on SSMs for a postmortem liver constructed using the transformed labels.

On investigating the relationship between SSMs using 144 *in vivo* liver labels and 32 postmortem liver labels, I concluded that an SSM constructed using *in vivo* liver labels suffered from inaccuracy when describing postmortem liver shapes. In addition, a larger number of training labels were required to enhance the performance of an SSM. In accordance with these conclusions and to solve the problem of the shortage of postmortem liver labels, I proposed several geometrical and statistical transformations to synthesize postmortem liver labels from *in vivo* liver labels. Using the proposed SSMs constructed from synthesized liver labels, I developed

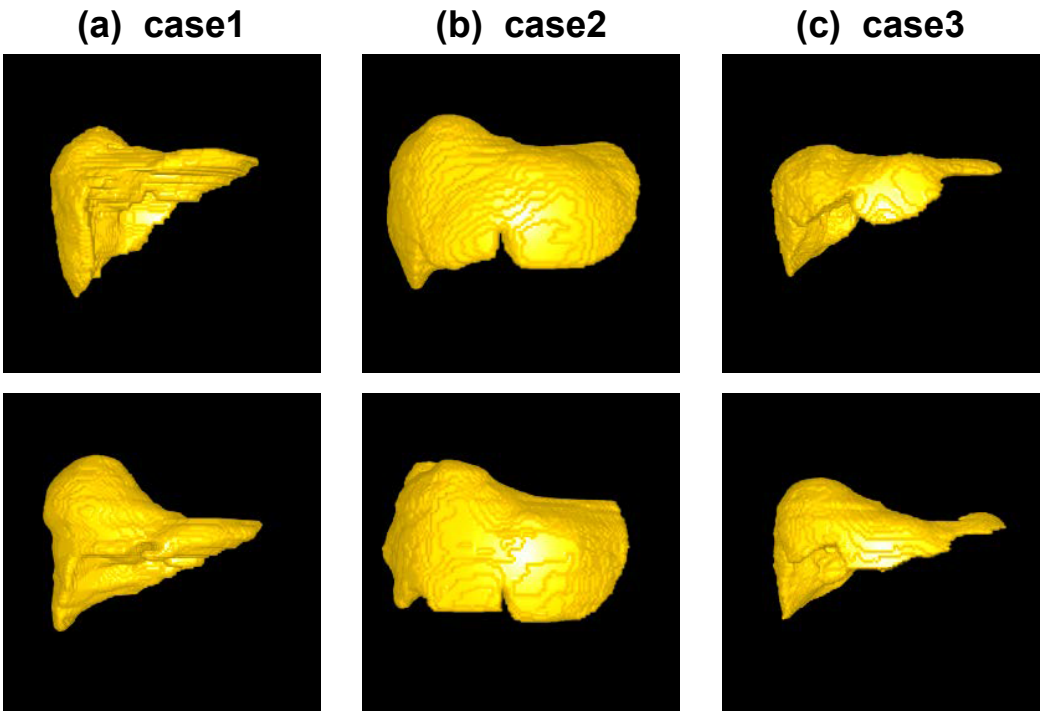

Fig. 2.10 Three pairs of *in vivo* livers (*upper*) and postmortem livers (*lower*); each pair was scanned from the same subject before and after death

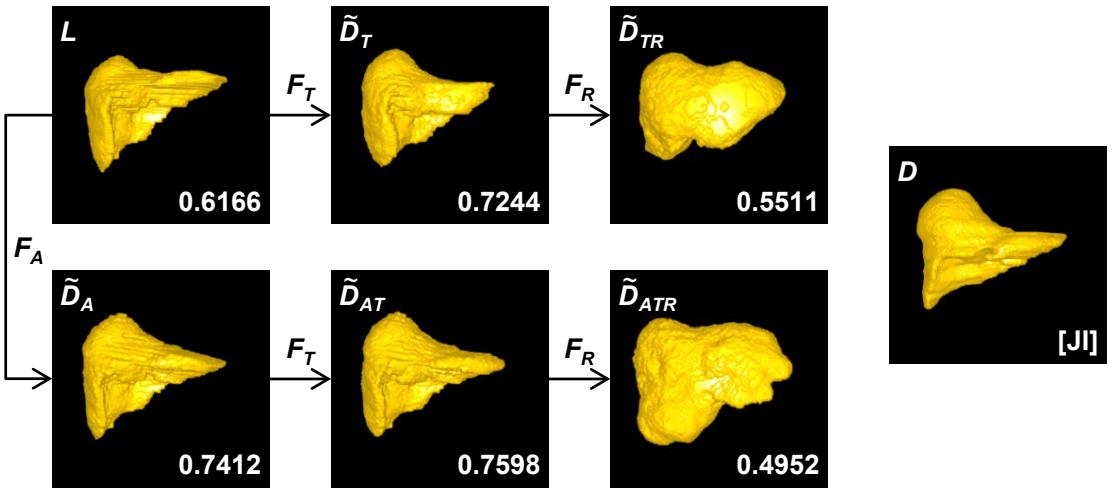

Fig. 2.11 Transition in the shapes between the transformed shapes and the true postmortem liver shapes from the proposed transformations and JIs

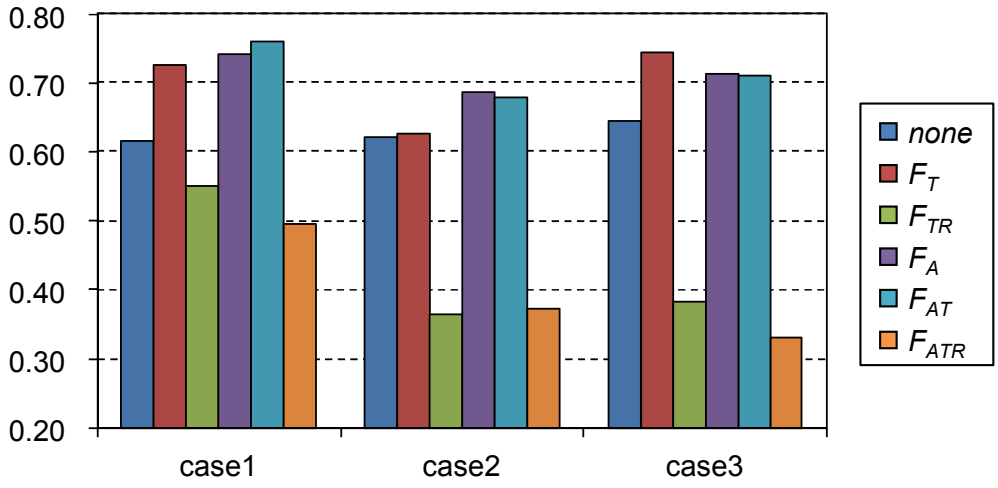

Fig. 2.12 JIs between synthesized postmortem livers and true postmortem livers

a liver segmentation method for PMCT volumes, where the dynamic probabilistic atlas was employed to handle the the Ai specific appearance of the liver. I reached the following conclusions from experiments using 144 *in vivo* liver labels and 32 postmortem liver labels.

1. The best SSM for a postmortem liver in terms of generalization and specificity was the $D + T$ model, trained using postmortem liver labels as well as postmortem liver labels synthesized from *in vivo* ones by a translation operation in level set space. The second best was the $D + AT$ model, and the difference in performance from the best model was statistically insignificant.

2. The best SSMs were confirmed to be statistically superior to conventional (D and L model) SSMs in terms of generalization and specificity for a postmortem liver. Conventional $D + L$ models showed comparable ability with the best model in generalization, but significantly lower specificity performance.

3. $D + L$ model also showed the highest segmentation accuracy and statistically significant improvement from D and L model. Conventional $D + L$ models showed comparable ability with the best model in generalization, but significantly lower specificity performance.

It is worth mentioning the relationships with nonlinear geometrical transformations and physical model-based algorithms, such as the finite element method

(FEM)-based transformations. The advantage of the proposed algorithm lies in the simplicity of simulating the changes. The proposed transformation does not require any additional nonlinear parameters, most of which are difficult to decide appropriately. For example, an FEM-based approach requires boundary conditions and physical parameters of the liver, as well as the forces the liver was subjected to during the transition process from life to death, all of which are very difficult to estimate. An interesting topic for future studies would be to compare the results of this study with results from nonlinear geometrical transformations and an FEM-based approach.

My future plans include applications to other organs, modeling both shape and appearance changes from an *in vivo* body to a postmortem body, and a comparative analysis using a larger amount of Ai data.

Chapter 3

Liver segmentation from PMCT volumes

3.1 Introduction

This section presents an algorithm for automated liver segmentation from a CT volume of a cadaver based on a statistical shape model (SSM), that was proposed in Chapter 2, where a comparative study of the eight SSMs showed that synthesized data were effective for training an SSM to delineate the specific postmortem shape of a liver.

3.2 Methods

3.2.1 Algorithm overview

My algorithm extends the previous liver segmentation algorithm [47], where the authors proposed a graph cut segmentation energy based on an SSM-based shape prior. Figure 3.1 shows the work flow of (a) the previous liver segmentation algorithm designed for *in vivo* livers [47] and (b) the proposed liver segmentation algorithm for Ai.

The previous method consists of three steps: rough segmentation, SSM-based shape estimation, and estimated shape-based graph cuts segmentation. The rough segmentation is performed using an atlas-guided expectation maximization (EM) algorithm followed by maximum a posteriori (MAP) segmentation [1]. The a posteriori probabilities of organs are computed from a mixture of four Gaussians. Subsequently,

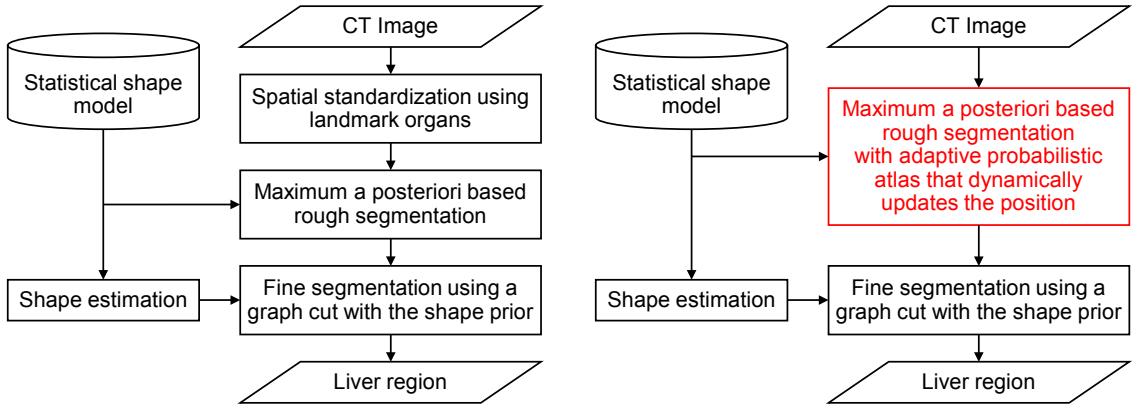

Fig. 3.1 The work flow of the automated liver segmentation algorithm designs: (a) previous method designed for *in vivo* liver; (b) the proposed method designed for Ai

the most similar shape to a MAP segmentation result is extracted from the eigen-shape space of an SSM in the shape estimation process [47]. The average distance between the surface of the MAP segmentation and the reconstructed surface in the eigenshape space is employed as a similarity measure and is minimized by the Nelder-Mead search algorithm [46]. Finally, the graph cut-based segmentation is performed, the energy function of which is similar to that in [47]. My energy function is composed of a unary term and two pairwise terms. The unary term consists of a negative logarithm of posterior probability of liver, given a CT value in which a patient-specific probabilistic atlas generated from the estimated shape is used as a prior probability. Pairwise terms consist of a conventional boundary term and a shape term that evaluates the difference in gradients between the estimated and true shape.

The conventional algorithm [47] employed a spatial standardization based on the non-linear deformation using anatomical landmarks before the segmentation. However, the landmark detection process, which depends on the CT value, may fail because of the postmortem changes described in Section 1.2.2. Therefore, the system was developed without a spatial standardization process. To compensate for the postmortem-specific deformation of organs, I repeated the process of atlas-guided EM and MAP by updating the location of the probabilistic atlas according to the

MAP segmentation result of the previous iteration. The location of the probabilistic atlas is initialized by the gravity point of the liver estimated by the proposed method shown in Section 3.2.2.

3.2.2 Estimation of the gravity point of the liver

This section provides the initial estimation of the gravity point of the liver g_0:(x_0, y_0, z_0). Figure 3.2 shows the outline of the estimation process of g_0.

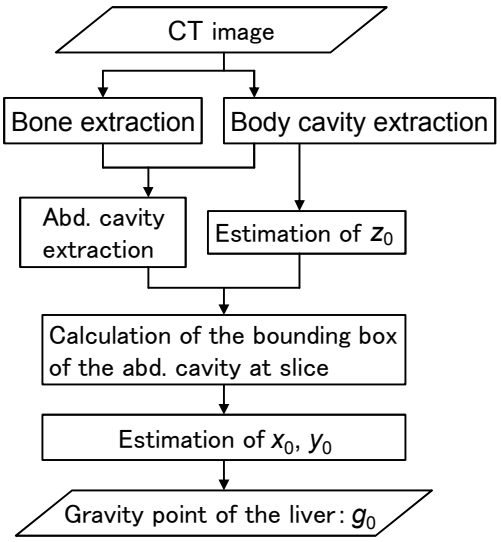

Fig. 3.2 Flow of the estimation of the gravity point of the liver

Body cavity extraction For the body cavity extraction, the trunk of the body and bone are extracted by a simple image processing algorithm, as shown in Algorithms 1 and 2, respectively, which are forwarded to the body cavity extraction algorithm (see Fig. 3.3).

Algorithm 1 Extraction of the trunk of the body

Binarization of X with $thr. = -300$ [H.U.]
Binary morphological opening of X with radius $r = 1$ [voxels]
Dilation of X with $r = 3$ [voxels]
Remove hole region from X
Binary morphological erosion of X with $r = 3$ [voxels]
Extract the largest connected component.

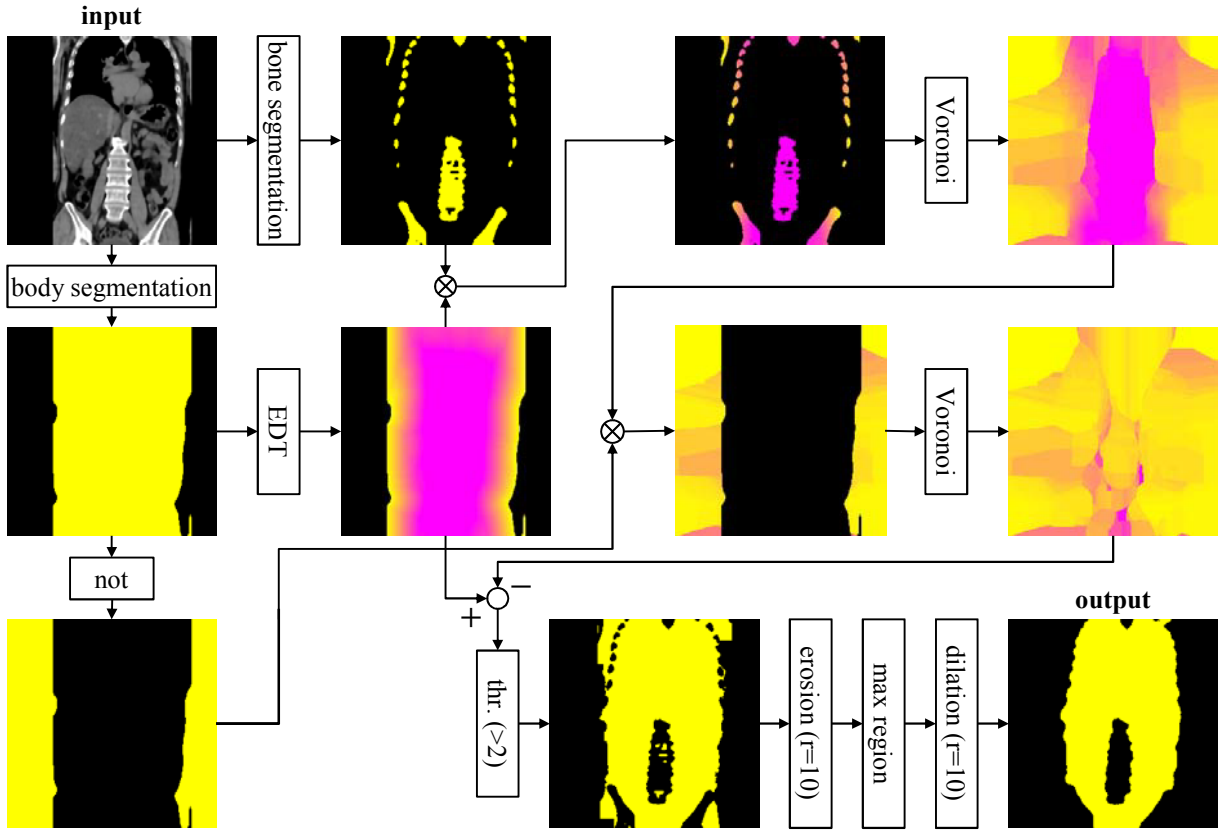

Fig. 3.3 Flow of the body cavity segmentation

Algorithm 2 Extraction of the bone

Require: CT image X
binarize X with $thr. = 100$ [H.U.]
dilate X with $r = 5$ [voxels]
extract maximum volume region from X
erode X with $r = 5$ [voxels].

Estimation of the gravity point of the liver Figure 3.4 shows the estimation process of the gravity point of the liver g_0:(x_0, y_0, z_0), which is used for the initial estimation of the location of the probabilistic atlas. Slice z_0 is calculated as the linear combination of the slices of the shoulder and the upper part of the thigh using the ratio $s_x : (1 - s_x)$. (x_0, y_0) is calculated from the bounding box of the body cavity at slice z_0. Proportion values s_x, s_y, and s_z are trained from the training data.

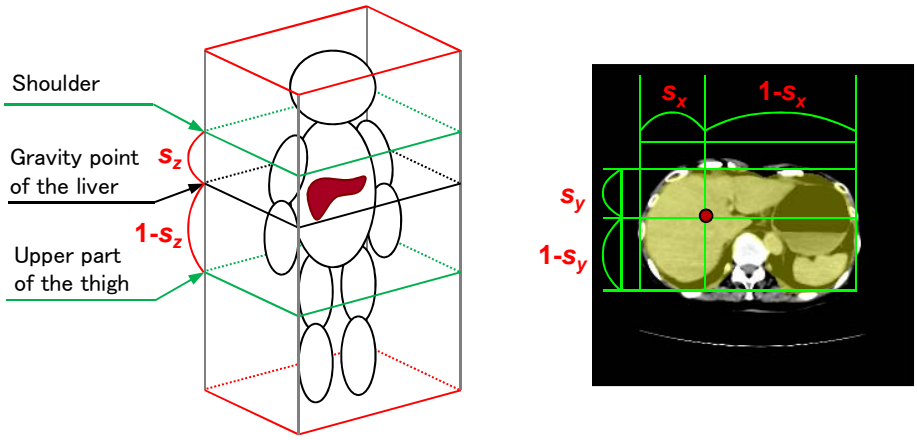

Fig. 3.4 Estimation of the gravity center of the liver. (left: z-coordinate, right: x- and y-coordinates

3.2.3 Rough extraction of the liver with dynamic probabilistic atlas

The rough extraction of the liver is conducted by maximum a posteriori (MAP) segmentation under the given prior probability, *e.g.* , the probabilistic atlas based on the equation.

The posterior probability is calculated from the mixture of Gaussians, the parameters of which are estimated by an atlas-guided EM algorithm [1] (see Appendix A

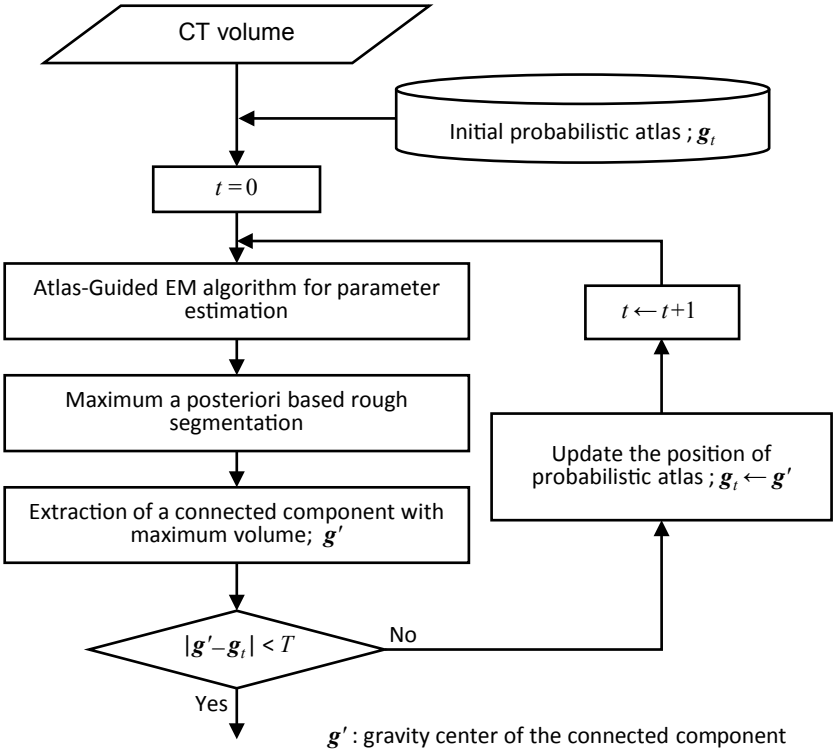

Fig. 3.5 The proposed rough liver extraction algorithm

for details), where the mixture ratio can be defined for each voxel independently

$$p(\boldsymbol{x} \mid \theta) = \frac{1}{N} \sum_{i=1}^{m} \sum_{n=1}^{N} \alpha_i^n \mathcal{N}(\boldsymbol{x}; \boldsymbol{\mu}_i, \Sigma_i) \tag{3.1}$$

where m, $\mathcal{N}$, α_i^n, $\sum_{i=1}^{m} \left(\alpha_i^n = 1\right)$, $\boldsymbol{\mu}_i$, and Σ_i are the number of classes, the number of voxels, the mixture ratio for each class, the mean vector, and the covariance matrix, respectively. $\mathcal{N}$ denotes a multivariate Gaussian distribution with the center $\boldsymbol{\mu}_i$ and the covariance Σ_i. The EM algorithm yields parameters θ_i and $\theta_i = \{\alpha_i^n, \boldsymbol{\mu}_i, \Sigma_i\}$. I used the initial estimation of the mixture ratio α_i^n for the probabilistic atlas generated from SSM.

The next step is the MAP-based (maximum a posteriori) segmentation of the liver based on

$$L(\mathbf{x}) = \arg\min_{l} P(\mathbf{x}|l) \tag{3.2}$$

Then, I calculate $\boldsymbol{g}_t'$, the gravity point of the rough segmentation result obtained from Eq. (3.2), and evaluate the difference between $\boldsymbol{g}_t'$ and the current estimation of the gravity center $\boldsymbol{g}_t$. If the distance $|\boldsymbol{g}_t - \boldsymbol{g}_t'|$ is larger than the tolerance, $\boldsymbol{g}_{t+1}$ is updated by the following equation.

$$\boldsymbol{g}_{t+1} = \begin{cases} \boldsymbol{g}_t + 2(\boldsymbol{g}_t' - \boldsymbol{g}_t) & (\text{ if } |\boldsymbol{g}_t' - \boldsymbol{g}_t| \geq 10\,\text{mm}\,) \\ \boldsymbol{g}_t + (\boldsymbol{g}_t' - \boldsymbol{g}_t) & (\text{ if } |\boldsymbol{g}_t' - \boldsymbol{g}_t| < 10\,\text{mm}\,) \end{cases} \tag{3.3}$$

Although there is no theoretical guarantee of convergence, it was experimentally confirmed that a location of the liver that was better than its initial location could be found through the several iterations, usually less than ten.

3.2.4 Patient-specific shape estimation

The next step is a patient-specific shape estimation, i.e., a fitting of the SSM to the rough segmentation result. In this study, I propose using the average *asymmetric* distance from the surface of the shape generated by the SSM Γ_M to that of the rough segmentation Γ_R for the sake of computational efficacy:

$$d(\Gamma_R, \Gamma_M) = \oint_{\Gamma_M} \min_{\mathbf{r}' \in \Gamma_R} \left\|\mathbf{r} - \mathbf{r}'\right\| d\Gamma \Bigg/ \oint_{\Gamma_M} d\Gamma \tag{3.4}$$

The Nelder-Mead search algorithm [46] is employed to minimize the coefficients **ff** for the SSM.

3.2.5 Fine segmentation based on graph cuts

In this study, graph cuts were employed, which is an efficient optimization method for the binary labeling problem using the s-t mincut algorithm [48]. Let $\mathcal{L}^{|\mathcal{V}|}$ denote a set of binary labels $\{0, 1\}$, where 0 and 1 correspond to the background and the foreground, respectively. The graph cuts optimize the binary labeling $\mathbf{x} = (x_1, \ldots, x_{|\mathcal{V}|}) \in \mathcal{L}^{|\mathcal{V}|}$ for a given image $\boldsymbol{I} = (I_1, \ldots, I_{|\mathcal{V}|}) \in \mathbb{R}^{|\mathcal{V}|}$ so that the following equation is minimized.

$$E(\mathbf{x}, \boldsymbol{I}) = \sum_{p \in \mathcal{V}} \lambda \cdot E_p^{\text{posterior}}(\mathbf{x}, \boldsymbol{I}) + \sum_{(p,q) \in \mathcal{E}} \left\{ E_{pq}^{\text{gradient}}(\boldsymbol{I}) + E_{pq}^{\text{shape}}(\boldsymbol{I}) \right\} \cdot \delta_{x_p \neq x_q} \tag{3.5}$$

where λ is the positive constant, and the function δ is defined as

$$\delta_{x_p \neq x_q} = \begin{cases} 1 & (x_p \neq x_q) \\ 0 & (x_p = x_q) \end{cases} \tag{3.6}$$

$E_p^{\text{posterior}}(\mathbf{x}, \boldsymbol{I})$ and $E_{pq}^{\text{gradient}}(x_p, x_q)$ are calculated as

$$E_p^{\text{posterior}}(\mathbf{x}, \boldsymbol{I}) = \begin{cases} \Pr(x_p = 0 | I_p) & (x_p = 1) \\ \Pr(x_p = 1 | I_p) & (x_p = 0) \end{cases} \tag{3.7}$$

$$E_{pq}^{\text{gradient}}(\boldsymbol{I}) = \exp\left\{ -\frac{(I_p - I_q)^2}{2\sigma^2} \right\} \cdot \frac{1}{\|\overrightarrow{pq}\|} \tag{3.8}$$

where σ is the positive constant. Shimizu et al. [47] proposed using the shape term, described as

$$E_{pq}^{\text{shape}}(\boldsymbol{I}) = \sqrt{\frac{1 - \cos\theta_{pq}}{2}} \tag{3.9}$$

where

$$\cos\theta_{pq} = \frac{\overrightarrow{pq} \cdot \nabla\phi^{\text{PSS}}(p)}{\|\overrightarrow{pq}\| \cdot \|\nabla\phi^{\text{PSS}}(p)\|}. \tag{3.10}$$

Let $\phi^{\text{PSS}}(p)$ denote the signed distance function of the estimated shape at voxel p. The gradient of the shape estimation $\nabla\phi^{\text{PSS}}(p)$ is shown in Figure 3.6.

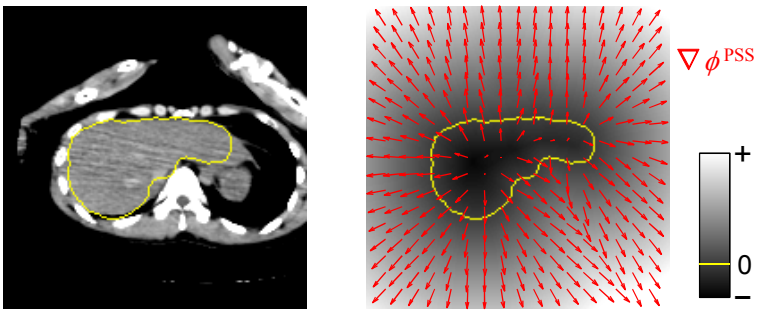

(a) Shape estimation (b) Gradient of the distance function

Fig. 3.6 (a) Estimated shape prior. (b) Gradient of the shape estimation

3.3 Experimental setups

In the experiment, 32 CT volumes acquired from 32 cadavers and the corresponding true liver label volumes were prepared. In training an SSM, half of the 32 dead liver labels were used together with artificial dead liver labels synthesized from 144 living liver labels. The remaining half of the 32 CT volumes of dead livers was used for validation of my segmentation algorithm. The process of training and validation was repeated after changing the role of the two datasets. It should be noted that the SSM construction and segmentation were performed in a reduced domain ($170 \times 170 \times 170$ voxels; 2.0 mm/voxel isotropic) because of memory limitations. The segmentation accuracy was measured by calculating the Jaccard index (JI) of the segmented region and true liver labels.

Five classes for GMM were used, i.e., liver, heart, right kidney, lesion, and other, the initial parameters of which were trained from 140 *in vivo* CT volumes. The parameters for graph cuts were determined empirically based on the JI of the segmentation result using the conventional model $D + T$ and fixed as $\sigma = 4.0$ and $\lambda = 0.1$ throughout the experiment.

3.4 Results and discussion

Figure 3.7 shows the JIs of a) the rough segmentation based on MAP, b) the shape estimation, and c) the graph cuts when using the eight different segmentation algorithms, each of which employs one of the eight SSMs. The results showed that the segmentation based on the $D + T$ model yielded the highest performance (average JI of 0.806). The $D + T$ model was the only model that significantly outperformed

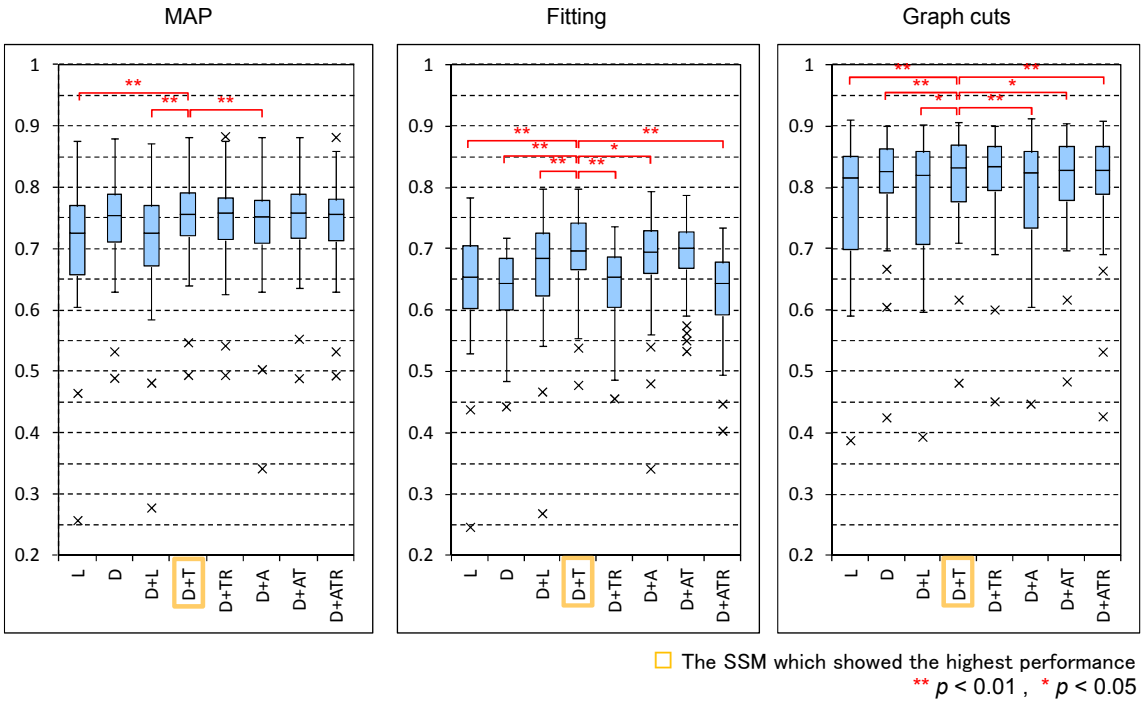

Fig. 3.7 JIs of a) the rough segmentation based on MAP, b) the shape estimation, and c) the graph cuts when using the eight different segmentation algorithms, each of which employs one of the eight SSMs

all of the conventional SSMs (the D, L, and $D + L$ models) in terms of both shape estimation and segmentation. Here, a Wilcoxon test with a significance level of 0.05 was used. It is worth mentioning that these findings are consistent with the results of the previous section, where the $D + T$ model proved the best model and superior to conventional SSMs, with statistical significance for a significance level of 0.05.

Figure 3.8 shows graph cut-based fine segmentation for four cases using different SSMs.

Figure 3.9 shows examples of shape estimation and graph cuts segmentation using L and $D + T$ model, in which the contours of the regions are shown in yellow. The figure shows that the shape estimated by the $D + T$ model was obviously more similar to the true boundary than that estimated by the L model, leading to higher accuracy in the graph cuts segmentation.

Figure 3.10 shows the transition of segmentation during the iteration of the proposed MAP segmentation algorithm using dynamic probabilistic atlas. The liver segmentation results improved with the increasing number of iterations.

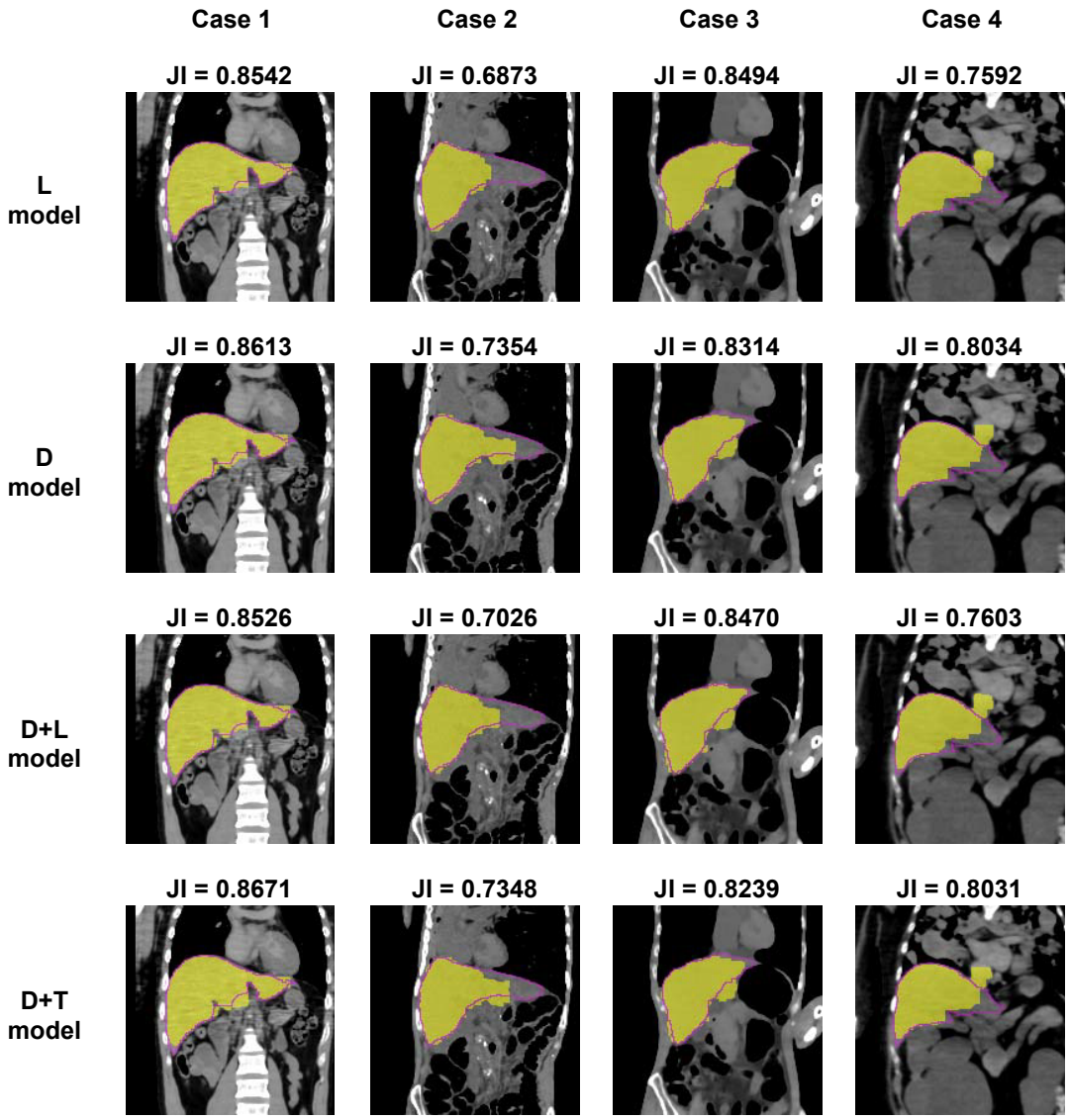

Fig. 3.8 Segmentation results for four cases using different SSMs

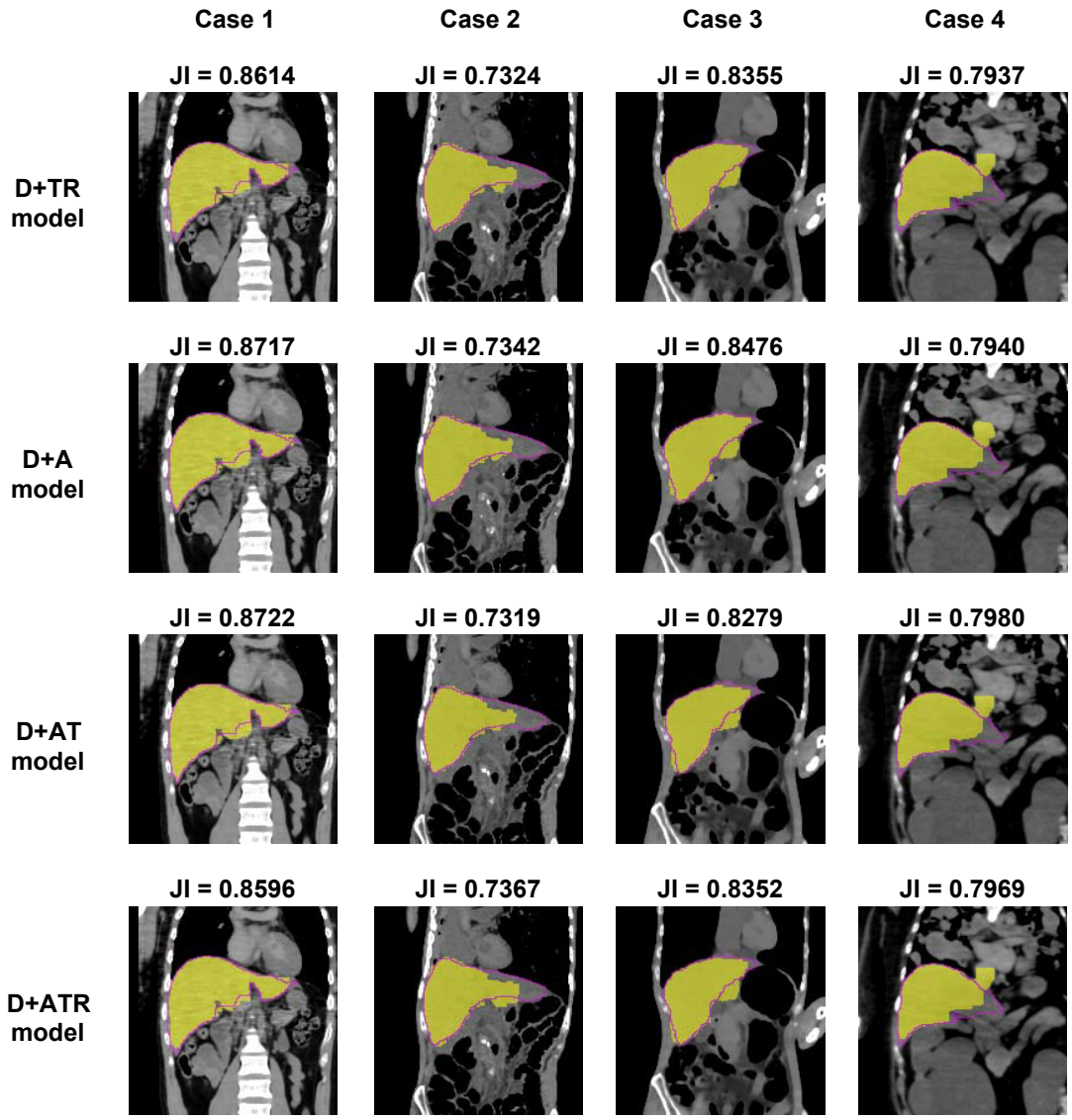

Fig. 3.8 Segmentation results for four cases using different SSMs (cont)

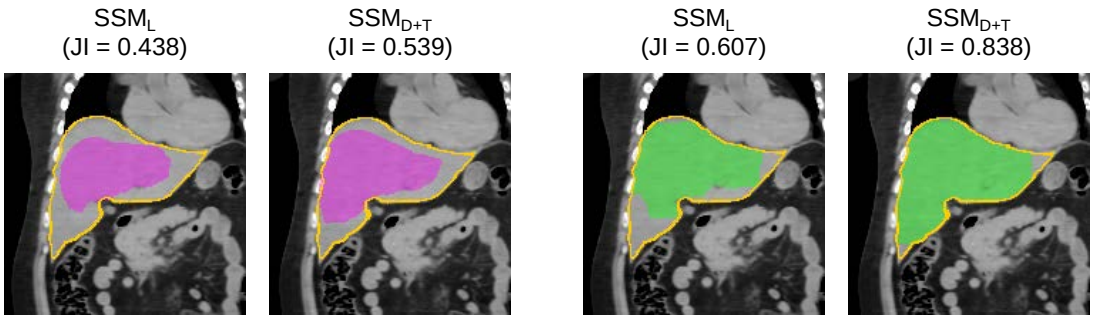

Fig. 3.9 Examples of (a) estimated shapes and (b) segmentation results from the conventional L model and the proposed $D + T$ model, which showed the best performance

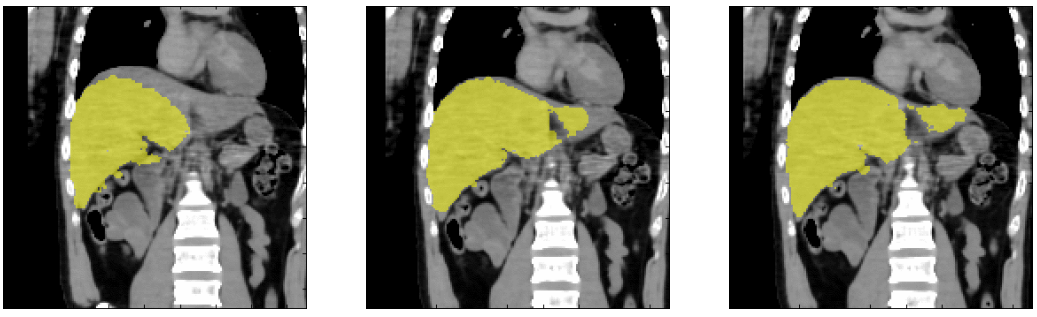

Fig. 3.10 Transition of segmentation during the iteration of the proposed MAP segmentation algorithm using dynamic probabilistic atlas

3.5 Conclusions

I proposed an SSM-based liver segmentation algorithm for autopsy imaging. A comparison study of algorithms was performed in a cross-validated manner with eight different SSMs and 32 dead liver CT volumes. The results showed the best segmentation algorithm employed the SSM trained from both dead liver labels and dead liver labels synthesized using a statistical transformation. The performance was statistically superior to that of algorithms with conventional SSMs constructed from dead and/or living liver labels. The current segmentation performance for a cadaver is inferior to that for a living body [1, 49, 50] because of postmortem deformation. I will improve the segmentation process in the near future by incorporating autopsy imaging specific knowledge into the process.

Chapter 4

Joint optimization of the segmentation and shape prior from an SSM

4.1 Introduction

SSM-based postmortem organ segmentation as shown in section 2 and 3 is an important topic; however, here I would like to address another interesting problem relates to the SSM-based segmentation for *in vivo* organs.

The automatic segmentation of abdominal organs such as the pancreas from a three-dimensional (3D) computed tomography (CT) volume is a challenging task because of the high inter-subject variability in the shape and location, as well as the existence of the surrounding organs, which appear similar to pancreatic tissue. A number of automated pancreas-segmentation algorithms have been proposed in the context of multi-organ [1, 51, 52] and single-organ [49, 53–57] segmentation frameworks, all of which yield low-accuracy segmentation.

A promising solution for improving the segmentation performance is the incorporation of a shape prior into a state-of-the-art segmentation algorithm, such as a graph cut [48]. A number of segmentation algorithms that incorporate shape priors have been proposed over the last decade, and they can be categorized into two different strategies. The first is the selection of one or more shape priors and performing shape-prior-based segmentation, and the second is optimizing the energy jointly for both the shape prior and the segmentation.

Most conventional studies based on graph cuts have employed the first strategy, and a variety of shape priors have been proposed. General shape constraints, such as ellipse [58], blob-like [59], or compact [60] priors, have been successfully applied

to the segmentation of a wide range of objects. While these shape priors are useful, they may be too simple for segmenting objects with more complex shapes. A user-defined shape template [61] was also incorporated into a graph-cut segmentation. In particular, a statistical shape model (SSM) [31] may be a good choice for a shape prior because it can describe the statistical variation in the shape of an organ, and an appropriate shape prior can be derived from the SSM. Several studies have proposed the incorporation of an SSM-based shape prior into the graph-cut segmentation process. Although Grosgeorge et al. [19] and Malcolm et al. [20] used shape priors for segmentation generated from SSMs produced through linear and nonlinear statistical analyses, respectively, their methods are not automated, and require user interaction. Nakagomi et al. [21] proposed fully automated segmentation using multiple shape priors, which were selected from eigenshapes generated through a uniform sampling of the first two eigenmodes of an SSM. Linguraru et al. [39] introduced a patient-specific shape prior, which was derived from the SSM computed using the Parzen window method. However, a common problem with these SSM-based approaches is that the shape prior and segmentation under the prior are not simultaneously optimized, but are sequentially optimized using different criteria. Therefore, the shape prior selected by these methods may not be optimal with respect to the graph-cut energy functional, which I hope to minimize during the segmentation process.

Of the graph-cut segmentation algorithms that use shape priors, a few have employed the second strategy to find the optimal energy jointly for the segmentation and shape prior. Kohli et al. [62] used a gradient descent method to optimize the graph-cut energy depending on the pose of the shape prior or a stickman model. The second strategy has also been employed in point-distribution model (PDM)-based approaches, such as the active shape model and active appearance model [4, 63]. However, in recent years, more sophisticated approaches have been employed. For example, Chen et al. [23] proposed a novel synergistic combination of the segmentation and PDM. This method iteratively updates the shape prior with the constraints of a PDM based on the current segmentation results. Although this study showed promising segmentation results, because it is based on an iterative optimization method, there is no mathematical guarantee that the attained shape prior will be globally optimal in terms of the objective functional. Besbes et al. [22] proposed a segmentation method based on random Markov fields, which combines shape priors that are defined using the PDM and regional statistics. The experimental results of hand segmentation showed the effectiveness of the shape prior. However,

in this study, only an approximate solution was obtained after the minimization of a nonconvex objective functional using a primal-dual algorithm. In addition, this method was only applied to two-dimensional (2D) image segmentation. Xiang et al. [24] proposed a novel framework for image segmentation through a unified-model-based and pixel-driven-integrated graphical model, where prior knowledge is expressed through the deformation of a discrete model that involves decomposing the shape of interest into a set of higher-order cliques. This method shares the same goal as my study on the joint minimization of the energy functional regarding the pixel-based segmentation and SSM-based shape prior. However, the energy functional described in this paper is rather difficult to optimize using a state-of-the-art optimization algorithm, or TRW-S, and is therefore trapped in the local minimum of the energy functional. Moreover, only the results for the small 2D images were shown, and it remains to be seen if this algorithm is applicable to large 3D medical images in terms of computational cost.

Lempitsky et al. [25] proposed a new framework for computing the optimal graph-cut segmentation, where a number of shape priors were defined as templates with various poses and locations. This framework is categorized as the first type of strategy because the shapes are selected in advance. A branch-and-bound search was conducted on a tree constructed from agglomerative bottom-up clustering using the predefined shape templates. The advantage of this study over the approaches mentioned above is that optimal segmentation can be obtained for a broad family of functionals depending on the given shape templates. However, this algorithm has a limitation in that the set of predefined templates may not include an optimal shape prior that truly minimizes the graph-cut energy among all possible shape priors generated by an SSM.

On the whole, all of the algorithms mentioned above suffer from the local minimum problem of their functional when considering all possible shapes generated from an SSM. Generally, a higher segmentation performance is expected if more shapes of an SSM are evaluated during the segmentation process. The goal of this study is to provide a theoretical framework for truly optimizing the segmentation energy considering all of the possible shapes generated from the SSM. This paper assumes that an SSM is represented as a subspace of level set functions learnt via principal component analysis (PCA), and the assumptions are relaxed in the discussion section. It is worth noting that to the best of my knowledge, this is the first study that perfectly solves the above local minimum problem. Because I employ a branch-and-bound search strategy, the proposed algorithm is similar to the

method proposed by Lempitsky et al. [25]. In contrast to Lempitsky et al. [25], my method employs the second strategy and finds a global solution, i.e., my method can incorporate all possible shapes defined by an SSM without sampling shapes from an eigenshape space of the SSM. In addition, I demonstrate the effectiveness of the proposed algorithm in the context of pancreas/spleen segmentation from CT volumes. The main contributions of this study, including the differences from existing works, are as follows:

- In contrast to the conventional method [25], my method conducts joint optimization in terms of the shape prior and segmentation labeling. In addition, it can handle many more 3D shape templates, and finds an optimal 3D shape prior[1] from among *all possible 3D shapes* (over 10^9) generated by an SSM. Owing to the combination of a level-set-based SSM and the fundamental theorem of linear programming, the algorithm has the following salient features.
  - A conventional algorithm conducts a branch-and-bound search over a tree of predefined shapes, whereas the proposed algorithm conducts a branch-and-bound search over the eigenshape space of an SSM to find an optimal shape prior from among all of the possible shapes generated by an SSM.
  - Unlike the conventional algorithm, the proposed algorithm does not require the clustering of predefined shape templates. In addition, it is not necessary to store an entire search tree with all clustered shapes during the segmentation process because the search tree is dynamically generated in a top-down manner during the optimization process. Note that it is nearly impossible to run the conventional algorithm with all of the possible 3D shapes (over 10^9) generated from an SSM, e.g., the clustering for 10^9 shapes takes over $10,000,000$ years and 2.04 PB of memory is required to store the entire clustering tree, as discussed in Section 4.4.2.
- I applied the proposed algorithm to pancreas and spleen segmentation using multiphase CT volumes, and I observed a statistically significant improvement compared to the algorithm proposed by Lempitsky et al. [25] for both the

[1] The term "optimal shape prior" is used differently in various studies. For example, an optimal shape prior in a study on multishape graph cuts by Nakagomi et al. [21] represented a shape prior generated by combining several shape templates using a fusion move with the quadratic pseudo-Boolean optimization (QPBO) algorithm. To the best of my knowledge, the present study is the first to find an optimal shape prior among *all of the possible shapes* generated by an SSM for single-shape graph cuts, and can be extended to multishape graph cuts in the near future.

Jaccard index (JI) and Dice similarity index (DSI). In addition, comparison with the state-of-the-art multiple abdominal organs segmentation algorithm was carried out so as to prove the effectiveness of the proposed algorithm.

The remainder of this chapter is organized as follows. Section 4.2 provides a brief introduction to a level set based SSM along with a description of how the SSM-based shape prior is incorporated into my segmentation algorithm. The experimental setup and results are presented in Section 4.3, followed by a discussion of the results in Section 4.4 and conclusions in Section 4.5.

4.2 Methods

4.2.1 Generation of shape priors using a level set distribution model

The shape priors used in the proposed method are generated from an SSM using level-set functions [17] or signed distance functions, which I refer to as the SSM level-set distribution model (LSDM), and the availability of different SSMs in my framework is discussed in Section 4.4.4. The shapes are embedded as a zero level set of signed distance functions with positive values inside an object and negative values outside the object, which are defined in a discrete 3D image domain comprising a voxel set $\mathcal{V}$. A training set of signed distance functions was statistically analyzed through a weighted principal components analysis [64], which yields an eigenshape space of dimension d ($\ll |\mathcal{V}|$). The following linear equation is widely used to generate a shape prior:

$$\phi^p(\boldsymbol{\alpha}) = \mu^p + \sum_{i=1}^{d} \alpha_i \sqrt{\lambda_i} u_i^p, \tag{4.1}$$

where μ^p denotes the average level-set functions of the training labels for the voxel p ($\in \mathcal{V}$), λ_i ($i = 1, \ldots, d$) is an eigenvalue, $\{u_1^p, \ldots, u_d^p\}$ represents the first d unit eigenmodes of the statistical variations for the voxel p, and the vector $\boldsymbol{\alpha} = [\alpha_1, \ldots, \alpha_d]^\top$ is a shape parameter vector, which is defined in the rectangular domain[2] $\mathcal{R}_{\boldsymbol{\alpha}} = \{r \in \mathbb{R}^d \mid \|r\|_\infty \leq w\}$ of an eigenshape space with a positive

[2] Note that an arbitrary convex polytopic domain is available for the shape parameter space without any modification of the proposed optimization process. In this study, I employed a rectangular domain for simplification of the implementation. In addition, the proposed method is applicable to a nonconvex polygon by developing preprocessing that divides a nonconvex polygon into a set of convex polygons, and postprocessing that finds the minimum from among a set of solutions for all divided convex polygons.

constant value w, which is typically set to 3. A shape prior in a discrete image domain is obtained by mapping $\boldsymbol{\alpha}$ to a label (see Fig. 4.1) as follows:

$$g : \boldsymbol{\alpha} \in \mathcal{R}_{\boldsymbol{\alpha}} \mapsto \mathbf{y} \in \mathcal{L}^{|\mathcal{V}|} \tag{4.2}$$

where $\mathcal{L} = \{0, 1\}$ is a set of labels, i.e., 0 for the background and 1 for the foreground. In this paper, I denote $\boldsymbol{g}(\boldsymbol{\alpha}) \in \mathcal{L}^{|\mathcal{V}|}$ and $\boldsymbol{\phi}(\boldsymbol{\alpha}) \in \mathbb{R}^{\mathcal{V}}$ as a vector (or image) whose p-th elements (or pixels) are $g_p(\boldsymbol{\alpha}) \in \mathcal{L}$, and $\phi^p(\boldsymbol{\alpha}) \in \mathbb{R}$, respectively. The LSDM uses a Heaviside function $\mathcal{H}(\cdot)$ as the mapping function $\boldsymbol{g}$.

$$y_p = g_p(\boldsymbol{\alpha}) = \mathcal{H}\left(\phi^p(\boldsymbol{\alpha})\right) = \begin{cases} 1 & (\phi^p(\boldsymbol{\alpha}) \geq 0) \\ 0 & (\phi^p(\boldsymbol{\alpha}) < 0) \end{cases} \tag{4.3}$$

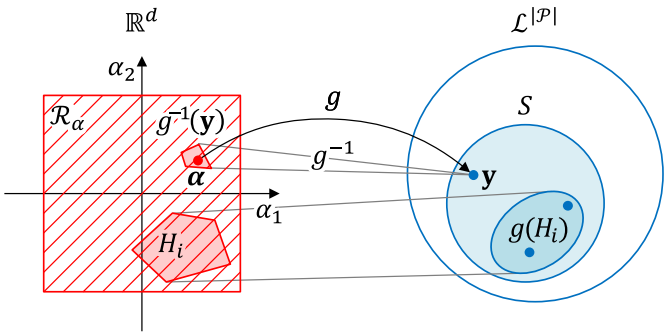

Fig. 4.1 Relationship between the eigenshape space of the LSDM and the discrete shape label domain. Function g is an onto-mapping from eigenshape space $\mathcal{R}_{\boldsymbol{\alpha}}$ to the discrete shape label domain $\mathcal{L}^{|\mathcal{V}|}$. The set of shape priors $\mathcal{S} \subset \mathcal{L}^{|\mathcal{V}|}$ is defined as an image of g, i.e., $\mathcal{S} = g(\mathcal{R}_{\boldsymbol{\alpha}})$. An arbitrary convex polygon in eigenshape space H_i corresponds to the set of shape labels $g(H_i)$. Each label $\mathbf{y} \in \mathcal{S}$ has a pre-image $g^{-1}(\mathbf{y}) \in \mathcal{R}_{\boldsymbol{\alpha}}$

Note that the image of g is the set $\mathcal{S}$ $(\in \mathcal{V})$, which comprises a finite but significantly large number of shape priors, which is difficult to handle using a conventional algorithm [25]. My goal is finding an optimal shape prior from set $\mathcal{S}$ in terms of a graph cut energy functional. The important properties of function g, which is a Heaviside function in the present study, are summarized as follows. The function is 1) monotonic and 2) has a many-to-one mapping, i.e., the inverse image $g^{-1}(\mathbf{y})$ is

$$g^{-1}(\mathbf{y}) = \left\{\boldsymbol{\alpha} \in \mathcal{R}_{\boldsymbol{\alpha}} \middle| \phi^p(\boldsymbol{\alpha}) \geq 0 \text{ for } \forall p \in \mathcal{F}\right\} \cap \left\{\boldsymbol{\alpha} \in \mathcal{R}_{\boldsymbol{\alpha}} \middle| \phi^p(\boldsymbol{\alpha}) < 0 \text{ for } \forall p \in \mathcal{B}\right\} \tag{4.4}$$

where $\mathcal{F} = \{p \in \mathcal{V} \mid y_p = 1\}$ and $\mathcal{B} = \{p \in \mathcal{V} \mid y_p = 0\}$ are the sets of voxels assigned to a the foreground and background, respectively. The third property of function g is that the inverse image $g^{-1}(\mathbf{y})$ is a solution of the simultaneous linear inequalities of size $|\mathcal{V}|$, which is a convex polygon in a two-dimensional (2D) eigenshape space. Note that most of the explanations provided in the present study utilize a 2D eigenshape space for simplicity, which can easily be extended to higher dimensions, *e.g.* , a convex polygon can be replaced with a convex polyhedron in a 3D eigenshape space. The segmentation of target CT volume $\boldsymbol{I} \in \mathcal{L}^{|\mathcal{V}|}$ is defined as 0-1 labeling $\mathbf{x} = (x_1, \ldots, x_{|\mathcal{V}|}) \in \mathcal{L}^{|\mathcal{V}|}$. A shape prior $\mathbf{y} \in \mathcal{S}$ is incorporated into the segmentation, where $\mathcal{S} \subset \mathcal{L}^{|\mathcal{V}|}$ is a set of shape priors. The goal of the present study is the simultaneous optimization of the segmentation energy functional in terms of the labeling $\mathbf{x} \in \mathcal{L}^{|\mathcal{V}|}$ and shape priors $y \in \mathcal{S}$, which leads to the following minimization problem:

$$\min_{\mathbf{x}\in\mathcal{L}^{|\mathcal{V}|},\, \mathbf{y}\in\mathcal{S}} E(\mathbf{x}, \mathbf{y}, \boldsymbol{I}) = \min_{\mathbf{x}\in\mathcal{L}^{|\mathcal{V}|},\, \mathbf{y}\in\mathcal{S}} \left\{ \sum_{p\in\mathcal{V}} F^p(\boldsymbol{I}, \mathbf{y}) \cdot x_p + \sum_{p\in\mathcal{V}} B^p(\boldsymbol{I}, \mathbf{y}) \cdot (1 - x_p) + \sum_{(p,q)\in\mathcal{E}} P^{pq}(\boldsymbol{I}) \cdot \left| x_p - x_q \right| \right\}, \quad (4.5)$$

where N is the set of neighboring voxel pairs. The unary potential terms $F^p(\boldsymbol{I}, \mathbf{y})$ and $B^p(\boldsymbol{I}, \mathbf{y})$ which are the costs when assigning voxel p to the foreground and background, respectively, are defined as follows:

$$F^p(\boldsymbol{I}, \mathbf{y}) = \lambda_1 \cdot \Pr\left(x_p = 0 \mid I_p\right) + \lambda_2 \cdot (1 - y_p) \quad (4.6)$$

$$B^p(\boldsymbol{I}, \mathbf{y}) = \lambda_1 \cdot \Pr\left(x_p = 1 \mid I_p\right) + \lambda_2 \cdot y_p \quad (4.7)$$

I use a similar energy functional to that proposed by Lempitsky et al. [25], but it differs with respect to the definition of shape prior $\mathbf{y}$, as described above. The other changes compared with the method of Lempitsky et al. [25] are related to the functional $\Pr\left(x_p = 0 \mid I_p\right)$,

$$\Pr\left(x_p \mid I_p\right) = \frac{\Pr\left(I_p \mid x_p\right) \Pr\left(x_p\right)}{\Pr\left(I_p\right)}, \quad (4.8)$$

which is the posterior probability of a background or foreground that is linearly combined with a shape prior term using positive constants λ_1 and λ_2 to represent

the appearance, which has an important role in the segmentation of an organ [49]. The term $P^{pq}(\boldsymbol{I})$ is a pairwise potential that defines the cost of assigning adjacent pixels $(p, q) \in \mathcal{E}$ to different labels.

$$P^{pq}(\boldsymbol{I}) = \exp\left\{-\frac{(I_p - I_q)^2}{2\sigma^2}\right\} \cdot \frac{1}{\|\overrightarrow{pq}\|} \tag{4.9}$$

4.2.2 Energy minimization strategy

The significantly large number of shape priors in $\mathcal{S}$ ($\subset \mathcal{L}^{|\mathcal{V}|}$) makes it difficult to conduct the global minimization of Eq. (4.5) in terms of $\mathbf{x} \in \mathcal{L}^{|\mathcal{V}|}$ and $\mathbf{y} \in \mathcal{S}$ using a conventional approach [25]. Although my approach employs a branch-and-bound search strategy, I utilize a dynamic branching operation and bounding computation in an eigenshape space. The key concept that underlies the proposed algorithm is that the division of a set of shape priors used for branching can be replaced with a partition of an eigenshape space, which yields convex polygons that correspond to the shape priors. Another important feature of my method is a bounding computation algorithm for a given arbitrary convex polygon in an eigenshape space, which I describe later. Consequently, the search algorithm used to find an optimal shape prior can be replaced with a top-down search algorithm for an optimal convex polygon in an eigenshape space, where only a portion of a tree is generated and searched during the process. These two important features facilitate an efficient branch-and-bound search in $\mathcal{S}$ ($\subset \mathcal{L}^{|\mathcal{V}|}$). The proposed optimization procedure is conducted in an eigenshape space, and thus I rewrote the energy minimization problem by substituting mapping function $g(\boldsymbol{\alpha})$ for shape prior $\mathbf{y}$.

$$\min_{\boldsymbol{\alpha} \in \mathcal{R}_{\boldsymbol{\alpha}}} \min_{\mathbf{x} \in \mathcal{L}^{|\mathcal{V}|}} E(\mathbf{x}, g(\boldsymbol{\alpha}); \boldsymbol{I}) \tag{4.10}$$

The best-first branch-and-bound algorithm [65] is used for the global optimization of Eq. (4.10). First, I describe the branching operation when given a parent node that corresponds to a convex polygon in $\mathcal{R}_{\boldsymbol{\alpha}}$, which is followed by an explanation of the bounding computation and the pseudo-code of the proposed algorithm.

Branching

Given parent node H_0 ($\subseteq \mathcal{R}_{\boldsymbol{\alpha}}$), branching is a step used to partition node H_0 into child nodes H_1 and H_2, ($H_1 \cup H_2 = H_0, H_1 \cap H_2 = \emptyset$), which decomposes Eq. (4.10)

into two sub-problems.

$$\min_{\boldsymbol{\alpha}\in H_0}\min_{\mathbf{x}\in\mathcal{L}^{|\mathcal{V}|}} E(\mathbf{x}, g(\boldsymbol{\alpha}); \boldsymbol{I}) = \min_{i\in\{1,2\}}\left\{\min_{\boldsymbol{\alpha}\in H_i}\min_{\mathbf{x}\in\mathcal{L}^{|\mathcal{V}|}} E(\mathbf{x}, g(\boldsymbol{\alpha}); \boldsymbol{I})\right\} \tag{4.11}$$

Various partitions are possible, but I propose a division based on the sign of $\phi^k(\boldsymbol{\alpha})$ in Eq. (4.1) at voxel k sampled from set Q:

$$H_1 = \left\{ \boldsymbol{\alpha} \in H_0 \;\middle|\; \phi^k(\boldsymbol{\alpha}) \geq 0 \right\}, \tag{4.12}$$

$$H_2 = \left\{ \boldsymbol{\alpha} \in H_0 \;\middle|\; \phi^k(\boldsymbol{\alpha}) < 0 \right\} \tag{4.13}$$

In this case, Q is a set of voxels k such that the hyperplane $\phi^k(\boldsymbol{\alpha}) = 0$ intersects H_0:

$$Q = \left\{ k \in \mathcal{V} \;\middle|\; \min_{\boldsymbol{v}\in V_0} \phi^k(\boldsymbol{v}) < 0 < \max_{\boldsymbol{v}\in V_0} \phi^k(\boldsymbol{v}) \right\} \tag{4.14}$$

where V_0 is a set of vertices for a convex polygon H_0, which can be computed analytically by solving the simultaneous linear equations for values of $\phi^e(\boldsymbol{\alpha})$ that correspond to the edges of H_0. Figure 4.2(a) illustrates the relationship between convex polygon H_i and the sign of level set functions $\phi^a(\boldsymbol{\alpha})$, $\phi^b(\boldsymbol{\alpha})$, and $\phi^c(\boldsymbol{\alpha})$ at different voxels a, b, and c of Fig. 4.2 (b), among which only voxel c is a member of Q (i.e., $c \in Q$ and $a, b \notin Q$). The entire set of Q comprises the voxels in the gray region shown in Fig. 4.2 (b), where the value of $\mathcal{H}(\phi^p(\boldsymbol{\alpha}))$ is either 1 or 0 over $\boldsymbol{\alpha} \in H_i$.

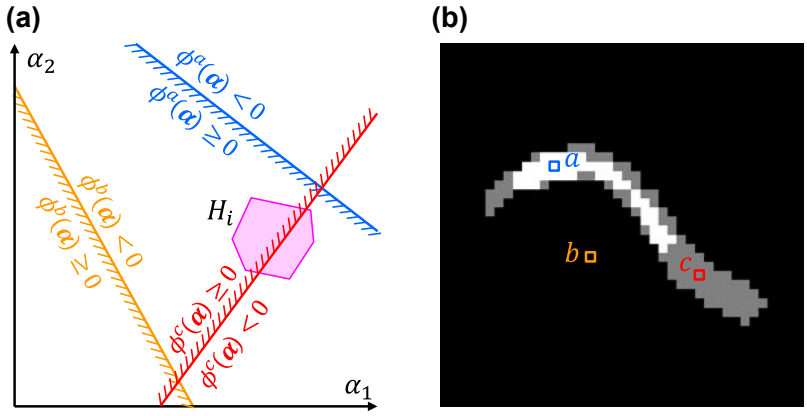

Fig. 4.2 The relationship between the location of voxel p and the sign of $\phi^p(\boldsymbol{\alpha})$ in the given H_i. The three lines in (a) correspond to $\phi^p(\boldsymbol{\alpha}) = 0$ for the three voxels in figure (b). Here, the normal vector of each hyperplane $\phi^p(\boldsymbol{\alpha}) = 0$ in (a) is $\left[\sqrt{\lambda_1}u_1^p, \ldots, \sqrt{\lambda_d}u_d^p\right]$ $(p \in \mathcal{V})$. The different colors in (b) correspond to three classes. $\mathcal{H}\left(\phi^p(\boldsymbol{\alpha})\right)$ always takes a value of 1 in the white region and 0 in the black region for $\forall \boldsymbol{\alpha} \in H_i$. Set Q comprises the voxels in the gray region, where the value of $\mathcal{H}\left(\phi^p(\boldsymbol{\alpha})\right)$ is either 1 or 0 over $\boldsymbol{\alpha} \in H_i$

Bounding

The lower bounds $L(H_i; \boldsymbol{I})$ $(i \in \{1, 2\})$ of my method are given below.

$$\min_{\boldsymbol{\alpha} \in \mathcal{R}_{\boldsymbol{\alpha}}} \min_{\mathbf{x} \in \mathcal{L}^{|\mathcal{V}|}} E(\mathbf{x}, g(\boldsymbol{\alpha}); \boldsymbol{I})$$

$$\geq \min_{\mathbf{x} \in \mathcal{L}^{|\mathcal{V}|}} \left\{ \sum_{p \in \mathcal{V}} \min_{\boldsymbol{\alpha} \in H_i} F^p(\boldsymbol{I}, \boldsymbol{g}(\boldsymbol{\alpha})) \cdot x_p + \sum_{p \in \mathcal{V}} \min_{\boldsymbol{\alpha} \in H_i} B^p(\boldsymbol{I}, \boldsymbol{g}(\boldsymbol{\alpha})) \cdot (1 - x_p) \right.$$
$$\left. + \sum_{(p,q) \in \mathcal{E}} P^{pq}(\boldsymbol{I}) \cdot |x_p - x_q| \right\} \quad (4.15)$$

$$= \min_{\mathbf{x} \in \mathcal{L}^{|\mathcal{V}|}} \left\{ \sum_{p \in \mathcal{V}} F^p(\boldsymbol{I}, \boldsymbol{g}^{\max}(H_i)) \cdot x_p + \sum_{p \in \mathcal{V}} B^p(\boldsymbol{I}, \boldsymbol{g}^{\min}(H_i)) \cdot (1 - x_p) \right.$$
$$\left. + \sum_{(p,q) \in \mathcal{E}} P^{pq}(\boldsymbol{I}) \cdot |x_p - x_q| \right\} \quad (4.16)$$

$$:= L(H_i; \boldsymbol{I}) \quad (4.17)$$

Here, I denote $\boldsymbol{g}^{\max}(H_i) \in \mathcal{L}^{|\mathcal{V}|}$ and $\boldsymbol{g}^{\min}(H_i) \in \mathcal{L}^{|\mathcal{V}|}$ as the maximum and minimum of $\boldsymbol{g}(\boldsymbol{\alpha})$ over $\boldsymbol{\alpha} \in H_i$ at each voxel, i.e., whose p-th elements are $g_p^{\max}(H_i) = \max_{\boldsymbol{\alpha} \in H_i} g_p(\boldsymbol{\alpha})$ and $g_p^{\min}(H_i) = \min_{\boldsymbol{\alpha} \in H_i} g_p(\boldsymbol{\alpha})$, respectively. The inequality in Eq. (4.15) is Jensen's inequality for the minimum operation. Eq. (4.16) is derived from the fact that $F^p(\boldsymbol{I}, \boldsymbol{g}(\boldsymbol{\alpha}))$ and $B^p(\boldsymbol{I}, \boldsymbol{g}(\boldsymbol{\alpha}))$ are the monotonically decreasing and increasing functions, respectively, in terms of y_p (see Eqs. (4.6) and (4.7)), and are independent of y_q ($q \in \mathcal{V} \setminus p$). Here, H_i is a convex polygon, $g_p(\boldsymbol{\alpha})$ ($p \in \mathcal{V}$) is a monotonic function (see the properties of $g_p(\boldsymbol{\alpha})$ in Section 4.2.1), and $\phi^p(\boldsymbol{\alpha})$ is a linear function (see Eq. (4.1)); thus, the maximum and minimum of $\phi^p(\boldsymbol{\alpha})$ for $\boldsymbol{\alpha} \in H_i$ can be found in the set V_i of H_i, and are based on the fundamental theorem of linear programming [66], which yields the following equations:

$$g_p^{\max}(H_i) = \begin{cases} 0 & \text{if } \phi^p(\boldsymbol{\alpha}) < 0 \text{ for } \forall \boldsymbol{v} \in V_i \\ 1 & \text{otherwise} \end{cases} \tag{4.18}$$

$$g_p^{\min}(H_i) = \begin{cases} 1 & \text{if } \phi^p(\boldsymbol{\alpha}) \geq 0 \text{ for } \forall \boldsymbol{v} \in V_i \\ 0 & \text{otherwise} \end{cases} \tag{4.19}$$

Once the maximum and minimum values of $\mathcal{H}\left(\phi^p(\boldsymbol{\alpha})\right)$ for $\boldsymbol{\alpha} \in H_i$ are obtained from Eqs. (4.18) and (4.19), the minimum value for $\mathbf{x} \in \mathcal{L}^{|\mathcal{V}|}$ in Eq. (4.16), or $L(H_i; \boldsymbol{I})$, can be computed efficiently using the s-t mincut algorithm [48]. Note that the three properties required for global optimization, i.e., monotonicity, computability, and the tightness of the lower bound $L(H_i; \boldsymbol{I})$, are satisfied by this method. The proof is given in **Appendix B**. Figure 4.2 shows the relationships between the location of voxel p and the sign of $\phi^p(\boldsymbol{\alpha})$ over $\boldsymbol{\alpha} \in H_i$ These relationships are categorized into the following three classes according to the sign of $\phi^p(\boldsymbol{\alpha})$.

(i) $\phi^p(\boldsymbol{\alpha}) \geq 0 \quad \forall \boldsymbol{\alpha} \in H_i \quad \leftrightarrow \min_{\boldsymbol{\alpha} \in H_i} \mathcal{H}\left(\phi^p(\boldsymbol{\alpha})\right) = \min_{\boldsymbol{\alpha} \in H_i} \mathcal{H}\left(\phi^p(\boldsymbol{\alpha})\right) = 1$

(ii) $\phi^p(\boldsymbol{\alpha}) < 0 \quad \forall \boldsymbol{\alpha} \in H_i \quad \leftrightarrow \min_{\boldsymbol{\alpha} \in H_i} \mathcal{H}\left(\phi^p(\boldsymbol{\alpha})\right) = \min_{\boldsymbol{\alpha} \in H_i} \mathcal{H}\left(\phi^p(\boldsymbol{\alpha})\right) = 0$

(iii) Otherwise $\quad \leftrightarrow \min_{\boldsymbol{\alpha} \in H_i} \mathcal{H}\left(\phi^p(\boldsymbol{\alpha})\right) = 1, \ \min_{\boldsymbol{\alpha} \in H_i} \mathcal{H}\left(\phi^p(\boldsymbol{\alpha})\right) = 0$

The three lines in Fig. 4.2(a) correspond to $\phi^p(\boldsymbol{\alpha})$ at voxels a, b, and c in Fig. 4.2(b), where the gray values represent three classes in the actual nodes in the binary tree during pancreas segmentation (see Section 4.3.1). Voxel a belongs to class (i), voxel b is a member of class (ii), and voxel c belongs to class (iii). Note that the set Q in Eq. (4.14) comprises voxels from class (iii).

4.2.3 Implementation

Algorithm 3 shows the pseudo-code of the proposed optimization algorithm. Given target image $\boldsymbol{I}$, an initial convex polygon H_0 that corresponds to the root node is set as $\mathcal{R}_{\boldsymbol{\alpha}}$. Next, H_0 is divided into two sub-regions, H_1 and H_2, through Eqs. (4.12) and (4.13) using voxel k selected from Q by the operation $Select(Q)$. The child nodes, H_1 and H_2, are inserted into *Queue* as candidates for the next parent node through an *InsertWithPriority* operation. *Queue* is a priority queue, where each element H_i is stored in ascending order of the associated lower bounds, $L(H_i; \boldsymbol{I})$. Next, H_0 is replaced with the node of the lowest lower bound, which is drawn from the queue using a *PullHighestPriorityElement* operation, which is followed by updating set Q. When $Q = \emptyset$, any $\boldsymbol{\alpha}^* \in H_0$ yields a globally optimal shape prior $\mathbf{y}^* = g(\boldsymbol{\alpha}^*)$. Finally, the optimal segmentation $\mathbf{x}^*$ is obtained by finding $\arg\min_{\mathbf{x} \in \mathcal{L}^{|\mathcal{V}|}} E(\mathbf{x}, \mathbf{y}; \boldsymbol{I})$ using the s-t mincut algorithm [18].

Algorithm 3 Pseudo-code of the proposed optimization algorithm

Require: Target image $\boldsymbol{I}$
  $H_0 \leftarrow \mathcal{R}_{\boldsymbol{\alpha}}$
  $Q \leftarrow \left\{ k \in \mathcal{V} \;\middle|\; \min_{\boldsymbol{v} \in V_0} \phi^k(\boldsymbol{v}) < 0 < \max_{\boldsymbol{v} \in V_0} \phi^k(\boldsymbol{v}) \right\}$
  $Queue \leftarrow \emptyset$
  $Queue.InsertWithPriority(H_0, L(H_0; \boldsymbol{I}))$
  while $Q \neq \emptyset$ **do**
    $k \leftarrow Select(Q)$
    $H_1 \leftarrow \left\{ \boldsymbol{\alpha} \in H_0 \;\middle|\; \phi^k(\boldsymbol{\alpha}) \geq 0 \right\}$
    $H_2 \leftarrow \left\{ \boldsymbol{\alpha} \in H_0 \;\middle|\; \phi^k(\boldsymbol{\alpha}) < 0 \right\}$
    $Queue.InsertWithPriority(H_1, L(H_0; \boldsymbol{I}))$
    $Queue.InsertWithPriority(H_2, L(H_0; \boldsymbol{I}))$
    $H_0 \leftarrow Queue.PullHighestPriorityElement()$
    $Q \leftarrow \left\{ k \in \mathcal{V} \;\middle|\; \min_{\boldsymbol{v} \in V_0} \phi^k(\boldsymbol{v}) < 0 < \max_{\boldsymbol{v} \in V_0} \phi^k(\boldsymbol{v}) \right\}$
  end while
  $\mathbf{y}^* \leftarrow g(\boldsymbol{\alpha}^*)$ where $\boldsymbol{\alpha}^* \in H_0$
  $\mathbf{x}^* \leftarrow \arg\min_{\mathbf{x} \in \mathcal{L}^{|\mathcal{V}|}} E(\mathbf{x}, \mathbf{y}^*; \boldsymbol{I})$

Two computations of s-t mincut are executed at each node in parallel in a multi-threaded environment. To further accelerate the s-t mincut algorithm, I exploit the fact that the solutions of the s-t mincut problem at different nodes are sufficiently similar to use the dynamic graph cut [67] technique, where the previous max-flow computation is used to find the solution in the updated residual graph.

The $Select(Q)$ operation may be a random selection from set Q because the global solution of the segmentation is independent of the choice of $Select(Q)$. Assuming that any shape prior is equally likely to be optimal, the binary search tree is preferably balanced [68], i.e., each child of any node contains almost the same number of shapes as its sibling. Thus, I propose the use of the following selection operation to maintain the balance of the search tree, instead of a random selection:

$$Select(Q) = \arg\min_{p \in Q} \frac{|a-b|}{|a+b|} \tag{4.20}$$

where $a = \max_{\boldsymbol{v} \in V_0} \phi^p(\boldsymbol{v})$ and $b = -\min_{\boldsymbol{v} \in V_0} \phi^p(\boldsymbol{v})$, the values of which are proportional to the maximum and minimum of the signed distance between the hypersurface $\phi^p(\boldsymbol{\alpha}) = 0$ and the vertices V_0, respectively. Note that $|a-b|/|a+b|$ in Eq. (4.20) takes a higher value as a/b becomes more distant from 1. Intuitively, Eq. (4.20) approximates voxel p, which divides H_0 into two equally sized regions, H_1 and H_2.

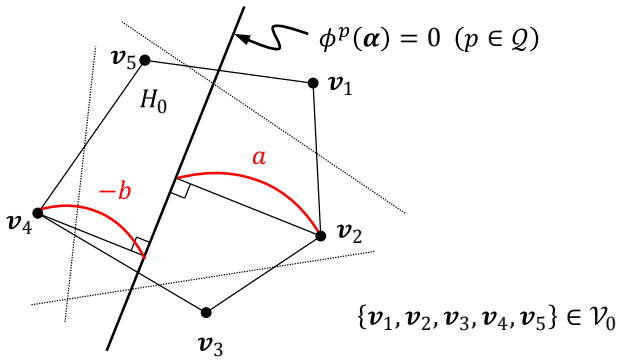

Fig. 4.3 Illustration of the process used to find a voxel for partitioning. The maximum and minimum of the signed distance from the hypersurface $\phi^p(\boldsymbol{\alpha}) = 0$ to the vertices V_0 are computed to select a voxel for partitioning. The proposed operator finds a voxel $p \in Q$ that minimizes $|a-b|/|a+b|$

4.3 Experimental setup and results

I validated the proposed algorithm in the context of the automated segmentation of the pancreas and spleen. Note that the energy functional used and the target organs are just examples to show the applicability of my framework to an actual segmentation problem. I verified that the energy of my method is lower than that of

the method proposed by Lempitsky *et al.*, which contributes to an improvement in the segmentation accuracy. I also conducted a comparison experiment with one of the state-of-the-art multi-organ segmentation algorithms proposed by Okada et al. [52] for both pancreas and spleen segmentation.

4.3.1 Pancreas segmentation

I validated the proposed algorithm in the context of automated pancreas segmentation using contrast-enhanced multiphase 3D CT volumes, or early-, portal-, and late-phase volumes that were obtained from 140 patients, which I refer to as Dataset-A in this study. The CT volumes in Dataset-A was measured as $512 \times 512 \times (154–901)$ voxels with a spacing of $(0.546–0.782) \times (0.546–0.782) \times (0.5–1.0)$ mm/voxel.

To make use of the three-phase information, I aligned the portal- and late-phase volumes (floating volumes) to the early-phase volume (target volume). For each control point placed on the regular lattice grids in the floating volume with an interval of 30 voxels, I calculated a displacement vector using template matching with a cube of 31 voxels on each side. I employed the normalized mutual information (NMI) for the metric of similarity between different phase volumes. I calculated the optimal displacement using an exhaustive search in a cuboidal region of $11 \times 11 \times 21$ voxels centered at the control point. After template matching, I established the correspondence of every voxel $\mathbf{r}_t \in \mathbb{Z}^3$ in the target volume with that in the floating volume $\mathbf{r}_f \in \mathbb{R}^3$ using a radial basis function (RBF):

$$\mathbf{r}_f = A\mathbf{r}_t + R + WG \tag{4.21}$$

where G is a radial basis function matrix, the matrix A is an affine matrix, T is a translation vector, and W is a weight matrix, all of which are computed by solving linear simultaneous equations [69]. I calculated the CT value of the voxel $\mathbf{r}_t \in \mathbb{R}^3$ in a floating volume using trilinear interpolation.

Next, I automatically extracted an abdominal cavity using graph cuts, and I used it to obtain a rough alignment of the CT volumes of an unknown input subject to those of a reference subject whose number of slices is the maximum among the training data. After the rough alignment, I extracted the surrounding organs, or the liver and spleen using the maximum a posteriori probability (MAP) method followed by a refinement process based on morphological operations and graph cuts. Subsequently, I extracted the portal, splenic, and superior mesenteric veins from a portal-phase CT volume using a region-growing algorithm whose seed points

were determined using the estimated hilum locations of the liver and spleen. Finally, I conducted a spatial standardization of the pancreas to eliminate pose variances between subjects. To do this, I used a method similar to that applied by Shimizu et al. [49], where I carried out an RBF-based nonlinear registration to the reference volume using 56 landmarks (see Fig. 4.4), i.e., 40 landmarks in the abdominal cavity, 14 landmarks in the portal and the splenic and superior mesenteric veins, and two landmarks in the extracted liver and spleen. I also learned an SSM of the pancreas from the spatially standardized training labels that were aligned using the same deformation field.

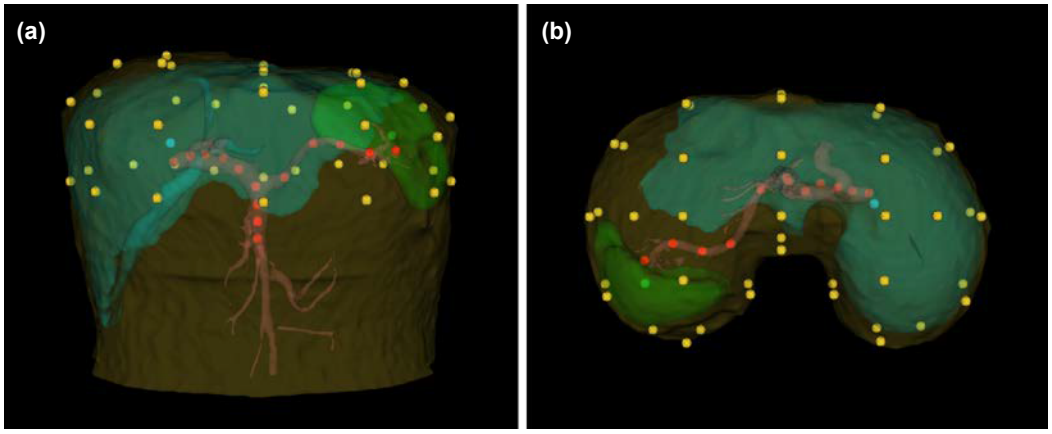

Fig. 4.4 Examples of (a) the front and (b) top views of the 56 extracted landmarks used for spatial registration of the pancreas. Forty landmarks are in the abdominal cavity (yellow); 14 landmarks are in the portal, splenic, and superior mesenteric veins (*red*); and the remaining two landmarks are in the extracted liver (*blue*) and spleen (*green*)

After the spatial standardization, I conducted three different types of segmentation using the proposed algorithm, the algorithm proposed by Lempitsky *et al.* and without using the shape-prior based energy. I computed the likelihood, $\Pr\left(I_p \mid x_p\right)$, of Eq. (4.21) from the Gaussian mixture distribution of the organs that were estimated using the expectation-maximization (EM) algorithm, where I assumed a Gaussian distribution of two classes, i.e., the pancreas and other tissues, and I computed the initial values of the statistical parameters used in the EM algorithm, i.e., the average values and the variances of the foreground/background features, from the training data.

In order to account for the much greater shape variation, I set the number of eigenmodes of the level-set-based SSM and the size of $\mathcal{R}_{\boldsymbol{\alpha}}$ to $d = 2$ and $w = 3.0$, respectively, the former being the same value used by Nakagomi et al. [21], and the latter being a higher value [21]. The RBF-based three-phase registration employed a Gaussian kernel whose standard deviation was 22.5 mm, and the RBF-based spatial standardization of the pancreas used a biharmonic kernel. I employed a 26-neighborhood system for the graph cuts. The parameters used for the graph cuts were determined experimentally, and were fixed to $(\lambda_1, \lambda_2, \sigma) = (1.05, 0.55, 10.0)$ throughout the pancreas-segmentation experiment.

I compared the results with those obtained using a conventional algorithm or the method proposed by Lempitsky *et al.* which uses a set of predefined shape templates. Fair comparison studies could be designed with different consistency conditions between segmentation algorithms, as follows:

1. Consistency in the segmentation performance (or the number of shapes considered)
2. Consistency in the memory requirements
3. Consistency in the computational time
4. Consistency in the number of nodes traversed (or searched)

Because it is difficult to simultaneously impose several consistency conditions, in this study, I employed each condition in 1 and 2. To perform a comparison study under the performance consistency condition, I first planned the experiment using all of the shapes $\mathcal{S}$ generated from an SSM, where $|\mathcal{S}| > 10^9$. The proposed algorithm requires 1.07 GB of memory and takes an average time of 213 s to find the globally optimal solution from $\mathcal{S}$. In contrast, because of the high computational cost of the algorithm proposed by Lempitsky *et al.* I estimated the required memory and computational time. I found that the estimated memory size is 2.04 PB, and the estimated computational time is over 10^7 years using the same computer (see Section 4.4.2 for the details). The superiority of my algorithm is therefore obvious. Subsequently, to obtain a quantitative comparison, I performed an experiment under the memory consistency condition using a smaller subset of shapes $\mathcal{S}' \subset \mathcal{S}$. I set the number of shapes as $\mathcal{S}' = 49$, which were generated by performing uniform sampling from the same eigenshape space $\mathcal{R}_{\boldsymbol{\alpha}}$ with intervals of 1.0. Under this setting, the experimental results indicated that the method proposed by Lempitsky *et al.* required 1.16 GB on average for $\mathbf{y} \in \mathcal{S}'$, while my algorithm requires 1.07 GB

on average for $\mathbf{y} \in \mathcal{S}$, which are nearly the same. The agglomerative hierarchical clustering over $\mathcal{S}'$ for their method was conducted using the Hamming distance measure, which was the same as that proposed by Lempitsky et al. [25].

To improve the computational efficiency, the input volumes were reduced to 256 $\times$ 256 $\times$ (335–340) isotropic voxels of (1.092–1.24) mm/voxel before executing the registration, segmentation of the neighboring organs, and spatial standardization. For the proposed pancreas segmentation method, to further reduce the computational costs, I clipped the CT volume with an automatically defined rectangular region based on the MAP estimates of the neighboring organs. The size of the rectangular region was 193 $\times$ 146 $\times$ 145 voxels, which was sufficiently large to cover the pancreas for all of the patients. The SSM was also constructed within a rectangular region.

I conducted a two-fold cross-validation study on Dataset-A with 140 patients, and I evaluated the segmentation accuracy based on the JI for an extracted region and the true region, which was drawn manually by experts. I also evaluated the selected shape priors based on the JI for the selected shape prior and true pancreas region.

Figure 4.5 shows typical examples of the segmentation results and the selected shape priors obtained using three methods: the proposed method (left), the method proposed by Lempitsky *et al.* (center), and a method without shape priors (right). Note that I employed the same segmentation processes for all three methods, with the exception of the graph-cut-based segmentation during the final step. The top row of Fig. 4.5 shows the selected shape priors (green region), and the bottom row shows the segmentation results (yellow region). Compared with the shape prior selected by the proposed algorithm, the one selected by the method proposed by Lempitsky *et al.* was not appropriate around the top of the pancreas, and produced a large segmentation error, as indicated by the blue arrows. This was consistent with the fact that the energy E for the algorithm proposed by Lempitsky *et al.* was higher than that of the proposed algorithm. In addition, the method without a shape prior over-segmented a region with a similar appearance as the pancreatic tissue marked by the red arrows. In this figure, the JI indicates that the proposed method performed better than both of the other methods in terms of both the accuracy of the selected shape prior and the segmentation results.

Figure 4.6 summarizes the evaluation of the segmentation results, the selected shape priors, and the segmentation energy for 140 test cases of Dataset-A, where the proposed method was compared with the method proposed by Lempitsky *et al.*

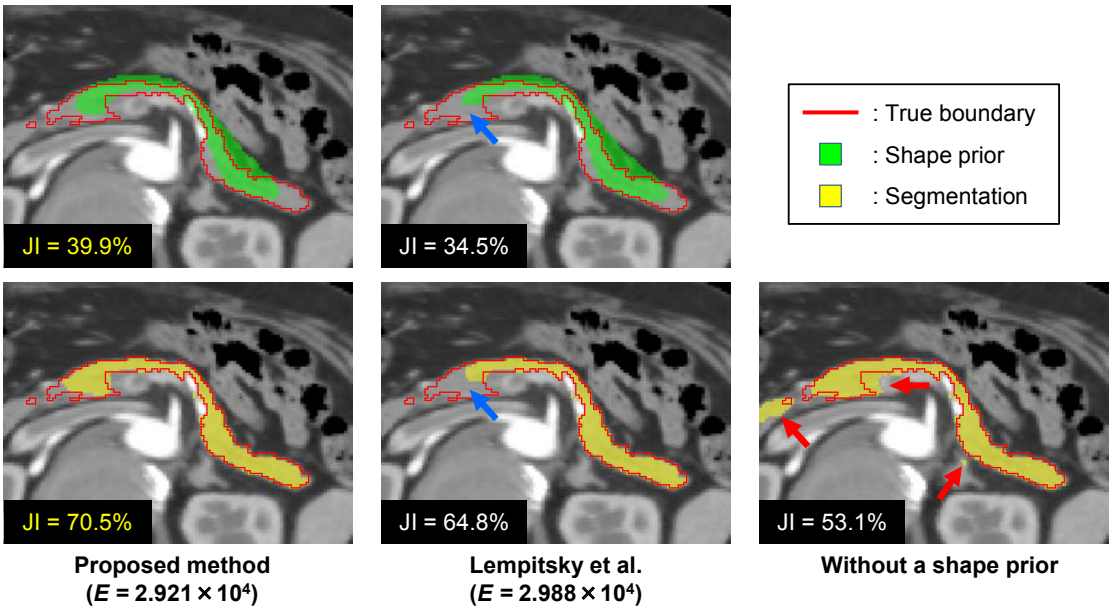

Fig. 4.5 Typical results obtained using the proposed method (*left*), Lempitsky *et al.*'s method (*center*), and the method without shape priors (*right*). The *top row* shows the selected shape priors (*green regions*), and the *bottom row* shows the segmentation results (*yellow regions*). The major false negatives are denoted by *blue arrows*, and the false positives are denoted by *red arrows*

and the method without shape priors, the latter of which corresponds to the results for $\lambda_2 = 0$. Using the proposed method, the average JI of the segmentation was improved by 1.3 pt compared with the method proposed by Lempitsky *et al.*, and by 3.7 pt compared with the method without shape priors. An analysis using a paired t-test with the null hypothesis (H0) that the JI is identical for both methods showed that the segmentation accuracy of the proposed method differed significantly from those of the method proposed by Lempitsky *et al.* ($p = 4.72 \times 10^{-2} < 0.05$) and the method without shape priors ($p = 7.59 \times 10^{-3} < 0.01$). The difference with the method proposed by Lempitsky *et al.* can be explained by the differences in the JI of the selected shape priors. The average JI of the selected shape priors increased by 2.1 pt compared with the method proposed by Lempitsky *et al.*, which is a statistically significant ($p = 1.99 \times 10^{-7} < 0.01$) difference. These observations are also consistent with the fact that the energy from the proposed method is equal to or less than that from the method proposed by Lempitsky *et al.* for all 140 cases in Dataset-A, which is theoretically expected.

Table 4.1 summarizes the computational cost per case, which was measured using a 3.1 GHz Intel® Xeon® CPU with two threads. In this table, the number of traversed nodes (A) is the number of reiterations of the two steps, i.e., branching and bounding, the computational cost of which was approximated as that of s-t mincut in the bounding computation. The number of leaf nodes (B) in this table indicates the number of predefined shape priors using the conventional algorithm (Lempitsky et al., 2012) and the total number of shapes generated by the SSM (= size $|\mathcal{S}|$) using the proposed algorithm. I approximated the size $|\mathcal{S}|$ as the average number of regions generated by dividing a square using lines [70]:

$$|\mathcal{S}| \sim \frac{1}{16}\ell(\ell-1)\pi + \ell + 1, \tag{4.22}$$

where ℓ is the number of lines $\phi^p(\boldsymbol{\alpha}) = 0$ that divide $\mathcal{R}_{\boldsymbol{\alpha}}$ into two nonempty sets, i.e., $\{\alpha \in \mathcal{R}_{\boldsymbol{\alpha}} \mid \phi^p(\boldsymbol{\alpha}) \geq 0\}$ and $\{\alpha \in \mathcal{R}_{\boldsymbol{\alpha}} \mid \phi^p(\boldsymbol{\alpha}) < 0\}$. Note that (B) represents the required number of s-t mincut computations when I conduct an exhaustive search over the shape priors, and corresponds to the worst-case complexity of the branch-and-bound optimization. The normalized number of traversed nodes (A/B) indicates the ratio of s-t mincut computations relative to that using an exhaustive search. The conventional algorithm [25] required 5.5 s for optimization and traversed 17.77 nodes per case, whereas the proposed method required 213 s and traversed 6.558×10^3 nodes.

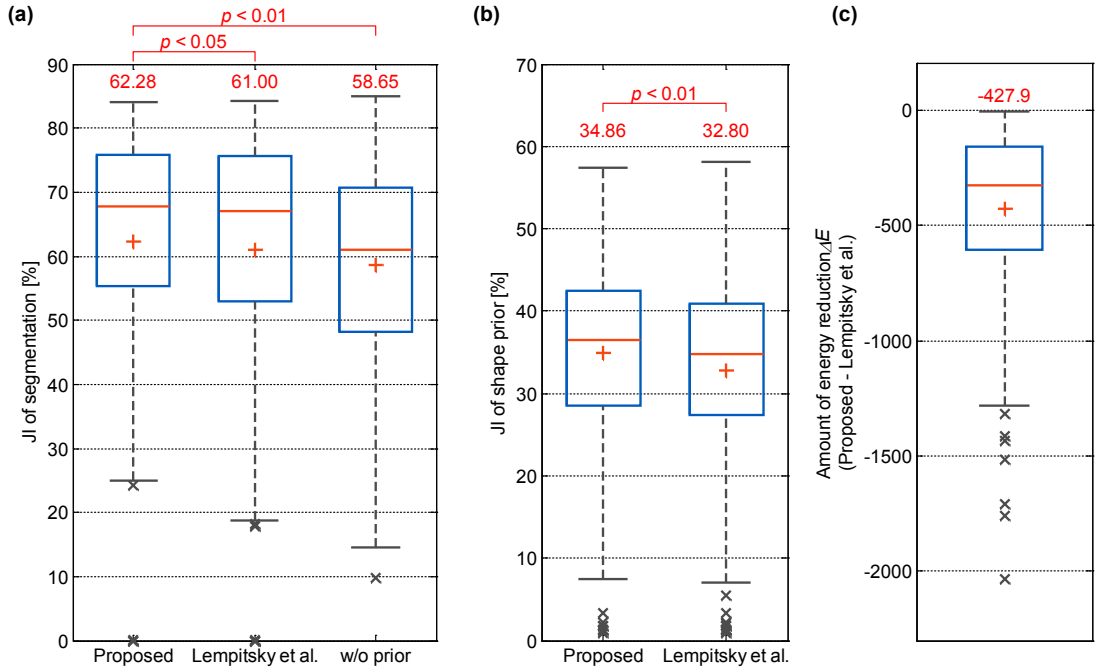

Fig. 4.6 Summary of the cross-validation test results for each method of pancreas segmentation using CT volumes from 140 patients. The box plots show the accuracy of the (a) segmentation, (b) shape priors, and (c) decrease in energy compared with Lempitsky *et al.*'s method. The segmentation accuracy was also compared to that obtained using the method without priors. The plus "+" signs in the box plots and the numerals above them indicate the average values. The results of the statistical tests of significance are also shown above the plots

Compared with the conventional method, the normalized number of nodes searched was dramatically reduced by the proposed method (from 0.3627 to 9.556×10^{-7}).

Table 4.1 Computational complexity for each pancreas segmentation using the proposed method and the method proposed by Lempitsky *et al.*

Method	Time required for hierarchical clustering	Optimization time	Total time
Proposed	–	213 s	213 s
Lempitsky *et al.*	22.6 s	5.5 s	28.1 s

Method	Number of nodes traversed (A)	Number of leaf nodes (B)	Normalized number of nodes traversed (A/B)
Proposed	6.558×10^3	6.863×10^9	9.556×10^{-7}
Lempitsky *et al.*	17.77	49	0.3627

4.3.2 Spleen segmentation

I also conducted spleen segmentation through the proposed algorithm using contrast-enhanced three-phase 3D CT volumes of 40 patients. I refer to these volumes as Dataset-A', which is a subset of Dataset-A. Dataset-A' was measured as 512 $\times$ 512 $\times$ (191–807) voxels with a spacing of (0.643–0.782) $\times$ (0.643–0.782) $\times$ (0.8–1.0) mm, which were reduced to 256 $\times$ 256 $\times$ (122–340) isotropic voxels of (1.092–1.564) mm/voxel for computational efficiency. I performed nonlinear registration among the three different phase volumes, followed by an abdominal cavity extraction and rough alignment of the cavities among the different subjects, all of which were conducted in the same manner as mentioned in Section 4.1. Note that the pose variance of the spleen was nearly eliminated by the abdominal cavity alignment because the spleen is located close to the abdominal cavity wall. The likelihood $\Pr\left(I_p \mid x_p\right)$ of Eq. (4.8) was assumed to be a 3D Gaussian mixture distribution consisting of four classes, e.g., spleen, liver, inferior vena cava (IVC), and other organs or tissues, and I used the training data to compute the initial values of the statistical parameters used in the EM algorithm, i.e., the average values and the variances of the foreground/background features. The posterior probability of the spleen was transformed using a linear function to balance that of the background, and it was forwarded to the graph cuts. The parameters used for the graph cuts were

determined experimentally and fixed to $(\lambda_1, \lambda_2, \sigma) = (0.25, 0.15, 12.0)$ throughout the spleen-segmentation experiment.

I used $d = 2$ and $w = 3.0$ for the number of eigenmodes of the level-set-based SSM and the size of $\mathcal{R}_\alpha$, respectively. The RBF-based three-phase registration employed a Gaussian kernel with a standard deviation of 22.5 mm. I employed a 26-neighborhood system for the graph cuts.

I conducted a cross-validation study using 40 subjects in Dataset-A', and I evaluated the segmentation accuracy based on the JI between the extracted region and the true region, which was drawn manually by experts. I also evaluated the selected shape priors based on the JI for the selected shape prior and the true spleen region.

Typical results of the spleen segmentation and the selected shape priors for the three methods are indicated in Fig. 4.7, where the top and bottom rows show the selected shape priors (green region) and the segmentation results (yellow region), respectively. For the method without a shape prior, the over-segmented region is marked by the red arrow, and was reduced by the proposed method. Compared with the method proposed by Lempitsky *et al.*, the proposed method selected a better shape prior and resulted in better segmentation. The optimal energy E of the proposed method was lower than that of the algorithm proposed by Lempitsky *et al.* This result indicates that the proposed method was superior to both of the other methods in terms of the accuracy of the selected shape prior and the segmentation results.

The box plots in Fig. 4.8 show the JI of the segmentation results for the proposed method compared with the method proposed by Lempitsky *et al.* and the method without shape priors for the selected shape priors, as well as the segmentation energy for the 40 cases during the testing stage. The average JI of the segmentation was improved by 0.5 pt compared with the method proposed by Lempitsky *et al.*, and by 7.2 pt compared with the method without shape priors. A paired t-test under the null hypothesis (H0) that the JI is identical for both methods revealed that there is a statistically significant difference in the segmentation accuracy among the proposed method, the method proposed by Lempitsky *et al.* ($p = 2.24 \times 10^{-3} < 0.01$), and the method without shape priors ($p = 1.85 \times 10^{-2} < 0.05$). Compared with the method proposed by Lempitsky *et al.*, the difference is explained based on the difference in the JI of the selected shape priors. The average JI of the selected shape priors increased by 1.9 pt compared with the method proposed by Lempitsky *et al.*, which is a statistically significant ($p = 1.84 \times 10^{-6} < 0.01$) difference. These observations are also consistent with the fact that the energy from the proposed method is equal

to or less than that of the method by Lempitsky *et al.* for all 40 cases, which was expected theoretically.

Table 4.2 summarizes the average computational cost for each spleen segmentation case measured using a 3.1 GHz Intel® Xeon® CPU with two threads. The conventional algorithm [25] required 17.8 s for optimization and traversed 13.65 nodes per case, whereas the proposed method required 586 s and traversed 7.456 $\times$ 103 nodes. The normalized number of nodes searched was reduced dramatically by the proposed method when compared with the conventional method (from 0.2786 to 1.779×10^{-7}), which conducted graph cuts given all possible shapes from an SSM.

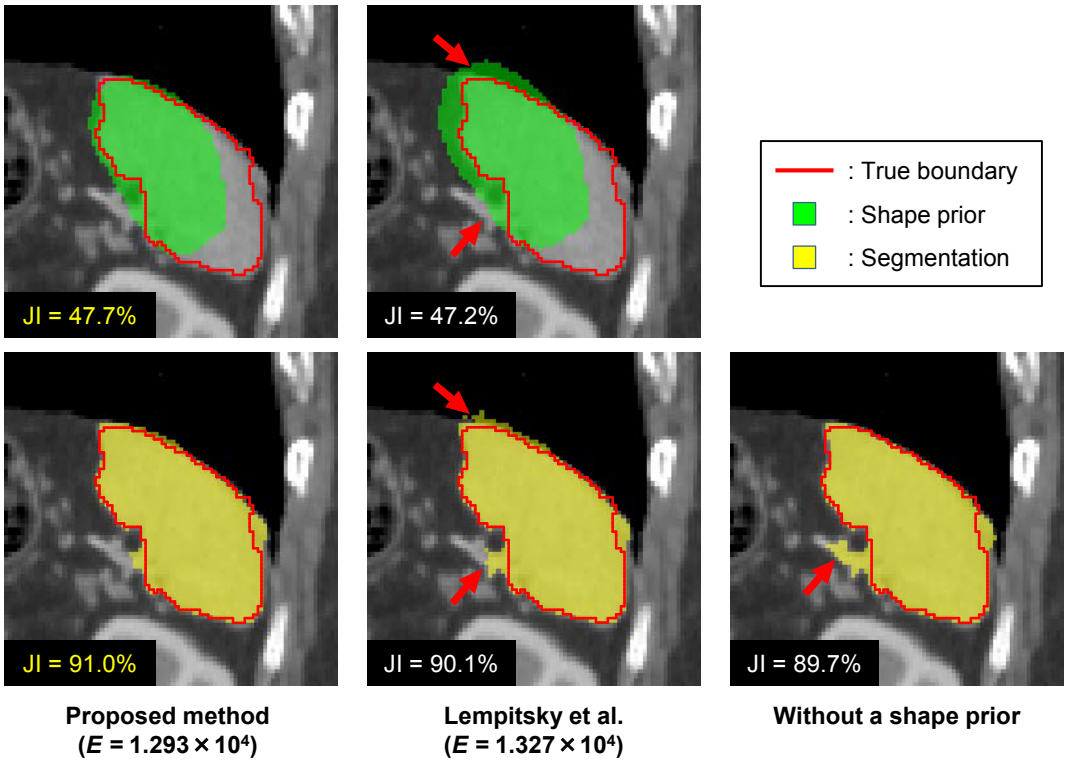

Fig. 4.7 Saggital view of the typical results obtained using the proposed method (*left*), Lempitsky *et al.*'s method (*center*), and the method without shape priors (*right*). The top row shows the selected shape priors (*green regions*), and the bottom row shows the segmentation results (*yellow regions*). The major false positives are denoted by the red arrows

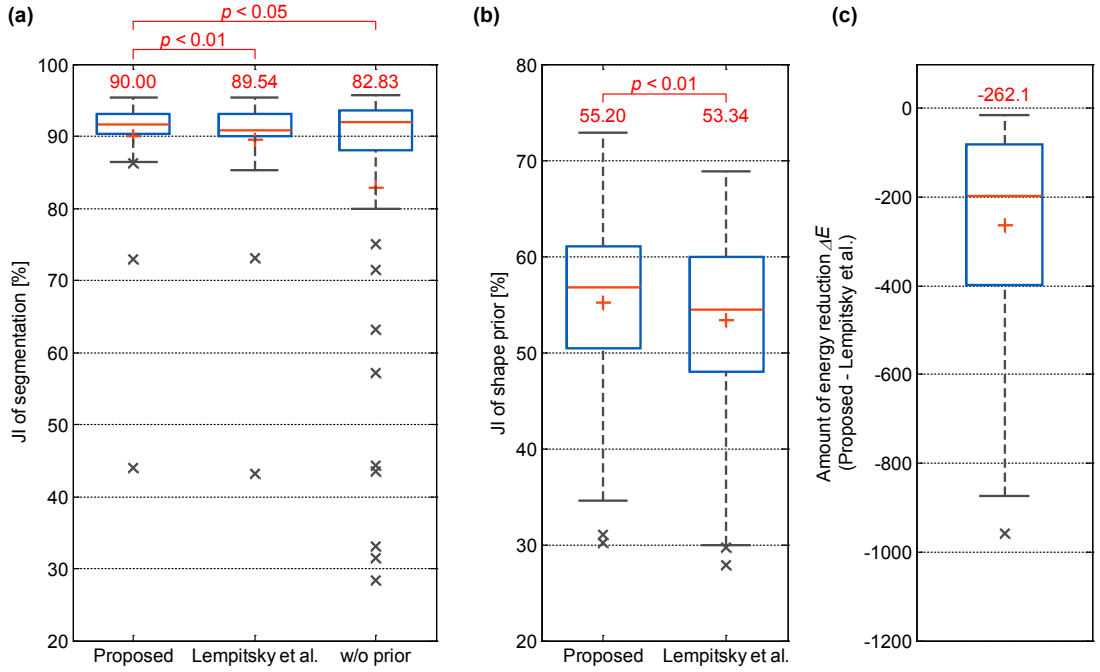

Fig. 4.8 Summary of the cross validation test results for spleen segmentation using CT volumes from 40 patients for each method. The box plots show the accuracy of (a) the segmentation (b) the shape priors, and (c) the decrease in energy compared with Lempitsky *et al.*'s method. The segmentation accuracy was also compared to that obtained using the method without priors. The plus "+" signs in the box plots and the numerals above them indicate the average values. The results of the statistical tests of significance are also shown above the plots

Table 4.2 Computational complexity for each spleen-segmentation case using the proposed method and the method proposed by Lempitsky *et al.*

Method	Time required for hierarchical clustering	Optimization time	Total time
Proposed	–	586 s	586 s
Lempitsky *et al.*'s	14.4 s	17.8 s	32.2 s

Method	Number of nodes traversed (A)	Number of leaf nodes (B)	Normalized number of nodes traversed (A/B)
Proposed	7.456×10^3	4.194×10^{10}	1.779×10^{-7}
Lempitsky *et al.*'s	13.65	49	0.2786

4.3.3 Comparison experiment with the state-of-the-art segmentation algorithm

I compared the proposed algorithm with one of the state-of-the art segmentation algorithms used for the pancreas and spleen. Because there is no single organ-segmentation algorithm for the pancreas and/or spleen under the same contrast conditions, I focused on the latest segmentation algorithm of multiple organs, or the liver, left and right kidneys, pancreas, and spleen, with a PDM-based conditional SSM for a single contrast condition [52]. A well-known advantage of multi-organ segmentation with a multi-organ SSM over single-organ segmentation with a single-organ SSM is that the spatial relationship between neighboring organs can be incorporated in the process, which is highly useful for segmentation.

I conducted the comparative experiment using the same test dataset in 4.3.1 and 4.3.2. To ensure that the difference in the training datasets for the two algorithms being compared do not introduce a negative influence on the results, I prepared a sufficient number of additional training datasets (Dataset-B) comprising eighty cases from the same hospital, and carried out re-training of their algorithm using the software provided by their research group. Specifically, I evaluated both algorithms by performing two-fold cross validation of Dataset-A and Dataset-A', but in the training phase, I also used Dataset-B, which comprised eighty cases, for each fold to train the multi-organ segmentation algorithm only. This was done because it was expected that the multi-organ algorithm would require a larger number of training data to describe the variation between organs. Figure 4.9 summarizes the number of training data used to train their conditional SSM and organ-correlation graph (OCG) for each fold. Dataset-B consists of 3D CT volumes having $512 \times 512 \times$ (166–310) voxels with a spacing of (0.488–0.782) $\times$ (0.488–0.782) $\times$ (0.8–1.0) mm/voxel, and whose size and spacing are similar to those of Dataset-A and Dataset-A'. The segmentation was executed on an early-phase CT volume, which is rich in contrast information.

The segmentation results of the same test dataset, or Dataset-A of 140 pancreas and Dataset-A' of 40 spleen, are summarized in Fig. 4.10 and Table 4.3, where the JIs of my algorithm achieved the best result in terms of the average JI. However, the median JI of the spleen, which was obtained by Okada's multi-organ segmentation, was slightly better than that of my algorithm. To evaluate the statistical difference between any pair of two algorithms, I conducted a paired t-test under the null hypothesis (H0) that the JI is identical for both methods. In summary, there was

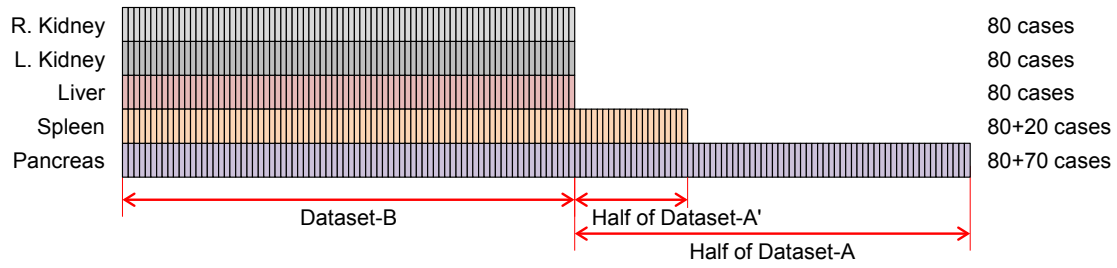

Fig. 4.9 Number of training data used to train the conditional SSM and organ-correlation graph (OCG) [52]. In the two-fold cross validation, the training phase of each fold used not only half of Dataset-A (or Dataset-A'), but also all of the data in Dataset-B when training the Okada's algorithm. Note that the test data are exactly identical to those used in Sections 4.3.1 and 4.3.2

no statistical difference between my algorithm and the multi-organ segmentation algorithm.

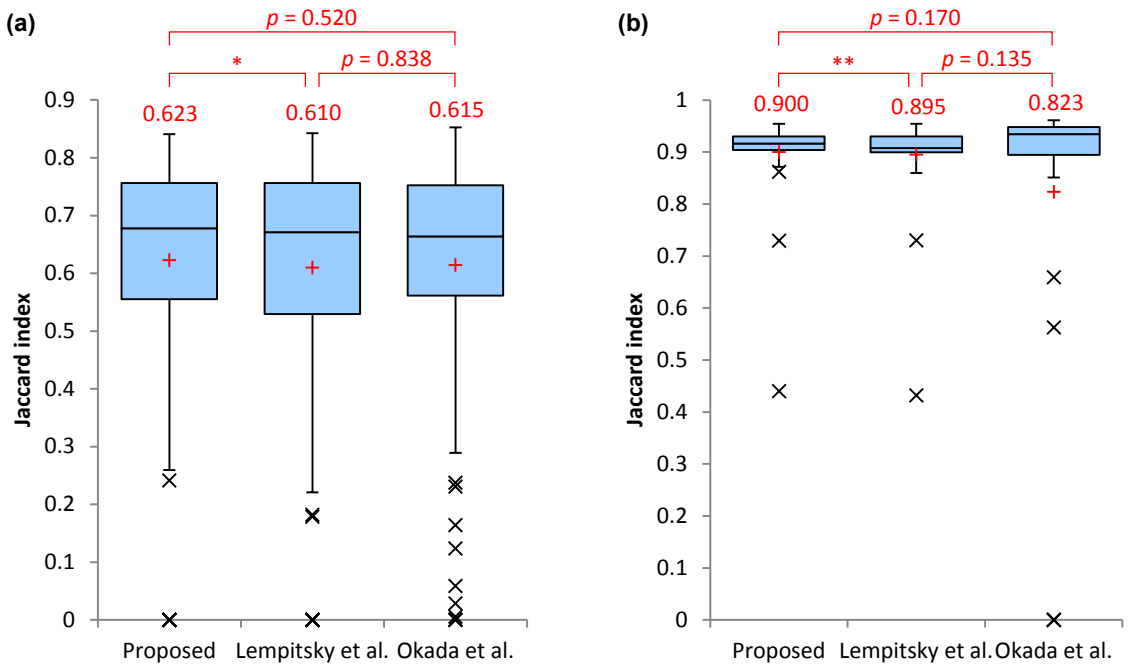

Fig. 4.10 Summary of the cross-validation test results for (a) pancreas segmentation using 140 CT volumes and (b) spleen segmentation using 40 CT volumes for the proposed method, the method proposed by Lempitsky *et al.*, and the method proposed by Okada *et al.* The box plots show the JI of the segmentation result. The "+" signs in the box plots and the numerals above them indicate the average values. The results of the statistical tests of significance are also shown above the plots.

Table 4.3 The segmentation results obtained using the same test data, i.e., 140 cases for the pancreas and 40 cases for the spleen.

Method	Pancreas		Spleen	
	JI [%] (±SD)	DSI [%] (±SD)	JI [%] (±SD)	DSI [%] (±SD)
Proposed	62.3 (±19.5)	74.4 (±20.2)	90.0 (±8.2)	94.5 (±5.8)
Lempitsky *et al.*	61.0 (±21.3)	72.9 (±22.5)	89.5 (±8.4)	94.2 (± 5.9)
Okada *et al.*	61.5 (±19.3)	73.9 (±19.6)	82.3 (±28.8)	85.8 (±29.4)
Performance reported in [52] using different test dataset	60.1 (±18.2)	72.5 (±17.6)	87.0 (±9.6)	92.1 (±8.1)

4.4 Discussion

4.4.1 Segmentation performance

First, I discuss the effects of the selected shape priors on the segmentation performance. As shown in Figs. 4.4–4.8, the proposed algorithm obtained a better shape prior compared with the method proposed by Lempitsky *et al.*, and it yielded better segmentation results. The examples shown in Figs. 4.11(a) and (b) illustrate cases with the most improved segmentation performance for the pancreas and spleen, respectively. The results suggest that there is a strong correlation between the accuracy of the shape prior and the segmentation performance. Figure 4.12 shows this relationship in terms of the JI, which was computed for 140 pancreas segmentation cases and 40 spleen segmentation cases using the proposed method. The improvement in the shape prior appeared to be more positively correlated to the pancreas segmentation. The value of Pearson's linear correlation coefficient for the pancreas segmentation was $R = 0.7857$ ($p < 0.01$; H0, no correlation). On the other hand, for the spleen segmentation, I observed a weaker but statistically significant correlation ($R = 0.5634$ and $p < 0.01$). Therefore, I conclude that the optimization of the shape priors from the perspective of the energy functional used for segmentation along with the proposed algorithm successfully improved the performance of both pancreas and spleen segmentation. However, this improvement appeared to be incremental, and I considered the possibility that the method proposed by Lempitsky *et al.* found a near-optimal solution, resulting in a small improvement. However, it is worth adding that the solution obtained using the method proposed by Lempitsky *et al.* was not globally optimal, resulting in a small

but steady performance improvement in the proposed method, i.e., from 61.0 to 62.3 % for pancreas segmentation, and from 89.5 % to 90.0 % for spleen segmentation, both with a statistically significant difference.

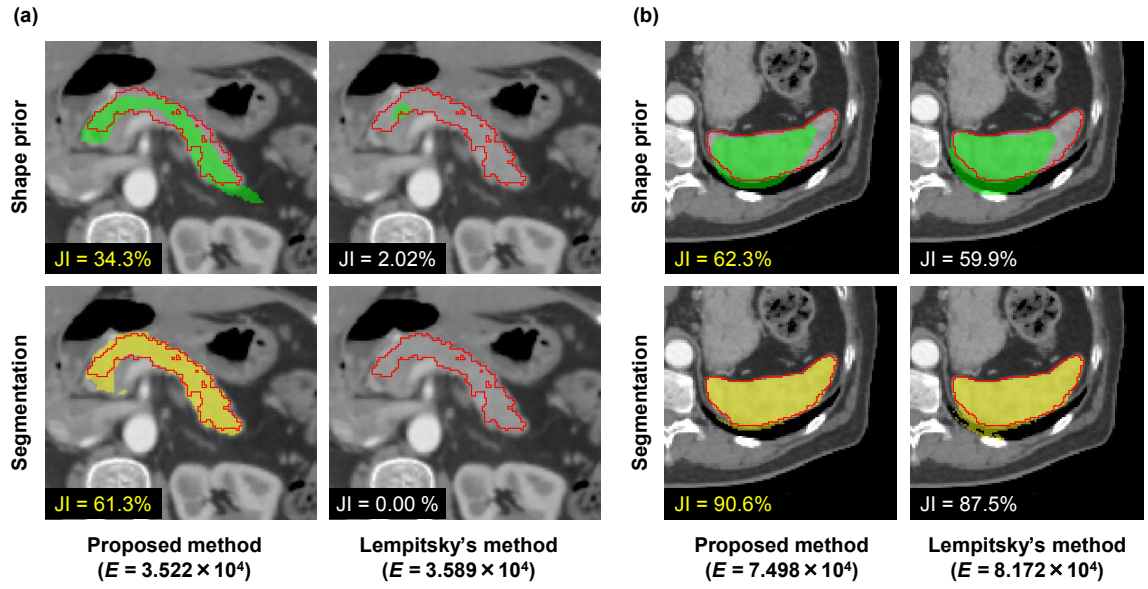

Fig. 4.11 The most-improved case from the proposed method compared with Lempitsky *et al.*'s method in terms of JI for (a) pancreas and (b) spleen segmentation. The *top row* shows the selected shape priors, and the *bottom row* shows the segmentation results

Second, I compare the results obtained using the proposed method against those recently reported pancreas and spleen segmentation algorithms, whose performances are summarized in Tables 4.4 and 4.5. The tables list the performance indices and the input contrast conditions, along with the number of test cases used. A simple comparison that was carried out using the indices only indicated that the proposed algorithm achieved the best performance for the pancreas segmentation and good performance comparable to the state-of-the-art algorithms for the spleen segmentation. However, such a simple comparison may be misleading. The difference in the performance is due not only to the differences in the algorithms and input contrast conditions, but also to the difference in the test data. To realize a fair comparison between two algorithms, it is necessary to at least use the same test data. For the purpose of showing that my algorithm extracts the pancreas and spleen precisely as well as the state-of-the-art segmentation algorithm of the pancreas and spleen, I focused on the algorithm proposed by Okada et al. [52], because it appears

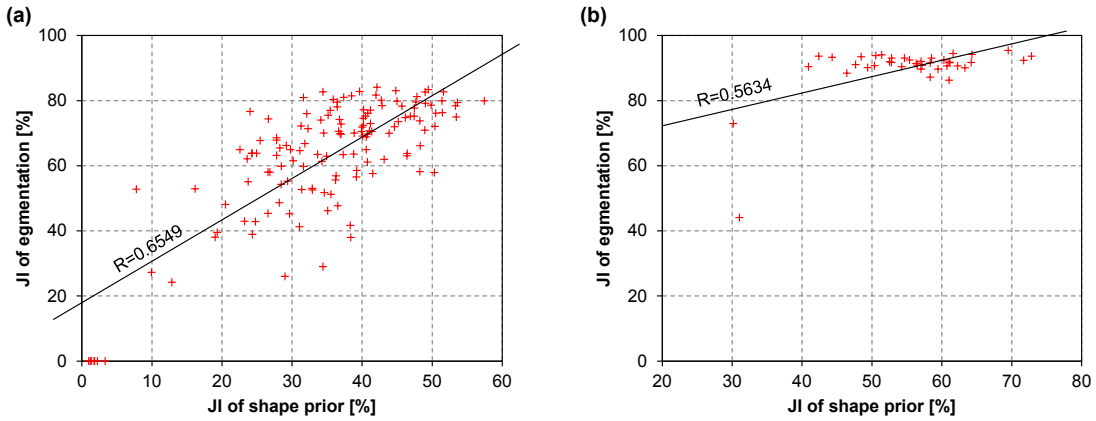

Fig. 4.12 Relationship between the accuracy of the segmentation and the selected shape prior of (a) the pancreas and (b) spleen for the JI computed from 140 and 40 cases, respectively, using the proposed method

in both Table 4.4 and 4.5, and it is the latest one. I compared my algorithm with that proposed by Okada's algorithm using the same test data. To reduce the influence of the difference in the training dataset, I re-trained Okada's algorithm using the same training data as Dataset-A or Dataset-A' for each fold of the cross validation. In addition, I prepared 80 additional cases for training Okada's algorithm, mainly in training of a PDM-based conditional SSM and OCG, with the training software provided by his research group. While it may be a concern that there is a difference in the number of training datasets, it should be noted that training a multi-organ SSM generally requires more data than training a single-organ SSM, because of the larger variation among organs. One possible advantage of such a multi-organ SSM is that it considers spatial correlations among neighboring organs that are inherent in human anatomy. As presented in the results in Fig. 4.10 with the statistical test, I concluded that the two algorithms were comparable with each other with respect to the segmentation performance. This conclusion suggests that the segmentation performance showed in this paper is the highest level of pancreas and spleen segmentation.

Third, I discuss other abdominal organ-segmentation algorithms, with the exception of the pancreas or spleen. In the last five years, there have been over 50 journal papers, including survey papers [74–76], that have been published in major international journals. Target organs are as follows: approximately 60 % of papers for the liver [77, 78], approximately 20 % for the prostate [79, 80], approximately

Table 4.4 Comparison of my automated segmentation method for the pancreas based on the performance indices reported for automated state-of-the-art pancreas segmentation methods. The methods are partitioned into three groups that are divided by the solid lines. The top group comprises my method and the method proposed by Lempitsky et al., where the shape priors were selected from a set of uniformly sampled shapes in the eigenshape space of an SSM. The middle group comprises single-organ- (pancreas) segmentation methods, and the bottom group comprises multiple-organ-segmentation methods including the pancreas. The average JI and DSI results from my method were better than those obtained by all previously reported automated pancreas-segmentation methods.

Methods	Input Image(s)	Test cases	JI [%] ($\pm SD$)	DSI [%] ($\pm SD$)
Proposed	3 (multi-phase)	140	62.3 ($\pm$19.5)	74.4 ($\pm$20.2)
Lempitsky *et al.*	3 (multi-phase)	140	61.0 ($\pm$21.3)	72.9 ($\pm$22.5)
Karasawa et al. [57]	1 (portal-phase)	150	60.5	73.4
Roth et al. [56]	1 (portal-phase)	82	–	71.8 ($\pm$10.7)
Farag et al. [55]	1 (portal-phase)	80	57.2	68.8
Erdt et al. [54]	1 (portal-phase)	40	61.2 ($\pm$9.08)	–
Shimizu et al. [49]	3 (multi-phase)	20	57.9	–
Kitasaka et al. [53]	4 (multi-phase)	22	12 fine, 6 medium, 4 poor cases‡	
Wolz et al. [51]	1 (portal-phase)	150	55.5 ($\pm$17.1)	69.6 ($\pm$16.7)
Chu et al. [71]	1 (portal-phase)	100	54.6	69.1 ($\pm$15.3)
Okada et al. [72]	1 (arbitrary phase)	86	58.0	71.8
Shimizu et al. [1]†	1 (non-contrast)	10	35.0	–

†Re-substitution method

‡Visual assesment results

Table 4.5 Comparison of my automated segmentation method for the spleen based on the performance indices reported for automated state-of-the-art spleen segmentation methods. The methods are partitioned into three groups divided by the solid lines. The top group comprises my method and the method proposed by Lempitsky et al., where the shape priors were selected from a set of uniformly sampled shapes in the eigenshape space of an SSM. The middle group comprises single-organ-(spleen) segmentation methods, and the bottom group comprises multiple-organ-segmentation methods including the spleen. The average JI and DSI results from my method were better than those obtained by all previously reported automated spleen-segmentation methods. Although several authors compared the results between datasets with different resolutions and/or contrast conditions, only the best results are displayed here.

Methods	Input Image(s)	Test cases	JI [%] ($\pm SD$)	DSI [%] ($\pm SD$)
Proposed	3 (multi-phase)	40	90.0 ($\pm$8.2)	94.5 ($\pm$5.8)
Lempitsky *et al.*	3 (multi-phase)	40	89.5 ($\pm$8.4)	94.2 ($\pm$5.9)
Linguraru et al. [73]	1 (portal-phase)	10	91.0 ($\pm$2.6)	95.2 ($\pm$1.4)
Okada et al. [52]	1 (arbitrary phase)	134	87.0 ($\pm$9.6)	92.1 ($\pm$8.1)
Linguraru et al. [39]	2 (multi-phase)	10	–	93.6 ($\pm$1.8)
Wolz et al. [51]	1 (portal-phase)	150	86.2 ($\pm$12.7)	92.0 ($\pm$9.2)
Chu et al. [71]	1 (portal-phase)	100	84.5	91.4 ($\pm$5.7)
Shimizu et al. [1]†	1 (non-contrast)	10	83.5	–

†Re-substitution method

25 % for the kidney [81, 82], and approximately 10 % for multiple organs including the gallbladder [51, 52]. Note that I counted the number redundantly in the case of multiple-organ segmentation, and listed only a few papers of the over 50 papers in a reference list, because this paper is not a review paper of abdominal organ segmentation. The major imaging modality is CT, or over 60 %, and magnetic resonance for approximately 30 % and ultrasound for approximately 10 %. From a technological viewpoint, the most commonly used prior for segmentation was derived from an SSM in approximately 30 % of papers, and a multi-atlas-based prior also gave a useful prior in approximately 10 % of the papers. Graph cuts is a major approach in the energy-optimization-based segmentation and over 20 % of papers employed the approach. A few papers tried to integrate priors derived from atlas [39] or SSM [77] into the graph-cuts-based approach.

While the applicability of the above algorithms to the pancreas or spleen may be of some interest, it is very difficult to consider because most algorithms were configured for the target organ(s) using target specific prior knowledge in an explicit or implicit manner. To realize a fair quantitative comparison, it is necessary to completely eliminate and develop a new algorithm, which is nearly impossible.

Recent trends in abdominal-organ segmentation include multiple-organ segmentation with a multi-atlas Wolz et al. [51] or a multi-organ SSM Okada et al. [52], because such a multi-atlas or SSM evaluates the spatial relationship between neighboring organs, which is inherent to human anatomy. Note that an algorithm for multi-organs not necessarily outperform an algorithm for a single organ, because there are many major and minor problems to be solved in organ segmentation. Note also that a multi-organ SSM can efficiently solve a problem caused by the correlation between neighboring organs, but do not solve other problems such as the global optimization addressed in this paper. From a historical viewpoint of medical-image analysis, technological advancements have been achieved in a spiral manner, where gradual advances aimed at different problems were presented by many researchers, and a researcher integrated them into an algorithm, followed by further improvements of the algorithm by many researchers. In this sense, the solution presented in this paper will be integrated into a multi-organ-segmentation algorithm in the near future in the hope of realizing a comprehensive solution of the organ-segmentation problem.

4.4.2 Computational efficiency

Now, I discuss the computational efficiency of the proposed algorithm based on Tables 4.1 and 4.2. Compared with the method proposed by Lempitsky *et al.*, the proposed method increases the number of nodes traversed for pancreas and spleen segmentation from 17.77 and 13.65 to 6.558×10^3 and 7.456×10^3, respectively, which increased the computational time from 5.5 s and 17.8 s to 213 s and 586 s , respectively. This may suggest that there is a possible disadvantage of the proposed algorithm. However, it should be noted that the number of leaf nodes or shape priors that were considered during segmentation is approximately 10^8 times greater for the proposed algorithm than for the method proposed by Lempitsky *et al.* To ensure a fair comparison, I divided the number of nodes traversed by the number of leaf nodes, which I defined as the normalized number of traversed nodes in the present study. The normalized number showed that the proposed algorithm significantly reduced the number from 0.3627 and 0.2786 to 9.556×10^{-7} and 1.779×10^{-7}, respectively; thus, the proposed algorithm was approximately 3.80×10^5 and 1.57×10^6 times more efficient than the conventional method. Another advantage of the proposed method compared with the conventional method is that it does not require a predefined hierarchical cluster tree, which increases the computational costs on the order of $O(n^2)$ (where n is the sampling size) [83]. The computational cost of the clustering process may be a major problem if the number of shape priors used in 3D segmentation is increased using the method proposed by Lempitsky *et al.* If we assume that all possible 3D shapes (6.863×10^9) are actually generated from an SSM, and we use a clustering algorithm where the computational cost increases according to the complexity of $O(n^2)$, followed by a graph-cut segmentation using the method proposed by Lempitsky *et al.* , it is clear that the computational costs of clustering will be significant, and a large memory capacity will also be required to store the shapes. For example, the computational cost for the shape clustering consists of 1) computation of a pairwise symmetric distance matrix and 2) hierarchical clustering based on the distance matrix, where the former alone costs over 3.73×10^{14} s (over 10^7 years), which is based on an approximated number of pairs of $1/2 \times (10^9)^2$ and an 0.746-ms average computational time of the Hamming distance for a pair using a single-thread 3.1 GHz CPU. In addition, the amount of memory required to hold an entire clustering tree is 2.04×10^{15} bytes ($=$ 2.04 PB), which is the number of nodes ($2 \times 10^9 - 1$) multiplied by the memory size of the image ($193 \times 146 \times 145$ voxels $\times 2$ bits). In contrast, the proposed algorithm does not require a clustering process for a predefined shape template or a hierarchical cluster tree, nor does it

construct a search tree using all shapes, thereby resulting in a lower computational time and less memory during segmentation. In addition, the main advantage of the proposed algorithm is that it is theoretically guaranteed that a truly optimal solution is obtained in terms of the given energy functional from all possible shapes (6.863×10^9), whereas this is not true for the method proposed by Lempitsky *et al.*, except when all possible shapes are utilized. This incurs a significant computational cost and requires a very large memory capacity, as mentioned above.

Next, I discuss the effects of the specific voxel-selection operation, $Select(Q)$, which is used as the eigenshape space partitioning algorithm. Figure 4.13 shows a scatter plot of the number of nodes traversed using the proposed voxel-selection operation with Eq. (4.20) and that obtained through a random selection. It is important to note that using the proposed operation, the number was reduced in all 140 cases for the pancreas and all 40 cases for the spleen, where all of the points are plotted below the diagonal line in Fig. 4.13. Compared with a random selection, the proposed selection operation successfully reduced the average number from 9,988 and 11,411 to 6,558 and 7,460 for the pancreas and spleen, respectively, thereby reducing the average optimization time from 305 s and 1,437 s to 213 s and 586 s, respectively. Note that the choice of the selection method does not affect the optimal shape priors, segmentation results, or minimized energy, which is obvious from the perspective of the branch-and-bound theory. I also computed the depth of the leaf node in which the optimal solution was found because of the high correlation between the depth and the number of nodes traversed. Figure 4.14 shows histograms of the depth of the optimal solution node with the proposed selection operator and a random selection operator. Figure 4.14 confirms that the proposed selection operator greatly reduces the depth of the optimal solution for both the pancreas and spleen ($p < 0.01$). The proposed selection operator successfully balances the search tree and incurs lower computational costs than a random selection operator.

4.4.3 Limitations

Next, I discuss some limitations of the proposed method. Figure 4.15(a) shows the worst case compared with the method proposed by Lempitsky *et al.* in terms of the segmentation accuracy for the pancreas, whereas the proposed algorithm decreased the JI by 10.1pt (from 73.8 % to 63.7 %). This failure of the proposed algorithm may be attributed to the inability to select an appropriate shape prior, as shown in the top row of Fig. 4.15(a). Note that the proposed algorithm can find a shape prior that truly minimizes the energy of the graph cuts, and the shape

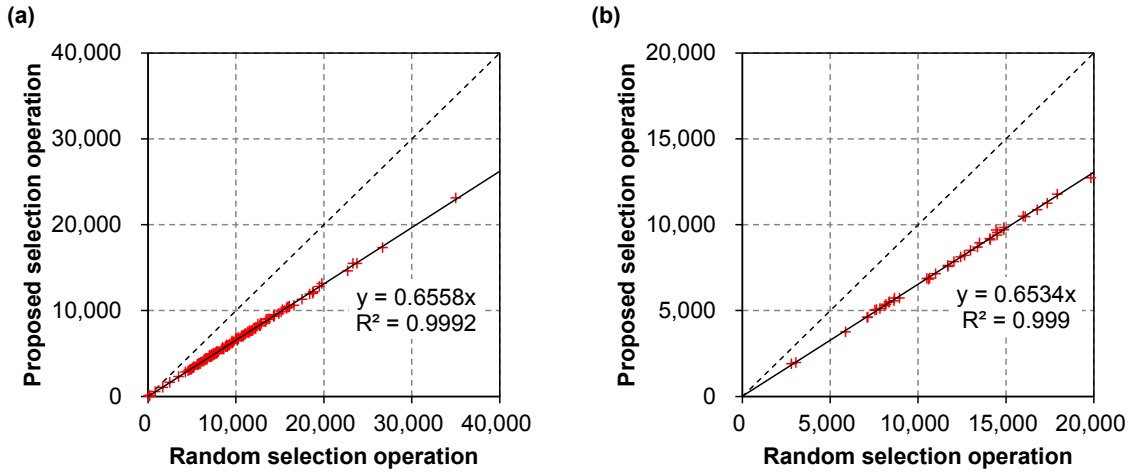

Fig. 4.13 Comparison of the number of nodes traversed using different voxel selection operations of (a) pancreas and (b) spleen segmentation. The horizontal and vertical axes of each plot correspond to a random selection operator and the proposed selection operator, respectively. The dotted diagonal line shows that the optimization times were equal using both operators

prior shown in the top left of Fig. 4.15 was an optimal shape in terms of the energy functional used in my experiment. However, despite the lower energy compared to that in the method proposed by Lempitsky *et al.*, the JI was degraded because of the inconsistency problem between the JI and the energy. An example of this problem was illustrated by Nakagomi et al. [21], where the JI was decreased while the energy functional monotonically decreased. It should be noted that this problem may not be observed by many researchers when the optimization process gets trapped in the local minimum. However, this problem is faced by almost all existing segmentation algorithms that are based on optimization theory. A few researchers have studied the optimal design of the objective function [84], which is quite an interesting topic but out of the scope of this study, and remains as future work. Another limitation is that the aforementioned quantitative validation results depend on the application (target organs) and the hyper-parameters used in the experiment, such as the number of eigenshape modes and the statistical analysis method used to construct an SSM. For other applications or parameter sets, the difference between the proposed algorithm and the conventional method may be either increased or decreased. It should be noted that the conclusions derived from the quantitative experiments described above were affected by the conditions. Despite these limitations, I consider that the main features of the proposed method will not be affected by different applications

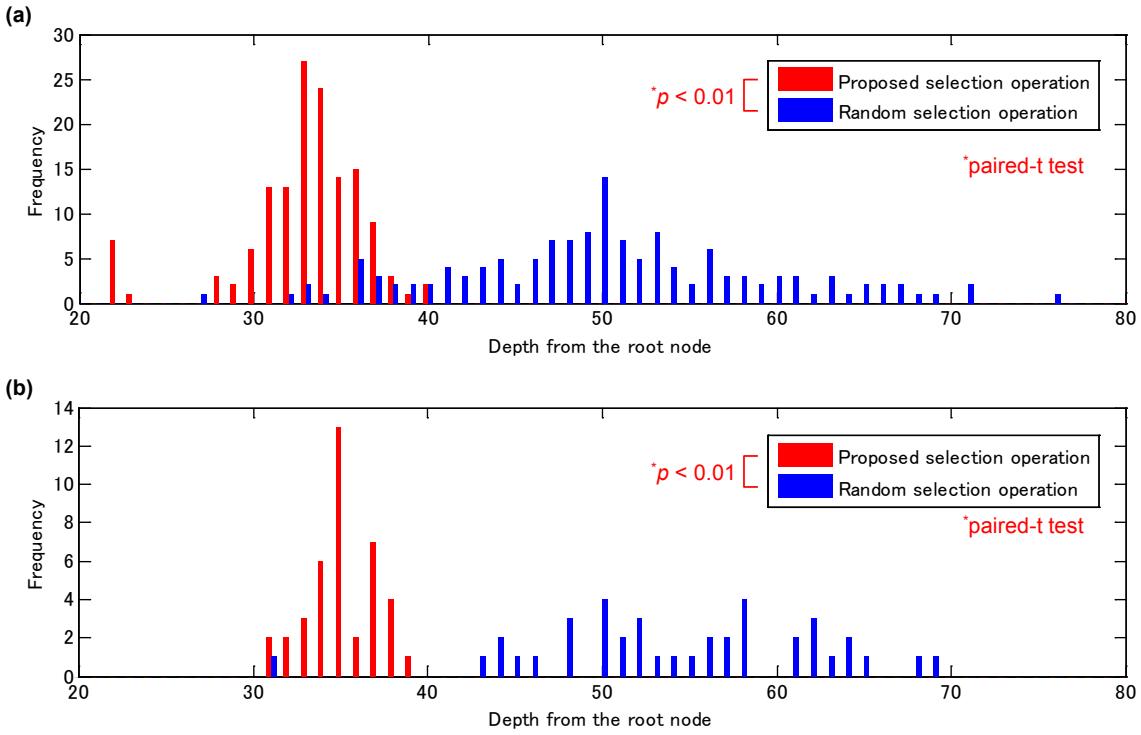

Fig. 4.14 Histograms showing the relationship between the depth of a leaf node with the optimal solution and the root node of a binary tree. The blue bars correspond to a random selection operator, and the red bars correspond to the proposed selection operator. There was a significant difference between the two distributions ($p < 0.01$)

or parameter sets. In particular, the proposed algorithm can find an optimal shape among all possible shapes generated from an SSM without requiring the clustering of predefined shapes or a predefined hierarchical cluster tree, both of which are prerequisites for conventional algorithms. The computational complexity of the optimization for a higher number of dimensions d is also an interesting topic of discussion. The number of leaf nodes $|\mathcal{S}|$, i.e., the shape priors to be considered during segmentation, increases drastically as d increases. An explicit form of the average size of $|\mathcal{S}|$ is also given for $d = 3$ [70], where ℓ is the number of planes used for partitioning a cubic region:

$$|\mathcal{S}| \sim \frac{1}{314}(2\ell + 23)\ell(\ell - 1)\pi + \ell + 1 \text{ for } d = 3 \tag{4.23}$$

In pancreas segmentation, the average value of ℓ is 1.85×10^5. Thus, $|\mathcal{S}|$ is expected to be 6.72×10^9 when $d = 2$ and 1.23×10^{14} when $d = 3$. This means that when d increases from 2 to 3, the number of shape priors to be considered increases by over 10,000 times, which may lead to an intractable computational cost. Thus, an improvement in the computational efficacy for a higher number of dimensions is an important topic to be addressed in future.

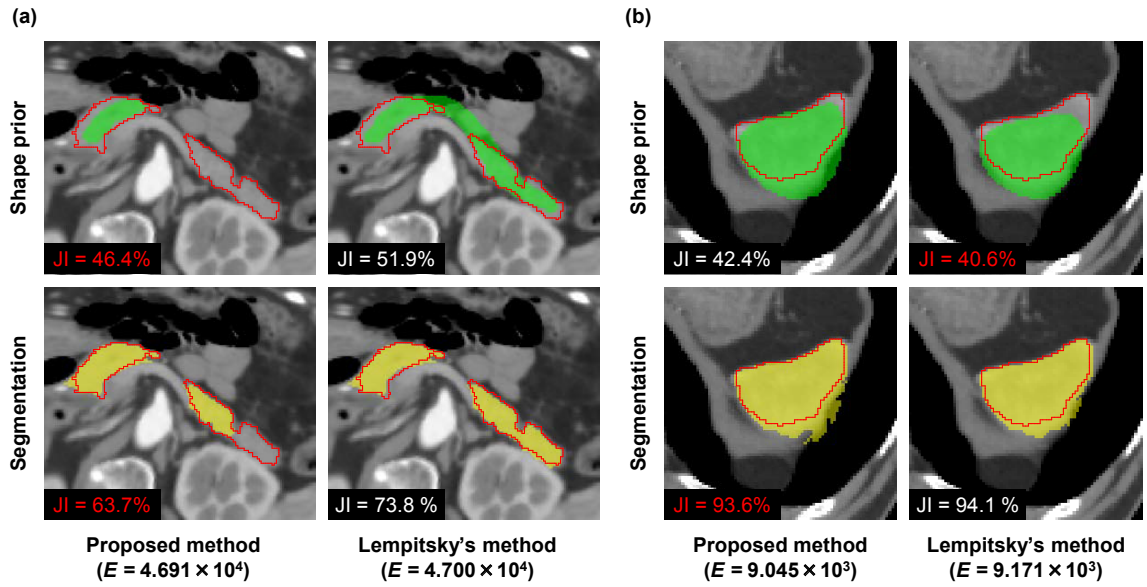

Fig. 4.15 Worst-case performance compared with Lempitsky *et al.*'s method in terms of the segmentation accuracy

4.4.4 Extensibility of the proposed framework

It is important to discuss the extensibility of the proposed framework to different SSMs and energy functionals. To clarify the conditions of the SSM and energy functional that are available in my framework, I showed the sufficient conditions to compute the lower bound of an energy functional above. To further enhance the advantage offered by my framework, I discuss the extension of the conditions, which are summarized as follows.

SSM

The SSM that is applicable to my framework can be generalized as follows:

$$g_p(\alpha) = \mathcal{H}\left(f(\phi^p(\boldsymbol{\alpha})) - t\right) \tag{4.24}$$

where $f : \mathbb{R} \to \mathbb{R}$ is a monotonically increasing function, $\phi^p(\boldsymbol{\alpha})$ is a linear function of $\boldsymbol{\alpha} \in \mathcal{R}_{\boldsymbol{\alpha}}$, and $t \in \mathbb{R}$ is a threshold parameter. An SSM defined by f and $t \in \mathbb{R}$ is applicable to my framework, and the global solution is computed efficiently. The proof is given in Appendix B.

Based on the extension using f and t, a possible shape representation $\boldsymbol{\phi}(\boldsymbol{\alpha})$ includes not only a level-set function [17] but also LogOdds [12] and Label Space [13]. Moreover, we can employ $\boldsymbol{\phi}(\boldsymbol{\alpha})$ defined on an additive log-ratio (ALR) or isometric log-ratio (ILR) space [14] by mapping it to the label space using a monotonically increasing function, f, that makes some of the nonlinear shape representations available. Note that I assume a binary shape representation that can be derived from the above shape representations.

Of course, different linear statistical analysis methods such as independent component analysis (ICA) are applicable to the model $\boldsymbol{\phi}(\boldsymbol{\alpha})$, which derives another linear function in terms of $\boldsymbol{\alpha}$. A user can choose a suitable shape representation and statistical analysis method from among the above methods depending on the problem being considered.

Energy Functional

Suppose $h_p^F(\mathbf{y})$ and $h_p^B(\mathbf{y})$ ($p \in \mathcal{V}$) are monotonically decreasing and increasing penalty functions ($\mathcal{L}^{|\mathcal{V}|} \to \mathbb{R}$), respectively, in a high-dimensional discrete space of $\mathbf{y}$.

Then, the shape energy terms can be generalized as follows:

$$F^p(\boldsymbol{I}, \mathbf{y}) = \lambda_1 \cdot \Pr\left(x_p = 0 \mid I_p\right) + \lambda_2 \cdot h_p^F(\mathbf{y}) \tag{4.25}$$

$$B^p(\boldsymbol{I}, \mathbf{y}) = \lambda_1 \cdot \Pr\left(x_p = 1 \mid I_p\right) + \lambda_2 \cdot h_p^B(\mathbf{y}) \tag{4.26}$$

Note that the functions $h_p^F(\mathbf{y})$ and $h_p^B(\mathbf{y})$ satisfy the following inequalities:

$$h_p^F(\mathbf{y}) \geq h_p^F(\mathbf{y}') \, \forall p \in \mathcal{V} \tag{4.27}$$

$$h_p^B(\mathbf{y}) \leq h_p^B(\mathbf{y}') \, \forall p \in \mathcal{V} \tag{4.28}$$

where $\{\mathbf{y}, \mathbf{y}\} \in \mathcal{L}^{|\mathcal{V}|}$ is a pair of shape label sets such that $y_q \leq y'_q \, \forall p \in \mathcal{V}$. Under the above conditions, we can derive the lower bound as follows:

$$\begin{aligned}
&\min_{\boldsymbol{\alpha} \in \mathcal{R}_{\boldsymbol{\alpha}}} \min_{\mathbf{x} \in \mathcal{L}^{|\mathcal{V}|}} E(\mathbf{x}, g(\boldsymbol{\alpha}); \boldsymbol{I}) \\
&\geq \min_{\mathbf{x} \in \mathcal{L}^{|\mathcal{V}|}} \left\{ \sum_{p \in \mathcal{V}} \min_{\boldsymbol{\alpha} \in H_i} F^p\left(\boldsymbol{I}, \boldsymbol{g}(\boldsymbol{\alpha})\right) \cdot x_p + \sum_{p \in \mathcal{V}} \min_{\boldsymbol{\alpha} \in H_i} B^p\left(\boldsymbol{I}, \boldsymbol{g}(\boldsymbol{\alpha})\right) \cdot (1 - x_p) \right. \\
&\qquad \left. + \sum_{(p,q) \in \mathcal{E}} P^{pq}\left(\boldsymbol{I}\right) \cdot \left| x_p - x_q \right| \right\} \qquad (4.29) \\
&\geq \min_{\mathbf{x} \in \mathcal{L}^{|\mathcal{V}|}} \left\{ \sum_{p \in \mathcal{V}} F^p\left(\boldsymbol{I}, \boldsymbol{g}^{\max}(H_i)\right) \cdot x_p + \sum_{p \in \mathcal{V}} B^p\left(\boldsymbol{I}, \boldsymbol{g}^{\min}(H_i)\right) \cdot (1 - x_p) \right. \\
&\qquad \left. + \sum_{(p,q) \in \mathcal{E}} P^{pq}\left(\boldsymbol{I}\right) \cdot \left| x_p - x_q \right| \right\} \qquad (4.30) \\
&:= L(H_i; \boldsymbol{I})
\end{aligned}$$

The inequality in Eq. (4.29) is Jensen's inequality for the minimum operation. The inequality in Eq. (4.30) was derived from the definition of the energy terms in Eqs. (4.25) and (4.26), as well as the fact that $h_p^F(\mathbf{y})$ and $h_p^B(\mathbf{y})$ satisfy the conditions in Eqs. (4.27) and (4.28), respectively. I added the proof in Appendix C.2. A potential choice of $h_p^F(\mathbf{y})$ and $h_p^B(\mathbf{y})$ is a penalty based on a distance function whose value is proportional to the distance from the boundary of $\mathbf{y}$, which was proposed by Boykov and Funka-Lea [18]:

$$h_p^F(\mathbf{y}) = D(p, \Omega) \tag{4.31}$$

$$h_p^B(\mathbf{y}) = D(p, \overline{\Omega}) \tag{4.32}$$

where $\Omega = \{p \in \mathcal{V} | y_p = 1\}$ is the region of the shape $\mathbf{y}$, and $D(p, \Omega) = d(p, q)$ ($D(p, \Omega), d(p, q) \geq 0$) is the distance from the point p to the region Ω. Figure 4.16 shows an example of $h_p^F(\mathbf{y})$ and $h_p^B(\mathbf{y})$ based on the Euclidean distance function. Note that we can use an arbitrary distance measure, or a norm of $\vec{pq}$, as $d(p, q)$. In addition, it is possible to extend it to any monotonically increasing function of the distance measure. Such a transformation may be a reasonable choice of shape constraint because the shape priors have less influence on voxels near the boundary, which may reduce the risk of errors in the shape prior at the cost of further computation for the distance transform.

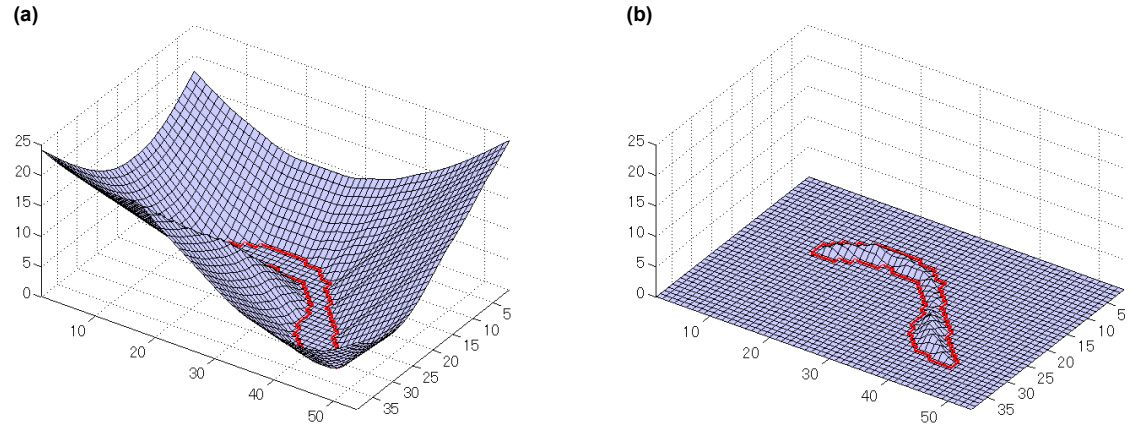

Fig. 4.16 A 2D example of the penalty functions (a) $h_p^F(\mathbf{y})$ and (b) $h_p^B(\mathbf{y})$ based on the Euclidean distance function. The red contour shows the contour of the shape prior $\mathbf{y}$.

4.5 Conclusions

In this study, I proposed an algorithm that simultaneously optimizes an energy functional for segmentation as well as the shape priors used for segmentation. The proposed joint-optimization algorithm can efficiently find an optimal shape prior from among all possible shape priors generated from an SSM by conducting a branch-and-bound search in the eigenshape space. In contrast to the conventional method [25], the proposed algorithm does not require the clustering of predefined shape templates or a search tree with all shapes. I demonstrated the effectiveness of the proposed algorithm for pancreas and spleen segmentation using multiphase CT volumes that were scanned based on a two-fold cross-validation. The results are summarized as follows.

1. Compared with the conventional method described by Lempitsky et al. [25], the proposed algorithm improves the pancreas- and spleen-segmentation accuracy (Jaccard index; JI) from 61.0 ± 21.3 % and 89.5 ± 8.4 % to 62.3 ± 19.5 % and 90.0 ± 8.2 %, with a statistically significant difference of $p < 0.05$ and $p < 0.01$, respectively. There was also a highly significant difference in the performance compared with pancreas and spleen graph-cut segmentation without shape priors, i.e., 58.6 ± 16.1 % and 82.8 ± 19.8 % with $p < 0.01$ and $p < 0.01$, respectively.

2. The average number of nodes traversed during pancreas and spleen segmentation was increased from 17.77 to 6.558×10^3 and from 13.65 to 7.456×10^3, respectively, because of the difference in the number of shape priors searched, i.e., 49 with the conventional method and 6.863×10^9 and 4.194×10^{10} with the proposed method. Although the proposed algorithm is relatively slow in practice because many more shapes are searched, after normalizing the number of nodes traversed using the number of shapes searched, I found that my algorithm was 3.80×10^5 and 1.57×10^6 times more efficient than the conventional method for pancreas and spleen segmentation, respectively.

3. I found that the proposed method was comparable with the state-of-the-art multi-organ-segmentation algorithm [52] based on the study performed using the same test dataset.

4. The proposed voxel-selection operator used to search for an optimal solution successfully balanced the tree and reduced the depth of the optimal solution, thereby decreasing the computational time needed.

5. A limitation of the proposed algorithm is the inconsistency between the JI of the segmentation and the energy functional that needs to be minimized, which degrades the JI despite the lower energy.

6. I showed the good extensibility of my framework in terms of the SSM and energy functional. Possible examples of the SSM are the level-set function, LogOdds, and Label Space learnt via a PCA or an ICA. Another way of incorporating the shape prior into the energy functional is via a distance function.

Further improvements to the proposed algorithm include the following.

(a) Despite its good performance in terms of the normalized number of nodes traversed, the actual number of nodes searched is not small, i.e., 6.558×10^3 for

pancreas segmentation and 7.456×10^3 for spleen segmentation; thus, further reducing the number of nodes is an important area that needs to be addressed.

(b) It would be useful to modify the proposed algorithm for application to a different SSM based on other shape representations such as PDM [63], label space [13], or LogOdds [38], and that based on non-linear statistical analysis.

(c) I plan to improve the segmentation performance from the perspective of the SSM and energy functional. I also plan to extend the proposed algorithm to deal with other objective functions, such as those containing a multishape term [21], gradient-based shape term (cf. Section 3.2.5), Parzen-window-method-based shape term [39], and the functions used by Chen et al. [85], Xiang et al. [24], and Besbes et al. [22].

(d) To overcome the inconsistency between the JI and the energy, I will determine the optimal design of an energy functional by referring to Scharstein and Pal [84] and Komodakis et al. [86].

(e) I will aim to realize further improvements in the computational efficacy of the proposed algorithm for using an SSM with a higher number of dimensions.

Chapter 5

Summary, conclusions, and future works

5.1 Summary

The goal of this study was to provide innovative solutions for the issues related to abdominal organ segmentation using a statistical shape model (SSM). The first main contribution of the study is that it provides modelling and segmentation methods for postmortem CT (PMCT) volumes, which is the first computer-aided diagnosis using autopsy imaging (Ai). The proposed method is innovative not only in its application but also in its novel methodology for performing the statistical shape analysis of a limited number of label volumes with large variations in shape. A second important contribution of this thesis is that it provides a globally optimal solution for the objective functional of the segmentation considering all possible shapes generated by the SSM. The significance of this method is that the solution is guaranteed to be globally optimal.

In Chapter 2, an SSM of a postmortem liver was developed. First, it was revealed that the performance of the SSM constructed using *in vivo* liver labels suffers when describing postmortem liver shapes, and a larger number of training labels are required to improve the performance of the SSM. Then, the performance of the conventional SSMs was found to be improved by using both postmortem liver shape labels and artificial shape labels synthesized from *in vivo* liver shape labels.

Chapter 3 described the liver segmentation based on postmortem CT images using the SSM proposed in Chapter 2. The SSMs using the synthesized labels also improved the accuracy of segmentation. The results of a comparative study showed

that the translation in the feature space of the level set was the best method for simulating postmortem changes in the liver. The segmentation algorithm using the SSM based on translation achieved an average Jaccard index (JI) of 0.806, which was the highest among the eight SSMs.

Chapter 4 provided a solution to optimize the energy across all shapes in the SSM, as well as the segmentation labels in a graph cut segmentation. In contrast to the conventional methods that are based on a motivation similar to that of my study [22–24], my method can obtain a globally optimal solution in terms of the graph cut energy functional. The proposed method outperformed the conventional method [25] in terms of its higher segmentation accuracy, as well as higher computational efficiency. As compared to the method in [25], the proposed method improved the accuracy of pancreas and spleen segmentation in terms of the JI from 61.0 ± 21.3 % and 89.5 ± 8.4 % to 62.3 ± 19.5, % and 90.0 ± 8.2 %, with a statistically significant difference. The proposed method was 3.80×10^5 and 1.57×10^6 times more efficient than the conventional method [25] for pancreas and spleen segmentation, respectively.

5.2 Conclusions and future works

To conclude, in my opinion this study significantly influences the history of SSM-based abdominal organ segmentation from two different aspects: (i) liver segmentation for PMCT volumes, and (ii) joint optimization of the segmentation and shape prior generated by an SSM. In the following, I would like present concluding remarks and the work to be performed in the future.

The proposed SSM-based postmortem liver segmentation algorithm is the first application of CAD for Ai. I am sure that this will open new doors for developing Ai-CAD systems. However, further improvement is needed in the performance of the proposed liver segmentation algorithm, which is still inferior to that for *in vivo* CT images [1, 49, 50] because of postmortem deformation. In the future, I would like introduce another transformation method that simulates the changes after the death, such as the finite element method (FEM)-based transformations. In addition, it is important to develop a statistical model for the postmortem changes in CT values. I also plan to improve the segmentation process by incorporating Ai-specific knowledge.

The joint optimization of the segmentation and shape prior generated by an SSM constitutes another innovative contribution to the SSM-based segmentation

algorithm. This is the first study to provide a globally optimal solution for the energy across all shapes in the SSM, as well as the segmentation labels, and my method showed higher segmentation accuracy and higher computational efficiency. The limitation of my method lies in the inconsistency between the JI and energy, which is a potential problem for all optimization-based segmentation algorithms. In the future, I would like to investigate the optimal design of an energy functional, which has been addressed by a few authors, e.g., Scharstein and Pal [84]. The proposed method is efficient but the computational cost is still high, which constitutes another drawback of the method. Therefore, a method to improve the computational efficacy constitutes another important future study.

References

[1] A. Shimizu, R. Ohno, T. Ikegami, H. Kobatake, S. Nawano, and D. Smutek, "Segmentation of multiple organs in non-contrast 3D abdominal CT images," *International Journal of Computer Assisted Radiology and Surgery*, vol. 2, no. 3-4, pp. 135–142, 2007.

[2] M. Kass, A. Witkin, and D. Terzopoulos, "Snakes: Active contour models," *International Journal of Computer Vision*, vol. 1, no. 4, pp. 321–331, 1988.

[3] H. Delingette, "Simplex meshes: a general representation for 3D shape reconstruction," in *Computer Vision and Pattern Recognition, 1994. Proceedings CVPR'94., 1994 IEEE Computer Society Conference on*, 1994, pp. 856–859.

[4] T. F. Cootes, C. J. Taylor, D. H. Cooper, and J. Graham, "Active shape models-their training and application," *Computer Vision and Image Understanding*, vol. 61, no. 1, pp. 38–59, 1995.

[5] S. M. Pizer, P. T. Fletcher, S. Joshi, A. Thall, J. Z. Chen, Y. Fridman, D. S. Fritsch, A. G. Gash, J. M. Glotzer, M. R. Jiroutek *et al.*, "Deformable m-reps for 3D medical image segmentation," *International Journal of Computer Vision*, vol. 55, no. 2-3, pp. 85–106, 2003.

[6] M. Styner, I. Oguz, S. Xu, C. Brechbühler, D. Pantazis, J. J. Levitt, M. E. Shenton, and G. Gerig, "Framework for the statistical shape analysis of brain structures using spharm-pdm," *The Insight Journal*, no. 1071, p. 242, 2006.

[7] D. Rueckert, A. F. Frangi, and J. A. Schnabel, "Automatic construction of 3-D statistical deformation models of the brain using nonrigid registration," *Medical Imaging, IEEE Transactions on*, vol. 22, no. 8, pp. 1014–1025, 2003.

[8] S. Durrleman, "Statistical models of currents for measuring the variability of anatomical curves, surfaces and their evolution," Ph.D. dissertation, Nice, 2010.

[9] M. E. Leventon, W. E. L. Grimson, and O. Faugeras, "Statistical shape influence in geodesic active contours," in *Computer Vision and Pattern Recognition, 2000. Proceedings. IEEE Conference on*, vol. 1, 2000, pp. 316–323.

[10] A. Tsai, W. Wells, C. Tempany, E. Grimson, and A. Willsky, "Mutual information in coupled multi-shape model for medical image segmentation," *Medical Image Analysis*, vol. 8, no. 4, pp. 429–445, 2004.

[11] J. Yang, L. H. Staib, and J. S. Duncan, "Neighbor-constrained segmentation with level set based 3-d deformable models," *Medical Imaging, IEEE Transactions on*, vol. 23, no. 8, pp. 940–948, 2004.

[12] K. M. Pohl, J. Fisher, M. Shenton, R. W. McCarley, W. E. L. Grimson, R. Kikinis, and W. M. Wells, "Logarithm odds maps for shape representation," in *Medical Image Computing and Computer-Assisted Intervention–MICCAI 2006*. Springer, 2006, pp. 955–963.

[13] J. Malcolm, Y. Rathi, M. E. Shenton, and A. Tannenbaum, "Label space: A coupled multi-shape representation," in *Medical Image Computing and Computer-Assisted Intervention–MICCAI 2008*. Springer, 2008, pp. 416–424.

[14] N. Changizi and G. Hamarneh, "Probabilistic multi-shape representation using an isometric log-ratio mapping," in *Medical Image Computing and Computer-Assisted Intervention–MICCAI 2010*. Springer, 2010, pp. 563–570.

[15] T. Okada, M. G. Linguraru, Y. Yoshida, M. Hori, R. M. Summers, Y.-W. Chen, N. Tomiyama, and Y. Sato, "Abdominal multi-organ segmentation of CT images based on hierarchical spatial modeling of organ interrelations," in *Abdominal Imaging. Computational and Clinical Applications*. Springer, 2012, pp. 173–180.

[16] A. Saito, M. Nakada, E. Oost, A. Shimizu, H. Watanabe, and S. Nawano, "A statistical shape model for multiple organs based on synthesized-based learning," in *Abdominal Imaging. Computation and Clinical Applications*. Springer, 2013, pp. 280–289.

[17] D. Cremers, M. Rousson, and R. Deriche, "A review of statistical approaches to level set segmentation: integrating color, texture, motion and shape," *International Journal of Computer Vision*, vol. 72, no. 2, pp. 195–215, 2007.

[18] Y. Boykov and G. Funka-Lea, "Graph cuts and efficient ND image segmentation," *International Journal of Computer Vision*, vol. 70, no. 2, pp. 109–131, 2006.

[19] D. Grosgeorge, C. Petitjean, J.-N. Dacher, and S. Ruan, "Graph cut segmentation with a statistical shape model in cardiac MRI," *Computer Vision and Image Understanding*, vol. 117, no. 9, pp. 1027–1035, 2013.

[20] J. Malcolm, Y. Rathi, and A. Tannenbaum, "Graph cut segmentation with nonlinear shape priors," in *Image Processing, 2007. ICIP 2007. IEEE International Conference on*, vol. 4, 2007, pp. IV–365.

[21] K. Nakagomi, A. Shimizu, H. Kobatake, M. Yakami, K. Fujimoto, and K. Togashi, "Multi-shape graph cuts with neighbor prior constraints and its application to lung segmentation from a chest CT volume," *Medical Image Analysis*, vol. 17, no. 1, pp. 62–77, 2013.

[22] A. Besbes, N. Komodakis, G. Langs, and N. Paragios, "Shape priors and discrete MRFs for knowledge-based segmentation," in *Computer Vision and Pattern Recognition, 2009. CVPR 2009. IEEE Conference on*, 2009, pp. 1295–1302.

[23] X. Chen, J. K. Udupa, U. Bagci, Y. Zhuge, and J. Yao, "Medical image segmentation by combining graph cuts and oriented active appearance models," *Image Processing, IEEE Transactions on*, vol. 21, no. 4, pp. 2035–2046, 2012.

[24] B. Xiang, J.-F. Deux, A. Rahmouni, and N. Paragios, "Joint model-pixel segmentation with pose-invariant deformable graph-priors," in *Medical Image Computing and Computer-Assisted Intervention–MICCAI 2013*. Springer, 2013, pp. 267–274.

[25] V. Lempitsky, A. Blake, and C. Rother, "Branch-and-mincut: global optimization for image segmentation with high-level priors," *Journal of Mathematical Imaging and Vision*, vol. 44, no. 3, pp. 315–329, 2012.

[26] M. J. Thali, K. Yen, W. Schweitzer, P. Vock, C. Boesch, C. Ozdoba, G. Schroth, M. Ith, M. Sonnenschein, T. Doernhoefer *et al.*, "Virtopsy, a new imaging horizon in forensic pathology: virtual autopsy by postmortem multislice computed tomography (msct) and magnetic resonance imaging (MRI)–a feasibility study." *Journal of Forensic Sciences*, vol. 48, no. 2, pp. 386–403, 2003.

[27] F. Dedouit, N. Telmon, C. Guilbeau-Frugier, D. Gainza, P. Otal, F. Joffre, and D. Rougé, "Virtual autopsy and forensic identification–practical application: a report of one case," *Journal of Forensic Sciences*, vol. 52, no. 4, pp. 960–964, 2007.

[28] L. Oesterhelweg, M. Lorenzen, C. Braun, D. Rohwedder, G. Adam, and K. Püschel, "Radio-autopsy–CT-assisted reconstruction in an case of extended suicide," *Rechtsmedizin*, vol. 17, no. 1, pp. 44–47, 2007.

[29] H. Ezawa, R. Yoneyama, S. Kandatsu, K. Yoshikawa, H. Tsujii, and K. Harigaya, "Introduction of autopsy imaging redefines the concept of autopsy: 37 cases of clinical experience," *Pathology International*, vol. 53, no. 12, pp. 865–873, 2003.

[30] H. Ezawa, S. Shiotani, and S. Uchigasaki, "Autopsy imaging in japan," *Rechtsmedizin*, vol. 17, no. 1, pp. 19–20, 2007.

[31] T. Heimann and H.-P. Meinzer, "Statistical shape models for 3D medical image segmentation: A review," *Medical Image Analysis*, vol. 13, no. 4, pp. 543–563, 2009.

[32] D. Kainmüller, T. Lange, and H. Lamecker, "Shape constrained automatic segmentation of the liver based on a heuristic intensity model," in *Proc. MICCAI Workshop 3D Segmentation in the Clinic: A Grand Challenge*, 2007, pp. 109–116.

[33] T. Okada, R. Shimada, M. Hori, M. Nakamoto, Y.-W. Chen, H. Nakamura, and Y. Sato, "Automated segmentation of the liver from 3D CT images using probabilistic atlas and multilevel statistical shape model," *Academic Radiology*, vol. 15, no. 11, pp. 1390–1403, 2008.

[34] M. De Bruijne, M. T. Lund, L. B. Tankó, P. C. Pettersen, and M. Nielsen, "Quantitative vertebral morphometry using neighbor-conditional shape models," *Medical Image Analysis*, vol. 11, no. 5, pp. 503–512, 2007.

[35] N. Baka, M. de Bruijne, J. H. Reiber, W. Niessen, and B. P. Lelieveldt, "Confidence of model based shape reconstruction from sparse data," in *Biomedical Imaging: From Nano to Macro, 2010 IEEE International Symposium on*, 2010, pp. 1077–1080.

[36] E. Syrkina, R. Blanc, and G. Székely, "Propagating uncertainties in statistical model based shape prediction," in *SPIE Medical Imaging*, 2011, pp. 796 240–796 240.

[37] S. Tomoshige, E. Oost, A. Shimizu, H. Watanabe, H. Kobatake, and S. Nawano, "Relaxed conditional statistical shape models and their application to non-contrast liver segmentation," in *Abdominal Imaging. Computational and Clinical Applications*. Springer, 2012, pp. 126–136.

[38] K. M. Pohl, J. Fisher, S. Bouix, M. Shenton, R. W. McCarley, W. E. L. Grimson, R. Kikinis, and W. M. Wells, "Using the logarithm of odds to define a vector space on probabilistic atlases," *Medical Image Analysis*, vol. 11, no. 5, pp. 465–477, 2007.

[39] M. G. Linguraru, J. A. Pura, V. Pamulapati, and R. M. Summers, "Statistical 4D graphs for multi-organ abdominal segmentation from multiphase CT," *Medical Image Analysis*, vol. 16, no. 4, pp. 904–914, 2012.

[40] H. Murase and S. K. Nayar, "Learning by a generation approach to appearance-based object recognition," in *Pattern Recognition, 1996., Proceedings of the 13th International Conference on*, vol. 1, 1996, pp. 24–29.

[41] D. M. Gavrila and J. Giebel, "Virtual sample generation for template-based shape matching," in *Computer Vision and Pattern Recognition, 2001. CVPR 2001. Proceedings of the 2001 IEEE Computer Society Conference on*, vol. 1, 2001, pp. I–676.

[42] H. Ishida, T. Takahashi, I. Ichiro, Y. Mekada, and H. Murase, "Generation of training data by degradation models for traffic sign symbol recognition," *IEICE Rransactions on Information and Systems*, vol. 90, no. 8, pp. 1134–1141, 2007.

[43] Y. Uchida, A. Shimizu, H. Kobatake, S. Nawano, and K. Shinozaki, "A comparative study of statistical shape models of the pancreas," *International Journal of Computer Assisted Radiology and Surgery*, vol. 5, no. 1, pp. S385–S387, 2010.

[44] J.-Y. Jeong, "Estimation of probability distribution on multiple anatomical objects and evaluation of statistical shape models," Ph.D. dissertation, University of North Carolina, Chapel Hill, NC, USA, 2009.

[45] M. A. Styner, K. T. Rajamani, L.-P. Nolte, G. Zsemlye, G. Székely, C. J. Taylor, and R. H. Davies, "Evaluation of 3d correspondence methods for model building," in *Information Processing in Medical Imaging*, 2003, pp. 63–75.

[46] J. C. Lagarias, J. A. Reeds, M. H. Wright, and P. E. Wright, "Convergence properties of the nelder–mead simplex method in low dimensions," *SIAM Journal on Optimization*, vol. 9, no. 1, pp. 112–147, 1998.

[47] A. Shimizu, K. Nakagomi, T. Narihira, H. Kobatake, S. Nawano, K. Shinozaki, K. Ishizu, and K. Togashi, "Automated segmentation of 3D CT images based on statistical atlas and graph cuts," in *Medical Computer Vision. Recognition Techniques and Applications in Medical Imaging*. Springer, 2011, pp. 214–223.

[48] Y. Boykov, O. Veksler, and R. Zabih, "Fast approximate energy minimization via graph cuts," *Pattern Analysis and Machine Intelligence, IEEE Transactions on*, vol. 23, no. 11, pp. 1222–1239, 2001.

[49] A. Shimizu, T. Kimoto, H. Kobatake, S. Nawano, and K. Shinozaki, "Automated pancreas segmentation from three-dimensional contrast-enhanced computed tomography," *International Journal of Computer Assisted Radiology and Surgery*, vol. 5, no. 1, pp. 85–98, 2010.

[50] H. Lamecker, T. Lange, and M. Seebass, "Segmentation of the liver using a 3D statistical shape model," Zuse Institute, Berlin., Tech. Rep., Apr. 2004.

[51] R. Wolz, C. Chu, K. Misawa, M. Fujiwara, K. Mori, and D. Rueckert, "Automated abdominal multi-organ segmentation with subject-specific atlas generation," *Medical Imaging, IEEE Transactions on*, vol. 32, no. 9, pp. 1723–1730, Sept 2013.

[52] T. Okada, M. G. Linguraru, M. Hori, R. M. Summers, N. Tomiyama, and Y. Sato, "Abdominal multi-organ segmentation from ct images using conditional shape–location and unsupervised intensity priors," *Medical Image Analysis*, vol. 26, no. 1, pp. 1–18, 2015.

[53] T. Kitasaka, M. Sakashita, K. Mori, Y. Suenaga, and S. Nawano, "A method for extracting pancreas regions from four-phase contrasted 3D abdominal CT images," *Int J Comput Assist Radiol Surg*, vol. 3, no. Suppl 1, p. S40, 2008.

[54] M. Erdt, M. Kirschner, K. Drechsler, S. Wesarg, M. Hammon, and A. Cavallaro, "Automatic pancreas segmentation in contrast enhanced CT data using learned spatial anatomy and texture descriptors," in *IEEE International Symposium on Biomedical Imaging*, 2011, pp. 2076–2082.

[55] A. Farag, L. Lu, E. Turkbey, J. Liu, and R. M. Summers, "A bottom-up approach for automatic pancreas segmentation in abdominal CT scans," in *Abdominal Imaging. Computational and Clinical Applications*. Springer, 2014, vol. 8676, pp. 103–113.

[56] H. R. Roth, L. Lu, A. Farag, H.-C. Shin, J. Liu, E. B. Turkbey, and R. M. Summers, "Deeporgan: Multi-level deep convolutional networks for automated pancreas segmentation," in *Medical Image Computing and Computer-Assisted Intervention–MICCAI 2015*. Springer, 2015, pp. 556–564.

[57] K. Karasawa, M. Oda, Y. Hayashi, Y. Nimura, T. Kitasaka, K. Misawa, M. Fujiwara, D. Rueckert, and K. Mori, "Pancreas segmentation from 3D abdominal CT images using patient-specific weighted subspatial probabilistic atlases," in *SPIE Medical Imaging*, vol. 9413, 2015, p. 94131A.

[58] G. Slabaugh and G. Unal, "Graph cuts segmentation using an elliptical shape prior," in *IEEE International Conference on Image Processing*, vol. 2, Sept 2005, pp. II–1222–5.

[59] G. Funka-Lea, Y. Boykov, C. Florin, M.-P. Jolly, R. Moreau-Gobard, R. Ramaraj, and D. Rinck, "Automatic heart isolation for CT coronary visualization using graph-cuts," in *Biomedical Imaging: Nano to Macro, 2006. 3rd IEEE International Symposium on*, 2006, pp. 614–617.

[60] P. Das, O. Veksler, V. Zavadsky, and Y. Boykov, "Semiautomatic segmentation with compact shape prior," *Image and Vision Computing*, vol. 27, no. 1, pp. 206–219, 2009.

[61] D. Freedman and T. Zhang, "Interactive graph cut based segmentation with shape priors," in *IEEE Computer Society Conference on Computer Vision and Pattern Recognition*, vol. 1, 2005, pp. 755–762.

[62] P. Kohli, J. Rihan, M. Bray, and P. H. Torr, "Simultaneous segmentation and pose estimation of humans using dynamic graph cuts," *International Journal of Computer Vision*, vol. 79, no. 3, pp. 285–298, 2008.

[63] T. F. Cootes, G. J. Edwards, and C. J. Taylor, "Active appearance models," *Pattern Analysis and Machine Intelligence, IEEE Transactions on*, vol. 23, no. 6, pp. 681–685, 2001.

[64] D. Skočaj, A. Leonardis, and H. Bischof, "Weighted and robust learning of subspace representations," *Pattern Recognition*, vol. 40, no. 5, pp. 1556–1569, 2007.

[65] J. Clausen, "Branch and bound algorithms-principles and examples," *Department of Computer Science, University of Copenhagen*, pp. 1–30, 1999.

[66] R. J. Vanderbei, *Linear programming*. Springer, 1998.

[67] P. Kohli and P. H. Torr, "Dynamic graph cuts for efficient inference in markov random fields," *Pattern Analysis and Machine Intelligence, IEEE Transactions on*, vol. 29, no. 12, pp. 2079–2088, 2007.

[68] G. Navarro, R. Baeza-Yates, E. F. Barbosa, N. Ziviani, and W. Cunto, "Binary searching with nonuniform costs and its application to text retrieval," *Algorithmica*, vol. 27, no. 2, pp. 145–169, 2000.

[69] M. Fornefett, K. Rohr, R. Sprengel, and H. S. Stiehl, "Elastic medical image registration using orientation attributes at landmarks," in *Proc. Medical Image Understanding and Analysis*, 1998, pp. 49–52.

[70] S. R. Finch, *Mathematical constants*. Cambridge University Press, 2003.

[71] C. Chu, M. Oda, T. Kitasaka, K. Misawa, M. Fujiwara, Y. Hayashi, Y. Nimura, D. Rueckert, and K. Mori, "Multi-organ segmentation based on spatially-divided probabilistic atlas from 3D abdominal CT images," in *Medical Image Computing and Computer-Assisted Intervention*. Springer, 2013, pp. 165–172.

[72] T. Okada, M. G. Linguraru, M. Hori, R. M. Summers, N. Tomiyama, and Y. Sato, "Abdominal multi-organ CT segmentation using organ correlation graph and prediction-based shape and location priors," in *Medical Image Computing and Computer-Assisted Intervention*. Springer, 2013, pp. 275–282.

[73] M. G. Linguraru, J. K. Sandberg, Z. Li, F. Shah, and R. M. Summers, "Automated segmentation and quantification of liver and spleen from CT images using normalized probabilistic atlases and enhancement estimation," *Medical Physics*, vol. 37, no. 2, pp. 771–783, 2010.

[74] A. M. Mharib, A. R. Ramli, S. Mashohor, and R. B. Mahmood, "Survey on liver ct image segmentation methods," *Artificial Intelligence Review*, vol. 37, no. 2, pp. 83–95, 2012.

[75] S. Ghose, A. Oliver, R. Martí, X. Lladó, J. C. Vilanova, J. Freixenet, J. Mitra, D. Sidibé, and F. Meriaudeau, "A survey of prostate segmentation methodologies in ultrasound, magnetic resonance and computed tomography images," *Computer methods and programs in biomedicine*, vol. 108, no. 1, pp. 262–287, 2012.

[76] J. E. Iglesias and M. R. Sabuncu, "Multi-atlas segmentation of biomedical images: A survey," *Medical Image Analysis*, vol. 24, no. 1, pp. 205 – 219, 2015.

[77] S. Tomoshige, E. Oost, A. Shimizu, H. Watanabe, and S. Nawano, "A conditional statistical shape model with integrated error estimation of the conditions; application to liver segmentation in non-contrast ct images," *Medical Image Analysis*, vol. 18, no. 1, pp. 130–143, 2014.

[78] G. Li, X. Chen, F. Shi, W. Zhu, J. Tian, and D. Xiang, "Automatic liver segmentation based on shape constraints and deformable graph cut in ct images," *Image Processing, IEEE Transactions on*, vol. 24, no. 12, pp. 5315–5329, 2015.

[79] G. Litjens, R. Toth, W. van de Ven, C. Hoeks, S. Kerkstra, B. van Ginneken, G. Vincent, G. Guillard, N. Birbeck, J. Zhang *et al.*, "Evaluation of prostate segmentation algorithms for mri: the promise12 challenge," *Medical Image Analysis*, vol. 18, no. 2, pp. 359–373, 2014.

[80] Y. Shao, Y. Gao, Q. Wang, X. Yang, and D. Shen, "Locally-constrained boundary regression for segmentation of prostate and rectum in the planning ct images," *Medical Image Analysis*, 2015.

[81] O. Gloger, K. D. Tönnies, V. Liebscher, B. Kugelmann, R. Laqua, and H. Völzke, "Prior shape level set segmentation on multistep generated probability maps of mr datasets for fully automatic kidney parenchyma volumetry," *Medical Imaging, IEEE Transactions on*, vol. 31, no. 2, pp. 312–325, 2012.

[82] A. K. Rudra, A. S. Chowdhury, A. Elnakib, F. Khalifa, A. Soliman, G. Beache, and A. El-Baz, "Kidney segmentation using graph cuts and pixel connectivity," *Pattern Recognition Letters*, vol. 34, no. 13, pp. 1470–1475, 2013.

[83] D. Defays, "An efficient algorithm for a complete link method," *The Computer Journal*, vol. 20, no. 4, pp. 364–366, 1977.

[84] D. Scharstein and C. Pal, "Learning conditional random fields for stereo," in *Computer Vision and Pattern Recognition, 2007. CVPR'07. IEEE Conference on*, 2007, pp. 1–8.

[85] X. Chen, J. K. Udupa, A. Alavi, and D. A. Torigian, "Gc-asm: Synergistic integration of graph-cut and active shape model strategies for medical image segmentation," *Computer Vision and Image Understanding*, vol. 117, no. 5, pp. 513–524, 2013.

[86] N. Komodakis, B. Xiang, and N. Paragios, "A framework for efficient structured max-margin learning of high-order mrf models," *Pattern Analysis and Machine Intelligence, IEEE Transactions on*, vol. 37, no. 7, pp. 1425–1441, July 2015.

[87] W. H. Press, S. A. Teukolsky, W. T. Vetterling, and B. P. Flannery, *Numerical Recipes 3rd Edition: The Art of Scientific Computing*, 3rd ed. New York, NY, USA: Cambridge University Press, 2007.

Appendix A

EM algorithm

Let D be a set of observation data and Z be set of latent variables of D that cannot be observed directly. I denote by D *incomplete data* and by (D, Z) a set of *complete data*. Given a probability distribution of the complete data $p(D, Z; \theta)$, where θ is an unknown parameter, the log likelihood function for the incomplete data is defined as A.1:

$$\begin{aligned} \mathcal{L}(\theta; D) &= \log p(D; \theta) \\ &= \log \sum_{Z} p(D, Z; \theta) \end{aligned} \tag{A.1}$$

The maximum likelihood estimate $\hat{\theta}$ of unknown parameters θ under the given incomplete data D can be defined as the parameters that maximize the log likelihood function $\mathcal{L}$:

$$\hat{\theta} = \arg\max_{\theta} \mathcal{L}(\theta; D) \tag{A.2}$$

Because (A.2) is classified as a nonlinear optimization problem that cannot be computed analytically, an efficient approximation algorithm or expectation-maximization (EM) algorithm is employed.

A.1 Maximization of the log likelihood function of the complete data

Instead of solving the Eq. (A.2) directly, the EM algorithm maximizes the conditional expectation value of the log likelihood function of the complete data. In particular,

the maximum likelihood estimate is computed by an iterative method having two steps.

First, for a given parameter estimation $\theta^{(t)}$ at the t-th iteration, the conditional expectation value of the log likelihood function of the complete data $\log P(D, Z; \theta)$ is computed (E-step):

$$\begin{aligned} \mathcal{Q}(\theta \,|\, \theta^{(t)}) &= E\left(\log P(D, Z; \theta) \,|\, D\,;\, \theta^{(t)} \right) \\ &= \sum_{Z} P(Z|D\,;\theta^{(t)})\, \log P(D, Z; \theta) \end{aligned} \tag{A.3}$$

where $E(A|B)$ is an expectation value of A for a given condition B. $P(Z|D\,;\theta^{(t)})$ is a posterior probability of Z for a given D, which is calculated by Eq. (A.4) based on a Bayes' theorem.

$$P(Z|D\,;\theta^{(t)}) = \frac{P(D, Z; \theta^{(t)})}{\sum_{Z} P(D, Z; \theta^{(t)})} \tag{A.4}$$

Then, θ that maximizes $\mathcal{Q}$ is used for the $(t+1)$-th estimation of the parameter (M-step). These two steps are iterated until the convergence condition is met.

A.2 Extension of the EM algorithm [1]

Shimizu et al. [1] proposed an EM algorithm for the extended-mixture Gaussian distribution in which the mixture ratio is defined. This model allows us to estimate parameters considering the location information.

$$P(v \,|\, \theta) = \frac{1}{N} \sum_{l=1}^{M} \sum_{n=1}^{N} \alpha_l(n)\, \mathcal{N}(v\,; \mu_l, \Sigma_l) \tag{A.5}$$

Here, M is a number of classes, N is a number of voxels, $\alpha_l(n)$ is a mixture ratio for the l-th class at the n-th voxel, and μ_l and Σ_l are the mean and the covariance for the l-th class. The unknown variables to be estimated are $\theta = \{\alpha_l(n), \mu_l, \Sigma_l\}$. Given an incomplete dataset $D = \{v_n\,; n = 1, 2, \cdots, N\}$, latent variables z_n correspond to v_n indicating from which distribution of the class v_n is generated. Taking account of the fact that the joint distribution of v_n and z_n can be written as $P(v_n, z_n\,; \theta) = \alpha_l(n)\, \mathcal{N}(v_n\,; \mu_l, \Sigma_l)$, $\mathcal{Q}$ the function in the E-step of the EM algorithm is formulated as

$$\mathcal{Q}(\theta \,|\, \theta^{(t)}) = \sum_{l=1}^{M} \sum_{n=1}^{N} P(l \,|\, x_n\,; \theta^{(t)})\, \log \{\alpha_l(n)\, \mathcal{N}(v\,; \mu_l, \Sigma_l)\} \tag{A.6}$$

where, $P(l \mid x_n ; \theta^{(t)})$ is calculated by Eq. (A.7) based on the Bayes' theorem:

$$P(l \mid x_n ; \theta^{(t)}) = \frac{P(v_n, l \mid \theta^{(t)})}{\sum_l P(v_n, l \mid \theta^{(t)})} = \frac{\mathcal{N}(v_n;\, l, \theta^{(t)})\, \alpha_l^{(t)}(n)}{\sum_l \mathcal{N}(v_n;\, l, \theta^{(t)})\, \alpha_l^{(t)}(n)} \tag{A.7}$$

where

$$\mathcal{N}(v_n;\, l, \theta^{(t)}) = \frac{1}{\sqrt{(2\pi)^d\, |\Sigma_l|}} \exp\left\{ -\frac{1}{2} (v_n - \mu_l)^\top \Sigma_l^{-1} (v_n - \mu_l) \right\} \tag{A.8}$$

In the M-step, $\dfrac{\partial \mathcal{Q}(\theta \mid \theta^{(t)})}{\partial \mu_l} = 0$ and $\dfrac{\partial \mathcal{Q}(\theta \mid \theta^{(t)})}{\partial \Sigma_l^{-1}} = 0$ are solved by the following update function to maximize $\mathcal{Q}$ function for each parameter.

$$\mu_l^{(t+1)} = \frac{\sum_{n=1}^{N} v_n\, p(l \mid v_n, \theta^{(t)})}{\sum_{n=1}^{N} p(l \mid v_n, \theta^{(t)})} \tag{A.9}$$

$$\Sigma_l^{(t+1)} = \frac{\sum_{n=1}^{N} (v_n - \mu_l^{(t)})(v_n - \mu_l^{(t)})^\top\, p(l \mid v_n, \theta^{(t)})}{\sum_{n=1}^{N} p(l \mid v_n, \theta^{(t)})} \tag{A.10}$$

From the method of Lagrange multipliers, the mixture ratios are calculated by (A.11) solving the maximization problem of the $\mathcal{Q}$ function for $\alpha_l(n)$.

$$L = \mathcal{Q}(\theta \mid \theta^{(t)}) - \lambda \left(\sum_{l=1}^{M} \sum_{n=1}^{N} \alpha_l(n) - N \right) \tag{A.11}$$

$$\textit{subject to} \quad \sum_{l=1}^{M} \sum_{n=1}^{N} \alpha_l(n) = N$$

Here, λ is a Lagrange multiplier.

$$\frac{\partial L}{\partial \lambda} = \sum_{l=1}^{M} \sum_{n=1}^{N} \alpha_l(n) - N = 0 \quad \therefore \quad \sum_{l=1}^{M} \sum_{n=1}^{N} \alpha_l(n) = N \tag{A.12}$$

$$\frac{\partial L}{\partial \alpha_l(n)} = P(l|v_n\,;\theta^{(t)}) \cdot \frac{\mathcal{N}(v_n\,;\mu_l,\Sigma_l)}{\alpha_l(n)\,\mathcal{N}(v_n\,;\mu_l,\Sigma_l)} - \lambda = 0 \quad \therefore \;\; \alpha_l(n) = \frac{P(l|v_n\,;\theta^{(t)})}{\lambda} \tag{A.13}$$

From Eq. (A.13) and (A.12), we obtain $\lambda = 1$. By substituting this into Eq. (A.13), the update function of $\alpha_l(n)$ is obtained:

$$\alpha_l^{(t+1)}(n) = P(l|v_n\,;\theta^{(t)}) \tag{A.14}$$

Here, the posterior probability for $\mu_l^{(t+1)}$, $\Sigma_l^{(t+1)}$, and $\alpha_l^{(t+1)}(n)$ is obtained by Eq. (A.15).

$$P(l|v_n\,;\theta^{(t)}) = \frac{\mathcal{N}(v_n\,;\mu_l^{(t)},\Sigma_l^{(t)})\,\alpha_l^{(t)}(n)}{\sum_{l=1}^{M}\mathcal{N}(v_n\,;\mu_l^{(t)},\Sigma_l^{(t)})\,\alpha_l^{(t)}(n)} \tag{A.15}$$

When the initial variables have been assigned for $\mu_l^{(0)}$, $\Sigma_l^{(0)}$, and $\alpha_l^{(0)}(n)$, we obtain parameters that provide the local maximum of the likelihood function after the iteration.

Appendix B

Three properties required for the branch-and-bound optimization

The lower bound proposed in Section 4 possesses the three properties described below, which are crucial for the lower bound in a branch-and-bound algorithm.

B.1 Monotonicity

Corollary B.1.1. *For the nested domains of the shape parameter space $H_1 \subset H_0$, the inequality $L(H_1; \boldsymbol{I}) \geq L(H_0; \boldsymbol{I})$ holds.*

Proof. Let us denote $A(\mathbf{x}, H_i; \boldsymbol{I})$ as the expression within the outer minimum of Eq. (4.15)

$$\begin{aligned} A(\mathbf{x}, H_i; \boldsymbol{I}) = & \sum_{p \in V} F^p(\boldsymbol{I}, \min_{\boldsymbol{\alpha} \in H_i} \mathcal{H}\left(\phi^p(\boldsymbol{\alpha})\right)) \cdot x_p \\ & + \sum_{p \in V} B^p(\boldsymbol{I}, \min_{\boldsymbol{\alpha} \in H_i} \mathcal{H}\left(\phi^p(\boldsymbol{\alpha})\right)) \cdot (1 - x_p) + \sum_{(p,q) \in \mathcal{E}} P^{pq}(\boldsymbol{I}) \cdot \left| x_p - x_q \right| \end{aligned} \tag{B.1}$$

Then, $L(H_i; \boldsymbol{I})$ is reformulated as

$$L(H_i; \boldsymbol{I}) = \min_{\mathbf{x} \in \mathcal{L}^{|\mathcal{V}|}} A(\mathbf{x}, H_i; \boldsymbol{I}) \tag{B.2}$$

Assume that $H_1 \subset H_0$. Then, for any fixed $\mathbf{x}$, for all voxels $p \in \mathcal{V}$ and neighboring voxels $(p, q) \in \mathcal{E}$, the following inequalities hold.

$$\min_{\boldsymbol{\alpha} \in H_1} F^p\left(\boldsymbol{I}, \mathcal{H}\left(\phi^p(\boldsymbol{\alpha})\right)\right) \cdot x_p \geq \min_{\boldsymbol{\alpha} \in H_0} F^p\left(\boldsymbol{I}, \mathcal{H}\left(\phi^p(\boldsymbol{\alpha})\right)\right) \cdot x_p \tag{B.3}$$

$$\min_{\boldsymbol{\alpha} \in H_1} B^p\left(\boldsymbol{I}, \mathcal{H}\left(\phi^p(\boldsymbol{\alpha})\right)\right) \cdot (1 - x_p) \geq \min_{\boldsymbol{\alpha} \in H_0} B^p\left(\boldsymbol{I}, \mathcal{H}\left(\phi^p(\boldsymbol{\alpha})\right)\right) \cdot (1 - x_p) \tag{B.4}$$

This is because x_p and $(1 - x_p)$ are non-negative ($\because x_p \in \{0, 1\}$), as are F^p and B^p. By summing up inequalities (B.3) and (B.4) over all pixels $p \in \mathcal{V}$, and adding $\sum_{(p,q)\in\mathcal{E}} P^{pq}(\boldsymbol{I}) \cdot |x_p - x_q|$ to both sides that are constant with respect to $\alpha \in H_i$, we obtain

$$A(\mathbf{x}, H_1; \boldsymbol{I}) \geq A(\mathbf{x}, H_0; \boldsymbol{I}) \ \text{ for } \forall \mathbf{x} \in \mathcal{L}^{|\mathcal{V}|}, \tag{B.5}$$

i.e., the monotonicity holds for any fixed $\mathbf{x}$. Let $\mathbf{x}_1$ be the segmentation that yields the global optimum of $A(\mathbf{x}, H_1; \boldsymbol{I})$, i.e., $\mathbf{x}_1 = \arg\min_{\mathbf{x} \in \mathcal{L}^{|\mathcal{V}|}} A(\mathbf{x}, H_1; \boldsymbol{I})$. Let $\mathbf{x}_0$ be the segmentation that yields the global optimum of $A(\mathbf{x}, H_0; \boldsymbol{I})$, i.e., $\mathbf{x}_1 = \arg\min_{\mathbf{x} \in \mathcal{L}^{|\mathcal{V}|}} A(\mathbf{x}, H_0; \boldsymbol{I})$. Then, from the definition provided previously and monotonicity (B.5), we obtain

$$L(H_1; \boldsymbol{I}) = A(\mathbf{x}_1, H_1; \boldsymbol{I}) \overset{\because (B.5)}{\geq} A(\mathbf{x}_1, H_0; \boldsymbol{I}) \overset{\because \text{def}}{\geq} A(\mathbf{x}_1, H_0; \boldsymbol{I}) = L(H_0; \boldsymbol{I}) \tag{B.6}$$

□

B.2 Computability

For a branch-and-bound search algorithm, the lower bound must be computable in an efficient manner. To compute the lower bound in Eq. (4.17), two types of optimizations are required, i.e., maximization/minimization with respect to $\boldsymbol{\alpha} \in H_i$ and minimization in terms of $\mathbf{x} \in \mathcal{L}^{|\mathcal{V}|}$. The former is computable through the fundamental theorem of linear programming [66]. The function that needs to be minimized is a linear function, and H_i is a convex polygon; thus, the maximum and minimum values of the function are obtained only on the vertex of the polygon [66]. Computing each vertex of H_i is equivalent to the solution of a system of d equations with d variables, which has a computational complexity of $\mathcal{O}(d^3)$ [87]. Then, using a set of vertex vectors V_i, the maximum and minimum values of the function at each voxel can be computed from Eqs. (4.18) and (4.19) with $\mathcal{O}(d|V_i|)$. In contrast, the latter minimization equals the minimum of a submodular quadratic pseudo-Boolean

function. The theoretical complexity is the low-order polynomial of $|\mathcal{V}|$ time if it is solved using the s-t mincut [48].

B.3 Tightness

corollary When the set of shapes prior to $\boldsymbol{g}(H_i)$ is a singleton, the lower bound of a function coincides with its minimum value, i.e.,

$$L(H_i; \boldsymbol{I}) := \min_{\mathbf{x} \in \mathcal{L}^{|\mathcal{V}|}} A(\mathbf{x}, H_i; \boldsymbol{I}) = \min_{\mathbf{x} \in \mathcal{L}^{|\mathcal{V}|}} \min_{\boldsymbol{\alpha} \in H_i} E(\mathbf{x}, \boldsymbol{g}(\boldsymbol{\alpha}); \boldsymbol{I}) \tag{B.7}$$

corollary

Proof. Assuming that $\boldsymbol{g}(H_i)$ is a singleton and that $\boldsymbol{\alpha}^*$ is an arbitrary member of H_i,

$$\min_{\boldsymbol{\alpha} \in H_i} E(\mathbf{x}, \boldsymbol{g}(\boldsymbol{\alpha}); \boldsymbol{I}) = E(\mathbf{x}, \boldsymbol{g}(\boldsymbol{\alpha}^*); \boldsymbol{I}) \tag{B.8}$$

Taking the minimum value from both sides with respect to $\mathbf{x}$ yields the equation

$$\min_{\mathbf{x} \in \mathcal{L}^{|\mathcal{V}|}} \min_{\boldsymbol{\alpha} \in H_i} E(\mathbf{x}, \boldsymbol{g}(\boldsymbol{\alpha}); \boldsymbol{I}) = \min_{\mathbf{x} \in \mathcal{L}^{|\mathcal{V}|}} E(\mathbf{x}, \boldsymbol{g}(\boldsymbol{\alpha}^*); \boldsymbol{I}) \tag{B.9}$$

Under the same assumption, the expression within the outer minimum of Eq. (4.16) will be

$$\begin{aligned} A(\mathbf{x}, H_i; \boldsymbol{I}) = & \sum_{p \in \mathcal{V}} F^p(\boldsymbol{I}, \min_{\boldsymbol{\alpha} \in H_i} \mathcal{H}\big(\phi^p(\boldsymbol{\alpha})\big)) \cdot x_p \\ & + \sum_{p \in \mathcal{V}} B^p(\boldsymbol{I}, \min_{\boldsymbol{\alpha} \in H_i} \mathcal{H}\big(\phi^p(\boldsymbol{\alpha})\big)) \cdot (1 - x_p) + \sum_{(p,q) \in \mathcal{E}} P^{pq}(\boldsymbol{I}) \cdot \big|x_p - x_q\big| \\ & = E(\mathbf{x}, \boldsymbol{g}(\boldsymbol{\alpha}^*); \boldsymbol{I}) \end{aligned} \tag{B.10}$$

By replacing $E(\mathbf{x}, \boldsymbol{g}(\boldsymbol{\alpha}^*); \boldsymbol{I})$ in Eq. (B.9) with $A(\mathbf{x}, H_i; \boldsymbol{I})$, according to the relationship described by Eq. (B.10), we obtain

$$\min_{\mathbf{x} \in \mathcal{L}^{|\mathcal{V}|}} \min_{\boldsymbol{\alpha} \in H_i} E(\mathbf{x}, \boldsymbol{g}(\boldsymbol{\alpha}); \boldsymbol{I}) = \min_{\mathbf{x} \in \mathcal{L}^{|\mathcal{V}|}} A(\mathbf{x}, H_i; \boldsymbol{I}) \tag{B.11}$$

Therefore, when the set of shapes prior to $\boldsymbol{g}(H_i)$ is a singleton, Eq. (B.7) holds. □

Appendix C

Extensibility

C.1 Extensibility of SSM

I would like to prove that the lower bound of an SSM defined with a monotonically increasing function $f : \mathbb{R} \to \mathbb{R}$ and $t \in \mathbb{R}$ in Eq. (4.24) can be calculated efficiently by our framework. Note that $\phi^p(\boldsymbol{\alpha})$ is a linear function in terms of $\boldsymbol{\alpha} \in \mathcal{R}_{\boldsymbol{\alpha}}$. Because both $f(x)$ and $\mathcal{H}(x' - t)$ are monotonically increasing functions of $x, x' \in \mathbb{R}$, their composite $\mathcal{H}(f(x) - t)$ is also a monotonically increasing function of x. Thus, the maximum and minimum of $g_p(\boldsymbol{\alpha}) = \mathcal{H}(f(\phi^p(\boldsymbol{\alpha})) - t)$ (Eq. (4.24) in terms of $\phi^p(\boldsymbol{\alpha})$ over $\alpha \in H_i$ are found at $\boldsymbol{\alpha}^* = \arg\max_{\boldsymbol{\alpha} \in H_i} \phi^p(\boldsymbol{\alpha})$ and $\boldsymbol{\alpha}^* = \arg\min_{\boldsymbol{\alpha} \in H_i} \phi^p(\boldsymbol{\alpha})$, respectively. On the other hand, because $\phi^p(\boldsymbol{\alpha})$ is a linear function in terms of $\boldsymbol{\alpha} \in \mathcal{R}_{\boldsymbol{\alpha}}$, the maximum and minimum of $\phi^p(\boldsymbol{\alpha})$ for $\boldsymbol{\alpha} \in H_i$ are always found at the vertices $\boldsymbol{v} \in V_i$ of polygon H_i owing to the fundamental theorem of linear programming [66]. Consequently, the maximum and minimum of $g_p(\boldsymbol{\alpha})$ are also found at the vertices $\boldsymbol{v} \in V_i$, and are given as follows:

$$g_p^{\max}(H_i) = \begin{cases} 0 & \text{if } f(\phi^p(\boldsymbol{v})) < t \quad \forall \boldsymbol{v} \in V_i \\ 1 & \text{otherwise} \end{cases} \tag{C.1}$$

$$g_p^{\min}(H_i) = \begin{cases} 1 & \text{if } f(\phi^p(\boldsymbol{v})) \geq t \quad \forall \boldsymbol{v} \in V_i \\ 0 & \text{otherwise} \end{cases} \tag{C.2}$$

Eqs. (C.1) and (C.2) can be computed efficiently by our proposed framework (see "Computability" in Appendix B).

C.2 Extensibility of energy functional

Corollary C.2.1. *Given the energy terms in Eq. (4.25) with $h_p^F(\mathbf{y})$ of Eq. (4.27) and Eq. (4.26) with $h_p^B(\mathbf{y})$ of Eq. (4.28), Eq. (4.30) holds.*

Proof. Given $H_i \subseteq \mathcal{R}_{\boldsymbol{\alpha}}$, the following inequalities hold:

$$\left(g_p^{\min}(H_i) =\right) \min_{\alpha \in H_i} g_p(\boldsymbol{\alpha}) \leq g_p(\boldsymbol{\alpha}) \leq \max_{\alpha \in H_i} g_p(\boldsymbol{\alpha}) \left(= g_p^{\max}(H_i)\right) \quad \forall \boldsymbol{\alpha} \in H_i, \forall p \in \mathcal{V} \tag{C.3}$$

Because $h_p^F(\cdot)$ in Eq. (4.27) and $h_p^B(\cdot)$ in Eq. (4.28) are the monotonically decreasing and increasing functions, respectively, we can derive the following inequalities based on the above monotonic relation of Eq. (C.3):

$$h_p^F(\boldsymbol{g}(\boldsymbol{\alpha})) \leq h_p^F(\boldsymbol{g}^{\max}(H_i)) \quad \forall \boldsymbol{\alpha} \in H_i, \forall p \in \mathcal{V}, \tag{C.4}$$

$$h_p^B(\boldsymbol{g}(\boldsymbol{\alpha})) \leq h_p^B(\boldsymbol{g}^{\min}(H_i)) \quad \forall \boldsymbol{\alpha} \in H_i, \forall p \in \mathcal{V}. \tag{C.5}$$

Taking the minimum of $h_p^F(\boldsymbol{g}(\boldsymbol{\alpha}))$ in Eq. (C.4) and $h_p^B(\boldsymbol{g}(\boldsymbol{\alpha}))$ in Eq. (C.5) over $\boldsymbol{\alpha} \in H_i$, we obtain

$$\min_{\boldsymbol{\alpha} \in H_i} h_p^F(\boldsymbol{g}(\boldsymbol{\alpha})) \geq h_p^F(\boldsymbol{g}^{\max}(H_i)) \quad \forall p \in \mathcal{V}, \tag{C.6}$$

$$\min_{\boldsymbol{\alpha} \in H_i} h_p^B(\boldsymbol{g}(\boldsymbol{\alpha})) \geq h_p^B(\boldsymbol{g}^{\max}(H_i)) \quad \forall p \in \mathcal{V}. \tag{C.7}$$

From Eqs. (C.6) and (C.7) as well as the definition of the energy terms, we obtain

$$\begin{aligned} \min_{\boldsymbol{\alpha} \in H_i} F^p(\boldsymbol{I}, \boldsymbol{g}(\boldsymbol{\alpha})) &= \lambda_1 \cdot \Pr\left(x_p = 0 \mid I_p\right) + \lambda_2 \cdot \min_{\boldsymbol{\alpha} \in H_i} h_p^F(\boldsymbol{g}(\boldsymbol{\alpha})) \\ &\geq \lambda_1 \cdot \Pr\left(x_p = 0 \mid I_p\right) + \lambda_2 \cdot h_p^F(\boldsymbol{g}^{\max}(H_i)) = F^p(\boldsymbol{I}, \boldsymbol{g}^{\max}(H_i)) \end{aligned} \tag{C.8}$$

$$\begin{aligned} \min_{\boldsymbol{\alpha} \in H_i} B^p(\boldsymbol{I}, \boldsymbol{g}(\boldsymbol{\alpha})) &= \lambda_1 \cdot \Pr\left(x_p = 1 \mid I_p\right) + \lambda_2 \cdot \min_{\boldsymbol{\alpha} \in H_i} h_p^B(\boldsymbol{g}(\boldsymbol{\alpha})) \\ &\geq \lambda_1 \cdot \Pr\left(x_p = 1 \mid I_p\right) + \lambda_2 \cdot h_p^B(\boldsymbol{g}^{\min}(H_i)) = B^p(\boldsymbol{I}, \boldsymbol{g}^{\min}(H_i)) \end{aligned} \tag{C.9}$$

Note that λ_1 and λ_2 are positive constants. Multiplying Eqs. (C.8) and (C.9) by x_p and $(1 - x_p)$ ($p \in \mathcal{V}$), respectively, we obtain

$$\min_{\boldsymbol{\alpha} \in H_i} F^p(\boldsymbol{I}, \boldsymbol{g}(\boldsymbol{\alpha})) \cdot x_p \geq F^p(\boldsymbol{I}, \boldsymbol{g}^{\max}(H_i)) \cdot x_p \tag{C.10}$$

$$\min_{\boldsymbol{\alpha} \in H_i} B^p(\boldsymbol{I}, \boldsymbol{g}(\boldsymbol{\alpha})) \cdot (1 - x_p) \geq B^p(\boldsymbol{I}, \boldsymbol{g}^{\max}(H_i)) \cdot (1 - x_p) \tag{C.11}$$

because x_p and $(1 - x_p)$ are nonnegative. Finally, summing up the inequalities in Eqs. (C.10) and (C.10) over all pixels $p \in \mathcal{V}$ and adding $\sum_{(p,q) \in \mathcal{E}} P^{pq}(\boldsymbol{I}) \cdot \left| x_p - x_q \right|$ to both sides that are constant with respect to $\boldsymbol{\alpha} \in H_i$, we obtain

$$\begin{aligned} &\sum_{p \in \mathcal{V}} \min_{\boldsymbol{\alpha} \in H_i} F^p(\boldsymbol{I}, \boldsymbol{g}(\boldsymbol{\alpha}))\, x_p + \sum_{p \in \mathcal{V}} \min_{\boldsymbol{\alpha} \in H_i} B^p(\boldsymbol{I}, \boldsymbol{g}(\boldsymbol{\alpha}))\, (1 - x_p) + \sum_{(p,q) \in \mathcal{E}} P^{pq}(\boldsymbol{I}) \left| x_p - x_q \right| \\ \geq &\sum_{p \in \mathcal{V}} F^p(\boldsymbol{I}, \boldsymbol{g}^{\max}(H_i))\, x_p + \sum_{p \in \mathcal{V}} B^p\left(\boldsymbol{I}, \boldsymbol{g}^{\min}(H_i)\right) (1 - x_p) + \sum_{(p,q) \in \mathcal{E}} P^{pq}(\boldsymbol{I}) \left| x_p - x_q \right| \end{aligned} \tag{C.12}$$

which is the expression within the outer minimum of Eq. (4.30). Because Eq. (C.12) holds for any $\mathbf{x} \in \mathcal{L}^{|\mathcal{V}|}$, Eq. (4.30) is derived by taking the minimum of Eq. (C.12) along $\mathbf{x} \in \mathcal{L}^{|\mathcal{V}|}$. □

Appendix D

List of Publications

International Journal Papers

1) A. Saito, A. Shimizu, H. Watanabe, S. Yamamoto, S. Nawano, H. Kobatake, Statistical shape model of a liver for autopsy imaging, International Journal of Computer Assisted Radiology and Surgery, vol.9, no.2, pp. 269–281, 2013

2) A. Saito, S. Nawano, A. Shimizu, Joint optimization of segmentation and shape prior from level-set-based statistical shape model, and its application to the automated segmentation of abdominal organs, Medical Image Analysis, vol.28, pp. 46–65, 2016

Domestic Journal Papers

1) 平野　靖, 時安竣一, 徐　睿, 橘　理恵, 木戸尚治, 斉藤　篤, 清水昭伸, 「死後CT像のテクスチャ解析による死因推定」, Medical Imaging Technology, vol.33, no.4, pp.177–184, 2015

International Conference Papers

1) A. Shimizu, M. Nakada, A. Saito, H. Watanabe, H. Kobatake, S. Nawano, Improvement of a simultaneous statistical shape model for multiple abdominal organs using synthesized-based learning, Computer Assisted Radiology and Surgery, vol.7, suppl.1, S327–S328, Pisa, Italy, June 2012

2) A. Saito, A. Shimizu, M. Nakada, H. Watanabe, S. Yamamoto, H. Kobatake, A statistical shape model of a dead liver for autopsy imaging, International Forum on Medical Imaging in Asia, O8-2, Daejeon, Korea, November 2012

3) A. Saito, A. Shimizu, H. Watanabe, S. Yamamoto, S. Nawano, H. Kobatake, Automated liver segmentation from a CT volume of a cadaver using a statistical shape model, Computer Assisted Radiology and Surgery, Heidelberg, Germany, June 2013

4) A. Saito, M. Nakada, E. Oost, A. Shimizu, H. Watanabe, S. Nawano, A statistical shape model for multiple organs based on synthesized-based learning, Proc. of Workshop on Computational and Clinical Applications in Abdominal Imaging in conjunction with MICCAI 2013, vol. 8198, pp. 280–289, Nagoya, Japan, September 2013

5) R. Oshima, A. Saito, H. Watanabe, A. Shimizu and S. Nawano, Relaxed conditional hierarchical statistical shape model of multiple organs, International Workshop on BioImage Recognition, Matsuyama, Japan, December 2013

6) R. Oshima, Y. Yamashita, A. Saito, A. Shimizu, S. Nawano, Multi-organ segmentation with a relaxed conditional hierarchical statistical shape model, Technical Committee on Medical Imaging, Fukuoka, Japan, June 2014

7) A. Saito, Okata S, A. Shimizu, H. Watanabe, S. Yamamoto, S. Nawano, Automated lung segmentation for autopsy imaging using graph cuts with a statistical shape model, Computer Assisted Radiology and Surgery, Fukuoka, Japan, June 2014

8) R. Oshima, A. Saito, S. Nawano, A. Shimizu, Improvement of abdominal multi-organ segmentation using a relaxed conditional hierarchical statistical shape model, International Forum on Medical Imaging in Asia, Tainan, Taiwan, January 2015

Domestic Conference Papers

1) 斉藤　篤, 中田美沙希, 渡部秀文, 清水昭伸, 小畑秀文, 縄野　繁, 「生成型学習を用いた臓器の統計的形状モデルの構築」, 『医用画像研究会 (MI)』, 信学技報, MI2011-130, pp.179–184, 那覇市ぶんかテンブス館（沖縄）, 2011年1月

2) 中田 美沙希, 斉藤　篤, 渡部秀文, 清水昭伸, 小畑秀文, 縄野　繁, 「腹部の複数臓器に対する統計的同時形状モデル」, 『医用画像研究会 (MI)』, 信学技報, MI2011-130, pp.293–298, 那覇市ぶんかテンブス館（沖縄）, 2011年1月

3) 平野　靖, 花岡昇平, 北坂孝幸, 横田　太, 橘　理恵, 斉藤　篤, 森　健策, 「MICCAI 2013参加報告」, 『医用画像研究会 (MI)』, 信学技報, MI2013-90, pp.187–191, 那覇市ぶんかテンブス館（沖縄）, 2014年1月

4) 平野　靖, 時安竣一, 徐　睿, 橘　理恵, 木戸尚治, 斉藤　篤, 清水昭伸, 「死後CT像のテクスチャ解析による死因・死後経過時間推定」, 『第33回日本医用画像工学会大会』, OP3-5, 東京慈恵会医科大学（東京）, 2014年7月

5) 斉藤　篤, 縄野　繁, 清水昭伸, 「セグメンテーションと事前形状の同時最適化のための一手法の提案と膵臓セグメンテーションへの応用」, 『医用画像研究会 (MI)』, 信学技報, MI2014-35, pp.179–184, 統計数理研究所（東京）, 2014年9月

6) 萩原康平, 斉藤　篤, 縄野　繁, 清水昭伸, 「グラフカットエネルギーの自動設計法に関する検討」, 『医用画像研究会 (MI)』, 信学技報, vol.114, no.482, MI2014-67, pp.73–76, ホテルミヤヒラ（沖縄）, 2015年3月

7) 立花幸子, 斉藤　篤, 山本正二, 縄野　繁, 清水昭伸 「死亡時CT像からの肺野セグメンテーションに関する検討」, 『医用画像研究会 (MI)』, 信学技報, vol.114, no.482, MI2014-112, pp.289–294, ホテルミヤヒラ（沖縄）, 2015年3月

8) 伊藤達也, 斉藤　篤, 花岡昇平, 東山滋明, 河邉譲治, 塩見　進, 清水昭伸, 「骨シンチグラム上の異常集積検出処理に関する初期検討」, 『日本医用画像工学大会』, PP24, 金沢歌劇座（金沢）, 2015年7月

9) 砂田太郎, 斉藤　篤, 花岡昇平, 東山滋明, 河邉譲治, 塩見　進, 清水昭伸, 「マルチアトラス法による骨シンチグラム上の解剖構造自動認識」, 『日本医用画像工学大会』, OP8-7, 金沢歌劇座（金沢）, 2015年8月

10) 岸本将志, 斉藤　篤, 山本　正二, 清水昭伸, 「Convolutional Neural Networkを用いた死亡時 CT 像からの皮質骨抽出処理の改良」, 『日本医用画像工学大会』, PP40, 金沢歌劇座（金沢）, 2015年7月

11) 岸本将志, 斉藤　篤, 大坂美穂, 高桑徹也, 山田重人, 清水昭伸, 「ヒト胚子の眼球を対象とした時空間統計モデルに関する初期検討」, 『医用画像研究会 (MI)』, 信学技報, MI2015-56, pp.39–44, 電気通信大学（東京）, 2015年9月

Tutorial paper

1) 平野　靖, 木戸尚治, 斉藤　篤, 清水昭伸, 「オートプシー・イメージングの現在と未来（3） Ai の計算機支援」, Medical Imaging Technology, vol.32, no.5, pp.351–354, 2014

Patents

1) 清水昭伸, 斉藤　篤, 「画像処理装置、方法、及びプログラム」, 特願2014-169911, 2014年8月 ＜申請中＞

Awards

1) 第2回 計算解剖学若手ワークショップ コンテスト 最優秀賞, 2013年5月

2) International Forum on Medical Imaging in Asia (IFMIA), Best Poster Award, 2015